



Universidade de São Paulo
Instituto de Astronomia, Geofísica e Ciências Atmosféricas
Departamento de Astronomia

Luiz Felipe Santiago Rodrigues

Sobre o problema da falta de galáxias satélites

São Paulo

2011

Luiz Felipe Santiago Rodrigues

Sobre o problema da falta de galáxias satélites

Tese apresentada ao Departamento de Astronomia do Instituto de Astronomia, Geofísica e Ciências Atmosféricas da Universidade de São Paulo como parte dos requisitos para a obtenção do título de Doutor em Ciências.

Área de Concentração: Astronomia

Orientador: Prof. Dr. Reuven Opher

São Paulo

2011

In memoriam Antonio Alexandre S. Rodrigues

Acknowledgments

I thank my beloved Denise Lopes, whom I had the good fortune to meet in the middle of this enterprise. Without her endless support and love, nothing of this could have been accomplished;

I thank my brother Antonio Alexandre, for all those unforgettable chats by the piano, when he refreshed my faith in humanity with his restless curiosity and his everlasting ability to amaze himself with this fascinating – and strange – Universe.

I am deeply grateful to my parents, for supporting me in all possible ways and at all times, and for bearing with my impatience during the writing of this thesis;

I am grateful to Reuven Opher, my thesis advisor, for showing me the fun that can be extracted from Physics and how the joys this activity can keep one's spirit forever youthful and one's mind sharp;

I enthusiastically thank Carlton Baugh, for making possible one of the most interesting episodes of my scientific life;

I also have special thanks to Rafael de Souza and Emille Ishida, colleagues, collaborators and friends, with whom important part of this work was developed and who had the patience to have a look at this thesis;

I am very grateful to all my colleagues and professors at IAG, with whom I had the opportunity to learn so much during these years;

I thank the Institute for Computational Cosmology, for the warm hospitality during my visit;

Last but not least, I thank the rest of my family and friends. Special thanks to Bruno, Rodrigo and Ricardo, for listening me in many difficult occasions.

This work received financial support from the Brazilian agencies CNPq and CAPES (process numbers: 142394/2006 and 4314-10-7, respectively).

*“Tudo transcende tudo;
Intimamente longe de si mesmo
E infinitamente, o universo
A si mesmo, existindo, se ilude.”*

in *Fausto, Tragédia subjectiva*, Fernando Pessoa

Resumo

Nesta tese, investigamos a discrepância existente entre o número de galáxias satélites da Via Láctea que é previsto e aquele que é observado, questão conhecida como “problema da falta de satélites” (PFS). Este problema pode ser reformulado em termos de um desacordo entre a função de luminosidades das galáxias satélites (FLS) que é estimada a partir de dados observacionais e a FLS predita por modelos numéricos de formação de galáxias. Nos revisamos tanto propriedades observacionais da população de satélites quanto a teoria associada à modelagem da formação de galáxias e estruturas. Para abordar o PFS, estudamos diferentes soluções possíveis. Nós desenvolvemos uma modificação simples ao potencial do inflaton usual e mostramos que esta leva à uma redução no número de halos de matéria escura de pequena massa. Nós usamos, então, um modelo semi-analítico de formação de galáxias para confirmar que supressões similares do espectro de potências de pequena escala produzem uma FLS com a forma correta. Em uma outra direção, nós discutimos outros mecanismos astrofísicos capazes de reduzir o número de galáxias pequenas, especificamente: os ventos gerados por explosões de supernovas e o aquecimento do meio intergalático durante a reionização do Universo. Finalmente, nós estudamos como um campo magnético primordial pode influenciar a formação de galáxias de pequena massa. Para isso, nós inicialmente mostramos que a pressão devida a um campo magnético leva a uma alteração significativa na massa de filtragem, levando a uma importante supressão na acreção de gás por galáxias de baixa massa. Introduzindo estas modificações em um modelo numérico de formação de galáxias, mostramos que, para valores realistas de intensidade de campo, a pressão devido ao campo magnético leva a um bom acordo entre a FLS prevista e observada.

Abstract

In this thesis we investigate the discrepancy between the predicted and observed number of satellite galaxies in the Milky Way, known as “the missing satellites problem” (MSP). This problem can be translated into the disagreement between the satellite luminosity function (SLF), which is estimated from the observational (particularly the SDSS) data and the SLF predicted by numerical models of galaxy formation. We review both the observational properties of the satellite population and the essentials of galaxy and structure formation modelling. To tackle the MSP, we study different possible solutions. We develop a small modification to the usual chaotic inflaton potential and show that it leads to a reduction in the number of small mass haloes. We use a semi-analytic model of galaxy formation to confirm that suppressions of the small scale power spectrum can produce a SLF with the correct shape. In a different direction, we discuss other astrophysical mechanisms that can reduce the number of small mass galaxies, namely: the outflows generated by supernovae explosions and the heating of the intergalactic medium during the reionization of the Universe. Finally, we study how a primordial magnetic field can influence the formation of small mass galaxies. We first find that small primordial magnetic field significantly change the filtering mass, leading to an important suppression in the gas accretion by small mass haloes. (The filtering mass is the mass for which the baryon accretion is reduced to approximately $1/2$ its normal value.) Introducing this modifications in the galaxy formation model, we show that for realistic field strengths, the pressure due to the magnetic field can result in a good match between the observed SLF and the model predictions.

List of Figures

2.1	Luminosity \times half-light radius for Milky Way's satellite galaxies and globular clusters	32
2.2	Luminosity \times metallicity relation for Milky Way's satellite galaxies and globular clusters	32
2.3	Hints of a common mass scale from the “Mateo plot” of Milky Way's satellites ($M/L \times M_V$)	34
2.4	The common (inner) mass scale in Milky Way's dSph ($M_{300} \times$ Luminosity)	36
2.5	The V-band Luminosity Function of the Milky Way's satellite galaxies . .	37
3.1	Comparison between Einasto, cored-NFW and cored-Isothermal subhalo number density profiles.	45
3.2	A dark matter haloes merger tree.	47
4.1	Cumulative circular maximum velocity function of the Milky Way satellites and the simulated subhaloes	56
4.2	Cumulative inner mass function of the Milky Way satellites and the simulated subhaloes	58
5.1	Saw-tooth and sinusoidal potentials, with $b = 0.025$ and $\lambda = 0.55$	66
5.2	Slow-roll-compatible regions of the parameter space (λ, b)	67
5.3	Matter power spectrum obtained in the context of the modified inflation model	67
5.4	Ratio $r = n_{\text{saw-tooth}}(m)/n_{\text{chaotic}}(m)$	68
5.5	Ratio $r = n_{\text{sin}}(m)/n_{\text{chaotic}}(m)$	69

5.6	Effect of a 25% suppression of the power spectrum at wavenumbers greater than $k_{\text{break}} = 15 \text{ Mpc}^{-1}$ on the b_J luminosity function.	71
5.7	Effect of a suppression of the power spectrum on the V luminosity function of the satellites of MW-like galaxies.	72
5.8	Effect of a suppression of the power spectrum on the the Metallicity-Luminosity relation of the satellites of a MW-like galaxy.	73
6.1	SNe feedback effect on the b_J Luminosity Function	77
6.2	Effect of changing α on the HI Mass Function	78
6.3	Effect of changing α on the V Luminosity Function of the satellites of MW-like galaxies.	79
6.4	Effect of changing α on the Metallicity-Luminosity relation of the satellites of a MW-like galaxy.	80
6.5	Effect of reionization on the b_J Luminosity Function	83
6.6	Effect of reionization on the V luminosity function of the satellites of MW-like galaxies.	84
6.7	Effect of reionization on the Metallicity-Luminosity relation of the satellites of a MW-like galaxy.	85
6.8	The effect of reionization on the mass-luminosity relation of satellite galaxies.	86
7.1	Variation of the filtering mass with redshift in the presence of a homogeneous magnetic field	94
7.2	Effect of a <i>dipole-like</i> ($p = 3/2$) random magnetic field on the filtering mass.	96
7.3	Effect of a <i>dipole-like</i> ($p = 3/2$) random magnetic field on the filtering mass.	97
7.4	Effect of a <i>ring-like</i> ($p = 1$) random magnetic field on the filtering mass. .	97
7.5	Effect of a <i>ring-like</i> ($p = 1$) random magnetic field on the filtering mass. .	98
7.6	The b_J luminosity function for different values of homogeneous primordial magnetic field.	100

7.7	The stellar mass function for different values of homogeneous primordial magnetic field.	101
7.8	The HI mass function for different values of homogeneous primordial magnetic field.	102
7.9	The V luminosity function function of satellite galaxies for different values of homogeneous primordial magnetic field.	103
7.10	The luminosity-metallicity relation for satellite galaxies of a Milky-Way-like central galaxy, under different values of homogeneous primordial magnetic field.	103
7.11	Effects of magnetic fields on the inner mass of the satellite galaxies. . . .	104
A.1	The b_J luminosity function of the fiducial model.	134
A.2	The star formation history predicted by the fiducial model.	134
A.3	The HI mass function predicted by the fiducial model.	135
A.4	The relation between the mass of the mass of the bulge and the mass of the central black hole predicted by the fiducial model.	135
B.1	In the upper panel, the continuous (gray) curve shows the NFW density profile of a halo of mass $10^7 M_\odot$ at $z = 10$, and the (blue) points correspond to the general profile with $\alpha = 1$, $\gamma = 1/2$ and $b = 1.085 r_s = 36.8$ pc. In the lower panel the fractional difference between the two profiles is shown.	145
B.2	In the upper panel, the continuous (gray) curve shows the Burkert density profile of a halo of mass $10^7 M_\odot$ at $z = 10$, and the (blue) points correspond to the general profile with $\alpha = 3/5$, $\gamma = 6/5$ and $b = 1.58 r_s = 53.7$ pc. In the lower panel the fractional difference between the two profiles is shown.	146
B.3	New equilibrium configuration of the perturbed halo removing 5% (dashed curve), 10% (dotted curve) or 15% (thin curve) of the total mass of the halo, compared to the NFW profile (top solid line).	149

B.4	New equilibrium configuration of the perturbed halo removing 1% (dotted line) and 2.5% (dashed line) of total energy E , compared to the original Burkert profile (solid line).	150
-----	---	-----

List of Tables

- 2.1 Summary of properties of dSph satellites of the Milky Way. 30
- A.1 Properties of the two types of run employed. 132
- A.2 Fiducial parameters (continues) 136
- A.3 Fiducial parameters (continues) 137
- A.4 Fiducial parameters 138

Contents

1. <i>Introduction</i>	23
2. <i>Observational properties of the Milky Way satellite population</i>	27
2.1 The properties of the dwarf satellites population	31
2.2 The common mass scale	33
2.3 The Satellite Galaxies Luminosity function	35
2.4 Summary	38
3. <i>Modelling structure and galaxy formation</i>	39
3.1 N-body simulations	41
3.1.1 Large scale simulations	42
3.1.2 Probing the small scales	43
3.2 Semi-analytic models of galaxy formation	45
3.2.1 Constructing the merger tree	46
3.2.2 Hot gas accretion	48
3.2.3 Gas cooling and disk formation	49
3.2.4 Quiescent star formation in disks	50
3.2.5 Galaxy mergers and spheroid formation	51
3.2.6 AGN feedback	52
3.2.7 Other processes	52
3.3 Summary	52
4. <i>Formulating the satellites problem</i>	55

5. <i>Initial power spectrum distortions</i>	61
5.1 Features in the inflationary potential	62
5.1.1 The slow-roll formalism: a reminder	63
5.1.2 The mass function	65
5.1.3 Modified potentials	65
5.1.4 Results	67
5.2 Warm dark matter	69
5.3 Effects on galaxy properties	70
5.4 Summary and discussion	73
6. <i>SNe feedback and reionization</i>	75
6.1 Supernovae feedback	76
6.2 Reionization	79
6.3 Summary and discussion	87
7. <i>Magnetic fields and galaxy formation</i>	89
7.1 Primordial Magnetic Fields	90
7.2 Effects on the filtering mass	92
7.2.1 Homogeneous magnetic fields	92
7.2.2 Random magnetic fields	94
7.3 Impact of a primordial magnetic field on the formation of satellite galaxies	99
7.4 Summary and discussion	104
8. <i>Conclusions</i>	107
<i>Bibliography</i>	113
<i>Appendix</i>	129
A. <i>Fiducial model</i>	131
A.1 Halo gas accretion module	131
A.2 Parameters choice	132
A.3 Runs	132

A.4	Resources	133
B.	<i>Cusps and cores</i>	139
B.1	Introduction	139
B.2	Expulsion of baryonic gas by a supernova explosion	141
B.2.1	Evolution of a supernova blastwave	141
B.2.2	Gas mass fraction	142
B.3	Evolution of the density profile of dark haloes	142
B.3.1	Distribution functions and density profiles	143
B.3.2	Parametrizing the density profile	143
B.3.3	Perturbing the distribution function	147
B.3.4	Relation between relative energy and perturbed halo mass	147
B.4	Results	148
B.5	Conclusions and discussion	150

Chapter 1

Introduction

In the context of the standard cosmological model, it is believed that the Universe is composed mainly of dark matter and dark energy. The Universe was initially dense, hot and approximately homogeneous. Its small inhomogeneities were generated through the amplifications of quantum fluctuations during an accelerated expansion period called inflation – which is also responsible for the negligible curvature of the Universe.

Through gravitational instability, these inhomogeneities in the dark matter component were able to grow denser, generating gravitationally bound systems called haloes, which often merge. Big streams of small dark matter haloes, eventually merge and generate larger mass haloes.

Baryonic matter stayed tightly coupled to the photons until a low enough temperature allowed the formation of neutral atoms through recombination. This allowed the decoupling of the gas from the photon background. The gas, then, started to fall into the dark matter haloes, until its temperature was increased by an accretion shock and settled down into thermal and hydrostatic equilibrium.

The gas started then to radiatively cool, losing pressure support and formed a disk at the centre of each halo. Portions of the cold gas fragmented and collapsed, allowing the formation of stars. Some of these, exploded in supernovae, generating shock waves capable of expelling part of the gas back to the interstellar and intergalactic media. The same supernovae produced gradual enrichment of the media, making heavy elements more abundant with time.

Eventually, some of the disk galaxies merged, completely destroying their previ-

ous disk symmetry when the sizes of the galaxies were comparable. The turbulence induced by the merger strongly enhanced the star formation, which led to the consumption of most of the gas in the galaxy and ended in star formation burst. This resulted in a spheroidal population of stars.

The hierarchical galaxy formation scenario, superficially delineated in the previous paragraphs, has successfully allowed the solution of many long standing mysteries. Within this picture it was possible to understand both qualitatively and quantitatively the diversity of galaxy morphologies, colours and luminosities, as well as how these relate with their spatial distribution and environment.

Despite the many successes of such a paradigm, there are still unfilled gaps. Of particular importance is the apparent tension between theory and observation on small scales.

About a decade ago, cosmological numerical simulations reached a resolution high enough to allow one to follow the formation of structures of mass scales $\lesssim 10^7 M_\odot$. This led to the discovery that hundreds of bound dark matter substructures could survive tidal disruption until the present era in dark matter haloes of masses similar to the halo of the Milky Way. This strongly contrasted with the observed relatively small number of satellite galaxies, which was ~ 40 at that time.

This discrepancy, which became known in the literature as the “missing satellites problem” (MSP), apparently challenged the standard cold dark matter based scenario, since it suggested a possible minimal clustering scale for dark matter structures.

In the recent years the MSP has been alleviated both on observational and theoretical grounds: a population of ultra-faint, dark matter dominated, dwarf spheroidal galaxies was discovered – more than doubling the number of known satellites; concurrently, semi-analytic models of galaxy formation demonstrated that standard astrophysical processes, such as supernovae feedback or the photoheating during the reionization epoch, could selectively suppress star formation in the small mass haloes, answering the MSP without relying on extra assumptions regarding the dark matter particle properties or the initial conditions of the Universe.

However, despite the growing plausibility of standard baryonic processes as an explanation to the MSP, there are still significant uncertainties associated with the phys-

ical processes responsible for the suppression of the formation of small galaxies. Also, there is yet no convincing evidence of the existence of a big population of satellite dark subhaloes, which are a consequence of this scenario.

During my doctoral studies, I dedicated most of the time to the study of these small scale discrepancies. In this thesis I review the state of our knowledge regarding the MSP and present some original contributions.

The thesis is organized in the following way:

In chapter 2 the observational properties of the satellite population are reviewed and discussed.

In chapter 3 the essentials of galaxy and structure formation modelling are reviewed. Also described are the major physical processes involved in galaxy formation and how they are implemented in GALACTICUS.

In chapter 4 the MSP is described and the major classes of tentative solutions to it are listed.

Chapter 5 focuses on the possibility of solving the MSP by a change in the initial power spectrum of density perturbations. A simple oscillatory modification to the chaotic inflaton potential is introduced, and the consequences to the power spectrum and to the number of small mass haloes are discussed. The effect of warm dark matter models on the initial power spectrum is also briefly reviewed. Finally, the impact on the satellite galaxy population of a suppression of the power spectrum on small scales is analysed.

Chapter 6 examines the possibility of a solution of the MSP through the action of winds produced by supernovae, and the heating of the intergalactic medium by photoionizing radiation.

In chapter 7, the consequences on galaxy formation of a primordial magnetic field are studied. First, a motivation for a primordial magnetic field is briefly reviewed. Then, the impact of such a field on the filtering mass is discussed, both for the case of a homogeneous and a random primordial magnetic field. (The filtering mass is approximately the halo mass for which the baryon accretion is reduced to $1/2$ its normal value.) Finally, the net effect of such a field on the satellite galaxy population is evaluated.

Finally, in chapter 8, the results of this thesis are summarized and discussed. Perspectives and future directions of the research are described.

In appendix A, I list extra details of the semi-analytic model of galaxy formation that is employed to illustrate many parts of this work.

A very related topic that was also studied during the period of the doctorate is the possibility that the density profile of dark matter dominated galaxies deviates from the expected cuspy profile. While this problem is complementary to the MSP, it is less sound from the observational point of view, and for this reason was left out of the thesis. Nevertheless, in appendix B, I present some original analytical arguments, developed during this doctorate, that quantify the impact of SNe explosions on the form of the dark matter inner density profile.

Chapter 2

Observational properties of the Milky Way satellite population

*“ O Universo não é uma idéia minha.
A minha idéia do Universo é que é uma idéia minha.
A noite não anoitece pelos meus olhos,
A minha idéia da noite é que anoitece por meus olhos.
Fora de eu pensar e de haver quaisquer pensamentos
A noite anoitece concretamente
E o fulgor das estrelas existe como se tivesse peso. ”*

Alberto Caeiro

In order to correctly enunciate the missing satellites problem, it is necessary to understand the observational properties of these objects.

Most of the satellite galaxies of the Milky Way are classified as dwarf spheroidal galaxies (dSphs). This type of galaxy is characterized¹ by a spheroidal distribution of stars, total absence of gas or dust and low luminosity ($M_V \gtrsim -13$).

In the literature, the satellite dSphs of the Milky Way are usually (due to historical and convenience reasons) further divided into two subsets: the so-called *classical* satellites, composed of 9 objects discovered before 1994, and the *ultra-faint* dwarf galaxies, ~ 11 objects discovered since 2005.

Classical satellites The first dSphs to be discovered were Sculptor and Fornax, by Shapley (1938a,b). In the decade of 1950, four more satellites were discovered in the Palomar Observatory Sky Survey (POSS): Ursa Minor, Draco, Leo I and Leo II. In 1977,

¹ I postpone a more precise definition of dSph for the discussion, further in this chapter, on the differences between dSphs and globular star clusters.

in ESO/SRC Southern Sky Survey (the Southern hemisphere counterpart of the POSS), Carina was discovered.

Carina was the last satellite discovered by visual inspection. At the time of its discovery, it was noticed that the discovery of similar objects could only be possible using detailed star counts in regions of high foreground stellar density. This perception was confirmed with the discovery of Sextans in 1990, using an automated plate machine that scanned the same POSS and ESO/SRC data inspected decades before.

The last classical satellite discovered was Sagittarius

Ultrafaint galaxies From 1994 until 2004, there were no new discoveries of satellites of the Milky Way. Since 2005, however, 11 dSphs were discovered², using the data from the Sloan Digital Sky Survey (SDSS, York et al. 2000).

There are essentially three strategies which, when adopted, can lead to the discovery of new faint satellite galaxies (Willman, 2010):

1. obtain photometry of stars to fainter apparent magnitudes,
2. suppress, more efficiently, the noise from point sources contaminating the signal from stars belonging to a dwarf galaxy,
3. reduce spurious detections, the primary source of which had been galaxies misclassified as point sources.

The explosion of dSphs discoveries using SDSS data is explained by its multiband photometry and by the accuracy in its star-galaxy separation, thus facilitating (2) and (3). Another essential feature is the extent and uniformity of the SDSS database.

I briefly summarize the technique that is currently employed in the search of dwarf galaxies (Willman, 2010).

First a color-magnitude filter is applied to the data, selecting only stars which could be part of an old stellar population over a given distance interval (the whole process is later repeated varying the distance). This leads to the removal of a great part of the Milky Way stars which act as the primary source of noise in this analysis.

² This number can increase if one includes objects which are not yet consensually classified as dSph as the case of Segue 2, Bootes II and Leo V.

From the filtered sample of stars, a smoothed map is generated. Regions above a certain threshold in this map correspond to dwarf galaxy candidates. The threshold is a function of the number density of sources after the filtering of the sample. It is obtained simulating various realizations of the search and requiring a limited number of spurious detections.

The candidates are then studied spectroscopically in order to check whether the systems are gravitationally bound and to evaluate their dark matter contribution.

Magellanic Clouds Together with the Andromeda galaxy, the Large Magellanic Cloud (LMC) and the Small Magellanic Cloud (SMC) are the only galaxies that can be seen by humans without the aid of a telescope. Thus, they are the satellite galaxies of the Milky Way known for the longest times.

These galaxies have total masses $M_{\text{LMC}} \approx 2 \times 10^{10} M_{\odot}$ and $M_{\text{SMC}} \approx 2.5 \times 10^9 M_{\odot}$ and are classified as irregular galaxies (dIrr). They are very bright: $M_{V,\text{LMC}} = -18.5$ and $M_{V,\text{SMC}} = -17.1$, and have small mass-to-light ratios when compared to other satellites: $\Upsilon_{\text{LMC}}^V = 9.3$ and $\Upsilon_{\text{SMC}}^V = 4.03$ (Grebel, 2000).

The two clouds are remarkably near each other, separated from each other by 20 kpc. This leads to interaction between the two objects, which are connected to each other by a gaseous *Magellanic bridge*, which can be detected by HI observations.

There is also a very big stream of gas associated with the Magellanic Clouds, called the *Magellanic Stream*, that extends for $\sim 100^\circ$ in the sky – which is (probably) caused by the ram pressure stripping of the gas in the Magellanic Clouds by the Milky Way.

The existence of satellites with the size and brightness of the Magellanic Clouds orbiting a galaxy as the Milky Way appears to be something rather unlikely. From the spectroscopic data from the SDSS, Liu et al. (2011) find that the probability for a galaxy with a luminosity similar to the Milky Way's to have 2 satellites as bright as the LMC and SMC is less than 4% (while the probability of having 1 satellite is $\approx 10\%$). These results are consistent with the probability of subhaloes with mass similar to the LMC/SMC to be found in a halo as massive as the Milky Way, calculated for the Millennium II simulation by Boylan-Kolchin et al. (2010).

Galaxy	D [kpc]	L_V [L_\odot]	$M_{1/2}$ [M_\odot]	$\Upsilon_{1/2}^V$ [M_\odot/L_\odot]	μ [mag arcsec $^{-2}$]	M_\star M_\odot
Carina	105 ± 2	$4.3^{+1.1}_{-0.9} \times 10^5$	$9.56^{+0.95}_{-0.90} \times 10^6$	44^{+13}_{-10}	25.5 ± 0.4	—
Draco	76 ± 5	$2.2^{+0.7}_{-0.6} \times 10^5$	$2.11^{+0.31}_{-0.31} \times 10^7$	200^{+80}_{-60}	25.3 ± 0.5	—
Fornax	147 ± 3	$1.7^{+0.5}_{-0.4} \times 10^7$	$7.39^{+0.41}_{-0.36} \times 10^7$	$8.7^{+2.8}_{-2.3}$	23.4 ± 0.3	—
Leo I	254 ± 18	$5.0^{+1.8}_{-1.3} \times 10^6$	$2.21^{+0.24}_{-0.24} \times 10^7$	$8.8^{+3.4}_{-2.4}$	22.4 ± 0.3	—
Leo II	233 ± 15	$7.8^{+2.5}_{-1.9} \times 10^5$	$7.25^{+1.19}_{-1.01} \times 10^6$	19^{+7}_{-5}	24.0 ± 0.3	—
Sculptor	86 ± 5	$2.5^{+0.9}_{-0.7} \times 10^6$	$2.25^{+0.16}_{-0.15} \times 10^7$	18^{+6}_{-5}	23.7 ± 0.4	—
Sextans	96 ± 3	$5.9^{+2.0}_{-1.4} \times 10^5$	$3.49^{+0.56}_{-0.48} \times 10^7$	120^{+40}_{-35}	26.2 ± 0.5	—
Ursa Minor	77 ± 4	$3.9^{+1.7}_{-1.3} \times 10^5$	$5.56^{+0.79}_{-0.72} \times 10^7$	290^{+140}_{-90}	25.5 ± 0.5	—
Boötes I	66 ± 3	$2.8^{+0.6}_{-0.4} \times 10^4$	$2.36^{+2.01}_{-1.02} \times 10^7$	1700^{+1400}_{-700}	27.7 ± 0.3	$6.7 \pm 0.6 \times 10^4$
Canes Venatici I	218 ± 10	$2.3^{+0.4}_{-0.3} \times 10^5$	$2.77^{+0.86}_{-0.62} \times 10^7$	240^{+75}_{-65}	27.1 ± 0.2	$5.8 \pm 0.4 \times 10^5$
Canes Venatici II	160 ± 5	$7.9^{+4.4}_{-3.0} \times 10^3$	$1.43^{+1.01}_{-0.59} \times 10^6$	360^{+380}_{-180}	$26.1^{+0.7}_{-0.6}$	$5.8 \pm 0.5 \times 10^5$
Coma Berenices	44 ± 4	$3.7^{+2.2}_{-1.4} \times 10^3$	$1.97^{+0.88}_{-0.60} \times 10^6$	1100^{+800}_{-500}	$27.3^{+0.7}_{-0.6}$	$9.2 \pm 1.7 \times 10^3$
Hercules	133 ± 6	$1.1^{+0.5}_{-0.3} \times 10^4$	$7.50^{+5.72}_{-3.14} \times 10^6$	1400^{+1200}_{-700}	$27.2^{+0.6}_{-0.5}$	$7.2^{+1.2}_{-1.1} \times 10^4$
Leo IV	160 ± 15	$8.7^{+5.4}_{-3.6} \times 10^3$	$1.14^{+3.50}_{-0.92} \times 10^6$	260^{+1000}_{-200}	$27.5^{+1.3}_{-1.2}$	$1.6^{+0.6}_{-0.4} \times 10^4$
Leo T	407 ± 38	1.4×10^5	$7.37^{+4.84}_{-2.96} \times 10^6$	110^{+70}_{-40}	—	—
Segue 1	23 ± 2	$3.4^{+3.0}_{-1.6} \times 10^2$	$6.01^{+5.07}_{-2.80} \times 10^5$	3500^{+5000}_{-2000}	$27.6^{+1.0}_{-0.7}$	$1.3 \pm 0.2 \times 10^3$
Ursa Major I	97 ± 4	$1.4^{+0.4}_{-0.4} \times 10^4$	$1.26^{+0.76}_{-0.43} \times 10^7$	1800^{+1300}_{-700}	$27.7^{+0.5}_{-0.4}$	$3.7^{+0.6}_{-0.5} \times 10^4$
Ursa Major II	32 ± 4	$4.0^{+2.5}_{-1.4} \times 10^3$	$7.91^{+5.59}_{-3.14} \times 10^6$	4000^{+3700}_{-2100}	27.9 ± 0.6	$1.2 \pm 0.1 \times 10^4$
Willman 1	38 ± 7	$1.0^{+0.9}_{-0.5} \times 10^3$	$3.86^{+2.49}_{-1.60} \times 10^5$	770^{+930}_{-440}	25.0 ± 0.2	$6.2 \pm 0.1 \times 10^5$

Table 2.1 - Summary of properties of dSph satellites of the Milky Way. Distances, V band luminosities half-light masses, and half-light mass to light ratios (D , L_V , $M_{1/2}$ and $\Upsilon_{1/2}^V$, respectively) obtained from (Wolf et al., 2010). The surface brightnesses, μ , were obtained from (Martin et al., 2008) and (Mateo, 1998), for the ultrafaint and classical dSph, respectively. The stellar masses were obtained from (Martin et al., 2008), under the assumption of a Salpeter IMF (assuming a Kroupa IMF lead to $\approx 50\%$ reduction in the stellar mass).

2.1 The properties of the dwarf satellites population

In table 2.1 (page 30) some properties of the dSph galaxies population are listed. It is noticed that most luminosities of the ultrafaint dSphs are two orders of magnitude smaller than a typical classical dSph, with median value $L_V \sim 10^4 L_\odot$. The typical surface brightness is $\mu \sim 27 \text{ mag arcsec}^{-2}$.

The extremely low values for luminosities and estimates of the stellar mass of these galaxies raises the issue of how to separate them from regular star clusters, since the latter may have the same brightness and stellar mass.

An ultrafaint dSph can be differentiated from globular cluster by the way the dynamics of the system is dominated by dark matter. Thus, in table 2.1, one finds rather extreme values for the mass to light ratio, frequently with $\Upsilon \sim 10^4 \frac{M_\odot}{L_\odot}$.

This distinction between globular clusters and dSph galaxies can be further appreciated in figure 2.1, where a bi-modality in the distribution of half-light radii can be seen. The similar velocity dispersions for star clusters and dwarf galaxies, together with an order of 10 difference in r_h , imply a difference of ~ 2 orders of magnitude in their phase densities ($\sim 10^4 M_\odot \text{ kpc}^{-3} \text{ km s}^{-3}$, for a dwarf galaxy).

While the dynamics indicates that globular clusters and satellite form distinct populations with different histories of formation, it is possible to further test this hypothesis observing the metal content of the two classes of objects.

In figure 2.2, is shown the data for the relation between luminosity and stellar metallicity compiled by Norris et al. (2010). A strong correlation can be seen between the total luminosity and the stellar metallicity of the dwarf spheroidal galaxies of the Galaxy. Globular clusters, on the other hand, present no clear correlation and typically a higher metallicity.

If one takes into account other dwarfs of the Local Group, this luminosity-metallicity relation found for Milky Way's dSphs can be extended up to $M_V \sim -15$ and remains approximately linear (Simon & Geha, 2007).

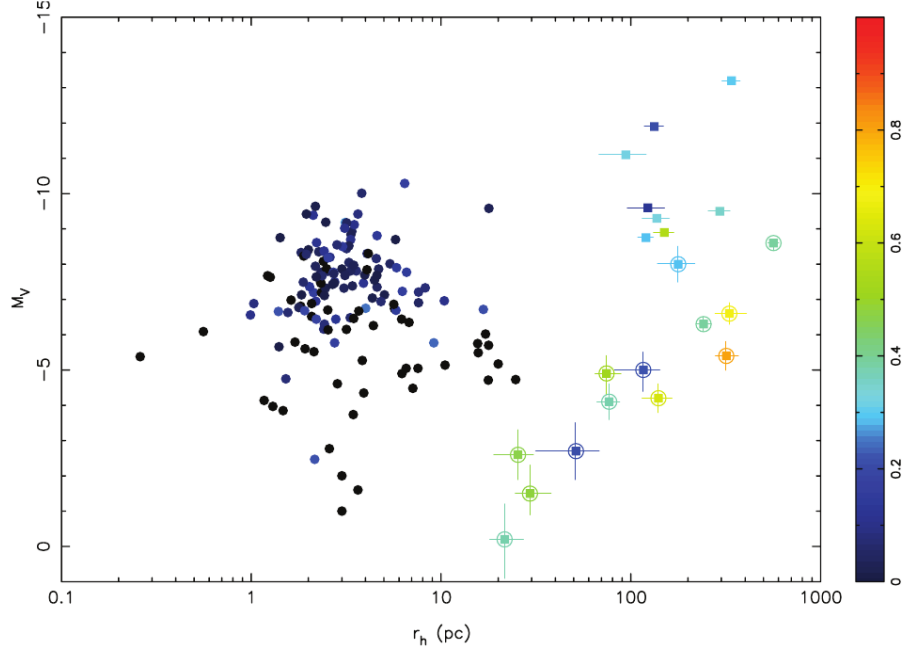


Figure 2.1: Luminosity \times half-light radius for Milky Way’s satellite galaxies and globular clusters. Reproduction of figure 6 of Martin et al. (2008). Colors code the ellipticity of the object and black corresponds to objects without an ellipticity measurement. Globular clusters are represented by circles; classical and ultrafaint satellites are represented by squares and circled squares, respectively.

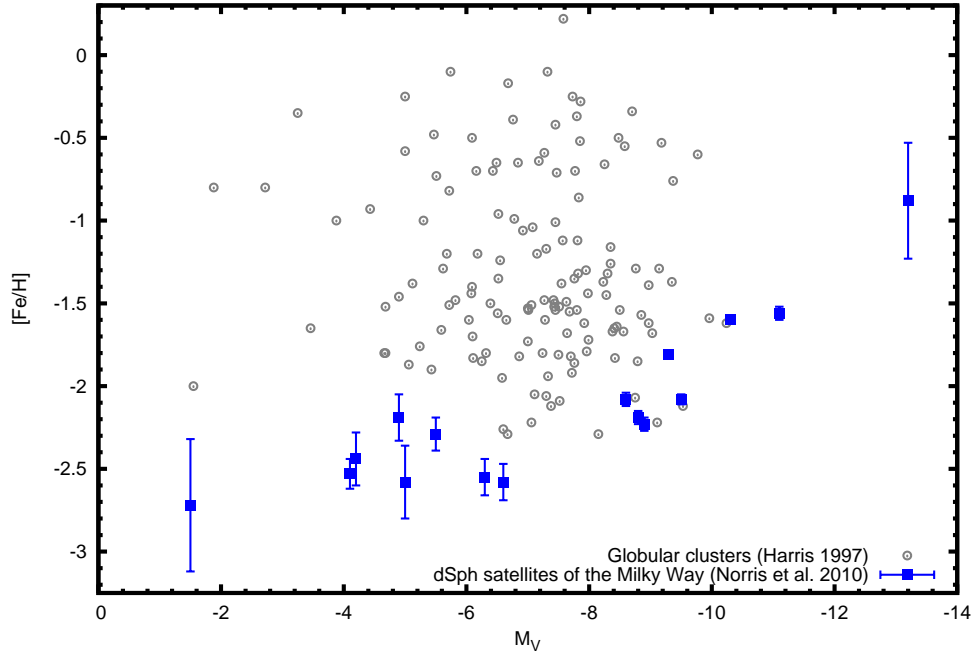


Figure 2.2: The relation between luminosity and stellar metallicity for objects near the Milky Way. The blue squares are the data for the satellite galaxies, compiled by Norris et al. (2010), with error bars indicating the dispersion. The grey circles show the globular cluster data from the VizieR Catalog VII/202 (Harris, 1996).

2.2 The common mass scale

Long before the discovery of the ultrafaint satellite galaxy population, Mateo et al. (1993) noticed that the satellite galaxies of the Milky Way (including the SMC and LMC) seemed to be consistent with the scenario that the galaxies are embedded in dark matter halos with a constant minimum mass (Mateo, 1998).

This conclusion was reached when studying a plot of the mass-to-light-ratio versus luminosity. In his paper, Mateo notices that the satellite population seems to obey the following expression:

$$\left(\frac{M}{L}\right)_{\text{total}} = \left(\frac{M_{\text{DM}}}{L} + \varepsilon\right), \quad (2.1)$$

where L is the luminosity of the galaxy, $M_{\text{DM}} \sim 10^7 M_{\odot}$ a common dark matter halo mass and $\varepsilon = \frac{M_{\star}}{L} = 2.5 M_{\odot}/L_{\odot}$ is the mass-to-light ratio of the stellar component, assumed to be constant.

The idea of a common mass scale motivated the proposition of the many alternative dark matter models that could generate it. One example is the idea of a Bose-Einstein condensate (BEC) dark matter, where dark matter haloes can be identified with Bose-Einstein condensates of extremely light bosons. In that case, the minimum mass scale is determined by the uncertainty principle (Lee, 2009; Lee & Lim, 2010).

In figure 2.3, an updated version of the $\Upsilon = M/L$ vs L plot is shown, using the data from table 2.1. Without taking into account the recently discovered ultrafaint satellites, one finds, as in Mateo et al. (1993), that the classical galaxies are consistent with being embedded in dark matter haloes of masses $10^7 - 10^8 M_{\odot}$.

This result does not seem to hold for the ultrafaint dwarfs (as first noticed by Simon & Geha 2007) which require smaller masses for small luminosities. However, before asserting that the hypothesis of a common or minimum mass for the dark matter haloes is false, one should bear in mind some limitations of this analysis.

The masses used to calculate Υ in figure 2.3 correspond to the masses at the half-light radius. This choice can lead to an underestimate of the mass content of haloes of galaxies with more compact stellar distributions. Besides, the assumption of a constant Υ for the stellar component may be dismissing the differences in the stellar populations that occupy haloes of different masses.

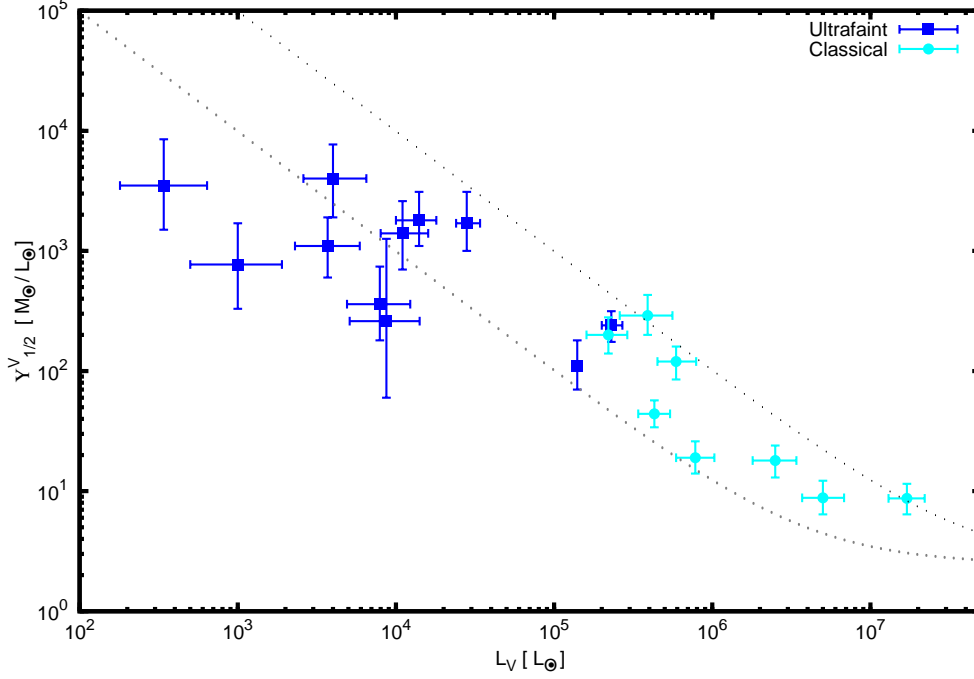


Figure 2.3: The “Mateo plot” of $\Upsilon = M/L$ versus L , updated with the data from Martin et al. (2008). The upper and lower dotted grey curves correspond to equation 2.1 with $M_{DM} = 10^8 M_\odot$ and $M_{DM} = 10^7 M_\odot$, respectively.

An alternative method that allows a more robust comparison between the dark matter content of different satellite galaxies is estimating the mass of each galaxy within a fixed radius. This radius must be chosen small enough in order avoid (or at least reduce) the extrapolation of the mass profile estimate beyond the observed limit of the stellar component.

It is worth reviewing how these mass estimates are made – and what are the assumptions involved. First, it is assumed that these systems are in steady state, which allows one to use the Jeans equation to relate the three dimensional radial density profile of the system, σ_r , and the stellar density profile, $\rho_\star(r)$, with the mass profile, $M(r)$,

$$r \frac{d(\rho_\star \sigma_r^2)}{dr} = -\rho_\star(r) \frac{G M(r)}{r} - 2\beta(r) \rho_\star \sigma_r^2, \quad (2.2)$$

where $\beta(r) = 1 - \sigma_\theta^2/\sigma_r^2(r)$ is the stellar anisotropy, which is either assumed to be null or marginalized out in the computation.

To estimate the mass within a certain radius, first one finds ρ_\star , fitting the measured

surface stellar density profiles, $I_*(R)$, to King or Plummer sphere profiles, which have a known de-projected three dimensional density profile — i.e. this allows converting $I_*(R) \rightarrow \rho_*(r)$.

Knowing the three dimensional stellar density and measuring the radial velocity dispersion, σ_r , one can solve equation 2.2 at a chosen radius.

After precise measurements of stellar velocity dispersions, Strigari et al. (2008) reported the discovery of a *common inner mass* for dSphs of the Milky Way. Specifically, they found that all dwarf satellites of the Milky Way, which span more than 4 orders of magnitude in luminosity, have a similar mass inside a 300 pc radius, $M_{300} \sim 10^7 M_\odot$.

This observation imposes limits on warm dark matter models, where the free streaming length sets a minimum mass. In fact, since N-body simulations indicate that the inner mass relates the total mass of the halo through

$$M_{300} \approx 10^7 M_\odot (M_{\text{total}}/10^9 M_\odot)^{0.35}, \quad (2.3)$$

it is possible to rule out candidate dark matter particles with masses $\lesssim 1\text{keV}$, which would result in minimum halo masses of order $\sim 10^9 M_\odot$.

2.3 The Satellite Galaxies Luminosity function

In order to estimate the luminosity function of the Milky Way satellite galaxies from the SDSS data, it is necessary to take into account the incompleteness of this experiment and the intrinsic inefficiency of the algorithm used to identify the galaxies (as overdensities in the stellar counts).

To estimate the detection efficiencies, Koposov et al. (2008) produced artificial catalogues by adding mock satellite galaxies and globular clusters to the original SDSS data. The same algorithm employed to detect the satellites in the original catalogue was, then, applied to the simulated ones. Doing this for many Monte Carlo realizations of mock dwarf galaxies with properties similar to the known ones, it was possible to access the probability of their discovery.

The detection efficiency corresponds to a steep function in surface brightnesses

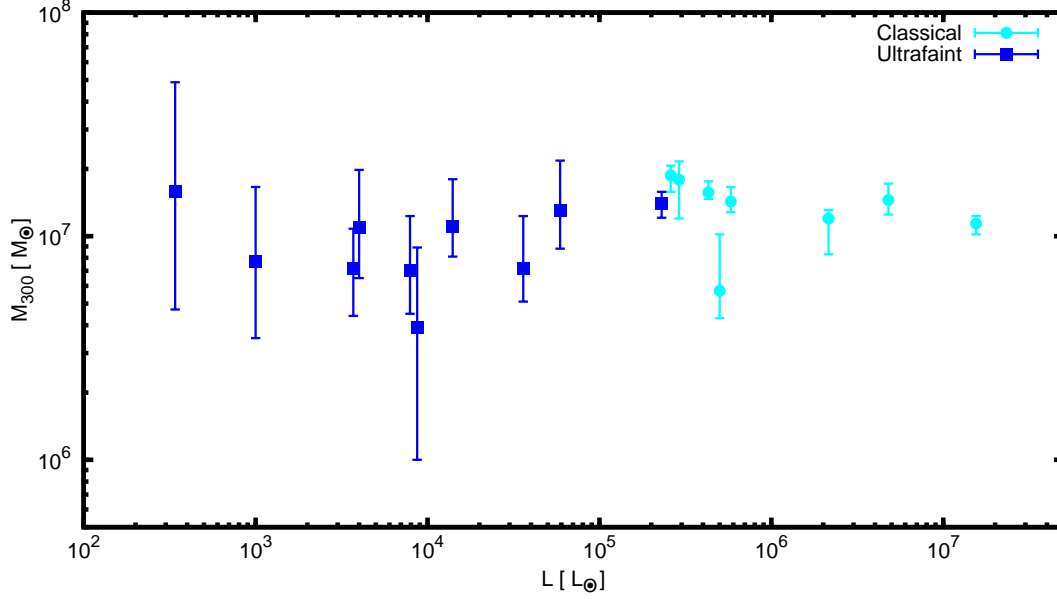


Figure 2.4: The common (inner) mass scale in Milky Way's dSph. The mass contained inside the inner 300 pc, M_{300} , was obtained from Strigari et al. (2008); the luminosities in the V band were obtained from Martin et al. (2008).

and magnitudes, well described by

$$\epsilon(M_V, \mu) = \frac{1}{4} \operatorname{erfc}\left(\frac{M_V - M_{V,\text{lim}}}{\sqrt{2} \sigma_{M_V}}\right) \operatorname{erfc}\left(\frac{\mu - \mu_{\text{lim}}}{\sqrt{2} \sigma_{\mu}}\right). \quad (2.4)$$

To account for the incompleteness of the sample, a correction factor, $c(M_V)$, was calculated by Koposov et al. (2008), considering the maximum radius that can be probed for each absolute magnitude, $r_{\text{max}}(M_V)$,

$$c(M_V) = \begin{cases} \frac{\int_0^{r_{\text{max}}(M_V)} n(r) r^2 dr}{\int_0^{r_{\text{LF}}} n(r) r^2 dr} & , \text{ if } r_{\text{max}}(M_V) < r_{\text{LF}} \\ 1 & , \text{ if } r_{\text{max}}(M_V) \geq r_{\text{LF}} \end{cases}, \quad (2.5)$$

where $n(r)$ is the distribution of satellite galaxies, and $r_{\text{LF}} = 280$ kpc is the radius within which the luminosity function will be calculated, which corresponds to the *virial radius* of the Milky Way galaxy.

The maximum radius, r_{max} , estimated by Koposov et al. (2008) for the SDSS DR5 is

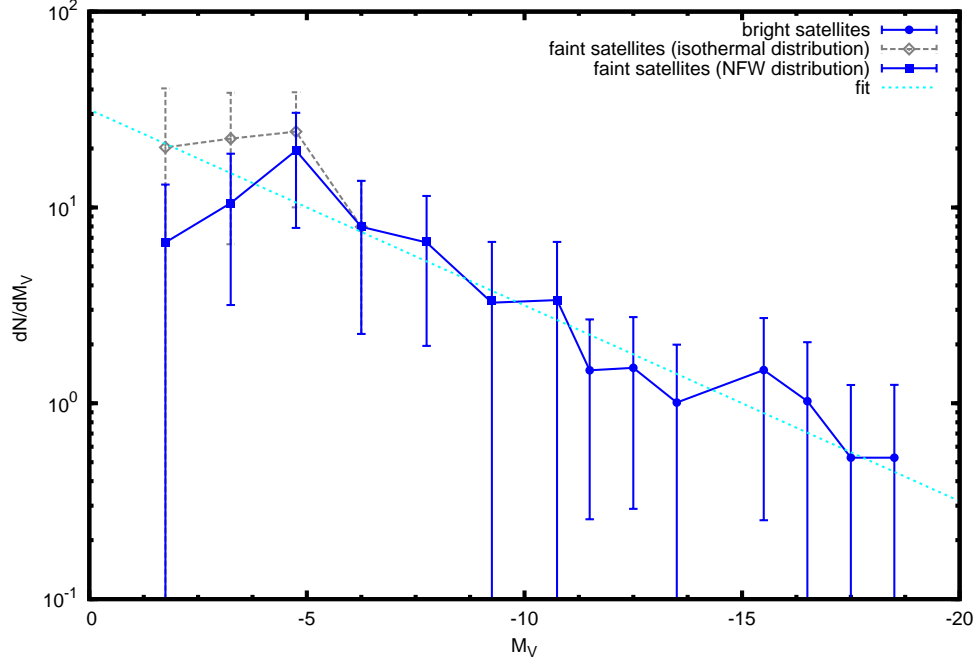


Figure 2.5: The V-band luminosity function of the satellites of the Milky Way. The squares and diamonds correspond to the data from Koposov et al. (2008); the filled circles to the data from Metz et al. (2007). The light blue dotted curve corresponds to the fit in equation 2.7. The error bars correspond to Poisson errors.

well approximated by (Tollerud et al., 2008)

$$r_{\max}(M_V) = \left(\frac{3}{4\pi f_{\text{DR5}}} \right)^{\frac{1}{3}} 10^{(-aM_V - b)/3} \text{Mpc}, \quad (2.6)$$

where $f_{\text{DR5}} = 0.194$ is the fraction of the sky covered by the survey.

Using equations 2.4 and 2.5, a corrected histogram of the luminosity distribution can be built by dividing each count by the detection efficiency associated with it, and dividing each bin by the incompleteness correction factor associated with it.

The satellite luminosity function obtained this way is shown in figure 2.5. The two curves plotted correspond to different choices for the satellite distribution in equation 2.5. Namely, a cored NFW-like distribution, $n(r) \propto (r + r_c)^{-1}(r + r_s)^{-2}$, is assumed in the case of the continuous blue curve, and a cored “isothermal sphere” distribution, $n(r) \propto (r + r_c)^{-2}$, is assumed in the case of the grey dashed curve.

Koposov et al. (2008) also points out that the luminosity function obtained can be

well described, in the range $-19 < M_V < -2$, by a simple power law

$$\frac{dN}{dM_V} = 10^{(0.1M_V + 1.5)}. \quad (2.7)$$

It is important to notice that the assumed satellite spatial distribution has significant influence on the shape of the luminosity function at magnitudes $M_V > -5$. Tollerud et al. (2008) find an even more appreciable enhancement in the faint end of the luminosity function after calculating the correction factor using a spatial distribution of subhaloes directly extracted from the *Via Lactea* simulation (Diemand et al., 2007).

2.4 Summary

In this chapter some important observational aspects of the satellite galaxy population were reviewed.

Despite sometimes having luminosities as low as the ones found in globular stellar clusters, faint satellites are strongly dominated by dark matter, with mass-to-light ratios that reach $\sim 10^4 M_\odot/L_\odot$.

There is, also, a strong correlation between the luminosity and the stellar metallicity of satellite galaxies, which is not observed in globular clusters – reinforcing the idea that these objects are of different nature.

Taking into account the efficiency and completeness of the observations, it was possible to estimate the luminosity function of the satellite population, which can be approximated by the power law: $dN/dM_V = 10^{(0.1M_V + 1.5)}$.

Another important observational property is that all satellites have approximately the same mass in their 300 pc radius: $M_{300} \sim 10^7 M_\odot$.

Chapter 3

Modelling structure and galaxy formation

*“If you wish to make an apple pie from scratch,
you must first invent the Universe.”*

Carl Sagan

The ultimate and highly ambitious goal of the field of extragalactic astrophysics is to obtain a consistent explanation for the rich phenomenology of galaxy properties, starting from a simple cosmological model and basic knowledge of star formation and evolution.

At very large scales, the gravitational field equations can be solved analytically through linear perturbations of the Friedmann-Lemaître-Robertson-Walker metric.

This type of approach is limited to studies of the distribution of very massive clusters of galaxies, which are approximately still in the linear regime. It is already a valuable tool to probe, for example, the properties of dark energy.

The most popular technique that allows us to go beyond this linear regime is called *N-body simulation*. In this kind of study, the evolution of a set of particles interacting gravitationally in an expanding universe is followed. The initial positions and velocities of the particles are chosen following a Gaussian density distribution filled with a given primordial power spectrum consistent with the CMB.

Since the particles interact only gravitationally, they can be naturally associated with dark matter. This technique, and the important results it led to, will be further discussed in sections 3.1.1 and 3.1.2.

Of course it is only possible to make comparisons between the predictions of N-body simulations and actual observations if one understands correctly the relationship between mass and light. It is a sensible assumption that light should trace mass,

since more gas would collapse into dark matter haloes with the deepest potential wells. This approach works well on very large scales, allowing the association of high mass dark matter haloes with clusters of galaxies.

However, one would like to go further and obtain definite predictions not only for the dark matter distribution but also for the baryonic content, accounting for gas thermodynamics and star formation. The most direct way to proceed in this direction is by adding, to the simulation, extra components to track the gas and the stars, the former being treated as a proper collisional fluid, obeying the equations of hydrodynamics.

There are two main techniques employed in this kind of simulation: smooth particle hydrodynamics (SPH, for a review see Rosswog 2009), based on a Lagrangian frame of reference, and adaptive mesh refinement (AMR, e.g. Fryxell et al. 2000), where the Eulerian hydrodynamics equations are solved with the aid of a fixed Cartesian mesh.

Recently a third technique was proposed by Springel (2010), where the Euler equations are solved on a moving unstructured mesh whose motion can be tied to motion of the fluid itself (what gives the method hybrid character, combining the properties of SPH and AMR techniques).

It is beyond the scope of this work to discuss such techniques in detail. Nevertheless, there is one important aspect of these simulations that cannot be overemphasised. An important part of the physics involved in galaxy formation occurs on scales well below the typical resolution of the simulation, receiving the name of *sub-grid* physics.

This subgrid physics is approached using sets of approximate differential equations motivated by observations or theoretical considerations. Belonging to this class, for example, are the calculations of the star formation rates.

Alternatively, instead of following the details of the gas distribution, one can try to model all the baryonic processes through sets of approximate, but well motivated, analytic differential equations. This technique, known as *semi-analytic galaxy formation modelling* or *phenomenological galaxy formation modelling* will be discussed in detail in section 3.2.

Semi-analytic models of galaxy formation (SAMs) have the major advantage of being computationally inexpensive when compared to direct simulations, which al-

lows for quick parameter-space explorations. Another important feature is the typical modular structure of the code, where each physical process is usually coded separately and can have its importance accessed by simply being switched on and off and comparing the results.

3.1 *N-body simulations*

In *N*-body simulations, collisionless dark matter is modelled by a large number of particles that interact gravitationally through a Newtonian potential written in comoving (“expanding”) coordinates (Bertschinger, 1998). The particles, thus, obey

$$\frac{d\mathbf{x}}{dt} = \frac{1}{a}\mathbf{v}, \quad \frac{d\mathbf{v}}{dt} + H\mathbf{v} = \mathbf{g}, \quad \nabla \cdot \mathbf{g} = -4\pi a [\rho(\mathbf{x}, t) - \bar{\rho}(t)] \quad (3.1)$$

where $a(t)$ is the expansion factor, H is the Hubble parameter, \mathbf{v} is the peculiar velocity, $\nabla = \frac{\partial}{\partial \mathbf{x}}$ is the gradient in comoving coordinates, ρ is the density and $\bar{\rho}$ is the mean density.

The most computationally costly step is the calculation of the gravitational force (the third term of equation 3.1), which ideally would require summation over all possible particle pairs in the simulation, thus a $O(N^2)$ problem.

In practice, some numerical technique is employed to reduce the number of operations. Typically, a combination of a hierarchical tree algorithm and a particle-mesh algorithm is used.

In a tree algorithm (Barnes & Hut, 1986) the space around a given particle is divided into an hierarchical structure of cells of variable size, containing one or more particles. If a cell of size l at distance D satisfies $l/D < \theta$ (where θ is a fixed tolerance parameter), the force due to this cell is computed treating all the particles inside it as a single particle at the cell’s centre of mass. In the case $l/D > \theta$, the cell is further subdivided.

This kind of procedure allows a precise calculation of the forces of N particles using $O(N \log(N))$ operations. It requires however a large amount of memory.

In the particle mesh (PM) method (Efsthathiou et al., 1985) the mass density field is first computed on a grid. This density field on the grid is Fourier-transformed using

a fast Fourier transform (FFT) technique, allowing the Poisson equation to be easily solved. The resulting gravitational force field is, then, interpolated back from the grid to the particles.

The PM algorithm requires $O(N) + O(N_g \log(N_g))$ operations, where N_g is the number of grid cells. While this procedure allows good mass resolution in most cases, the spatial resolution is limited to the mesh spacing that is chosen, leading to inaccuracies in the high density regions.

In a TreePM algorithm (Xu, 1995), particles in low density regions have the field computed through a PM method, while for particles in regions above a density threshold the gravitational force is calculated using the method for the internal particles and using the PM for the external. This hybrid approach allows spatial resolutions ~ 20 times higher than a pure PM code and is much faster and less resource intensive than a pure tree code.

3.1.1 Large scale simulations

An example of a very influential N-body simulation is the *Millenium simulation* (Springel et al., 2005). This was the largest N-body simulation ever performed, with a number of particles $N = 2160^3 \sim 10^{10}$, using the TreePM algorithm described above. The simulation started at $z = 127$, with initial conditions set by placing the particles in positions consistent with a realization of the predicted linear power spectrum.

An immediate, qualitative, result of the Millenium run is confirming the idea that the large scale distribution of dark matter corresponds to a “cosmic web”. Thus, the topology of the dark matter distribution is complex, composed of an intricate pattern of dark matter clusters and filaments, with typical sizes ~ 100 Mpc at $z=0$. Through these filaments, matter flows into the clusters, increasing their mass. Both clusters and filaments are composed of a multitude of substructures.

This qualitative picture could be confirmed by comparing the output of the simulation with big redshift surveys such as the 2dFRS (Cole et al., 2005). It is also consistent with weak lensing measurements of the dark matter distribution (Massey et al., 2007).

In order to measure the clustering properties of dark matter, the 2-point correlation for the dark matter haloes functions were calculated. These agreed with the ob-

servational data from the 2dFRS in the range from $\sim 2 h^{-1}\text{Mpc}$ to $\sim 20 h^{-1}\text{Mpc}$, well approximated by a simple power law.

At smaller scales, however, the predictions for the dark matter correlation function deviated strongly from the observations of galaxies, which keep a power law behaviour. This shows that the clustering of galaxies is not the same as the one found for dark matter, reminding one that, while galaxy formation occurs in dark matter haloes, this process has a scale dependence leading to more galaxies for some haloes than for others.

In that same paper (Springel et al., 2005) a semi-analytic model (section 3.2) was used to calculate predictions for the actual galaxy correlation function using the merger tree obtained from the Millenium simulation and obtained a good match between observations and predictions, confirming the discussion of the last paragraph.

This illustrates the necessary complementarity between the dark-matter-only *N*-body simulations and the semi-analytic models of galaxy formation. While the former can provide precise information about the structure and distribution of dark matter haloes, the latter can use this information to produce predictions for more direct observable quantities.

3.1.2 *Probing the small scales*

Of particular interest to this thesis is the information that can be obtained about small spatial scales, which requires higher resolutions.

Because of the computational cost of higher resolution simulations, it is usually not feasible to simply increase the resolution of a cosmological simulation of a large volume. At the same time, reducing the volume could lead to the neglect of important environmental effects.

A compromise between a high enough resolution and taking into account the cosmological context can be achieved through *zoom* or *resimulation* techniques. In this kind of simulation, one proceeds in two steps: first, a large cosmological volume is simulated, at low resolution; then, interesting objects are selected for a resimulation. The particles that compose the selected haloes can then be traced back to the beginning of the simulation, identifying the region which gave origin to the selected halo.

This region has its resolution increased by the substitution of the original particles by a large number of particles with smaller mass. The simulation is then rerun.

This kind of procedure, taken to an extreme, allowed the prediction – under the assumption of a neutralino¹ candidate for dark matter – that bound substructures of masses as small as $10^{-6} M_{\odot}$ would survive disruption in the Milky Way halo. These Earth-mass ‘micro-haloes’ would have sizes comparable to the dimensions of the solar system (Diemand et al., 2005).

In the approach of the previous paragraph, it is interesting to evaluate the ability of a small mass halo to resist tidal disruption, but the extreme increase of resolution required restricts the precision of the results on larger scale and numerical difficulties required the simulation to be halted at $z = 26$.

Nevertheless, accurate high resolution simulations of Milky-Way-mass haloes until $z = 0$ have been done. The highest resolution ones were: the *Via Lactea I* and *Via Lactea II* simulations (Diemand et al., 2007, 2008), where a single halo was re-simulated with particle masses $m_p = 2.09 \times 10^4 M_{\odot}$, and the *Aquarius Project* (Springel et al., 2008), where 6 dark matter haloes similar of mass similar to the Milky Way were extracted from the Millennium and re-simulated at resolutions as high as $2 \times 10^3 M_{\odot}$.

The results of both sets of simulations mostly agree. For definiteness, I will list some results from the Aquarius project. It was found that the *subhalo mass function* is well approximated by

$$\frac{dN}{dM} = a_0 \left(\frac{M}{m_0} \right)^n, \quad (3.2)$$

with $n = -1.9$, $a_0 = 3.26 \times 10^{-5} M_{\odot}^{-1}$ and $m_0 = 2.52 \times 10^7 M_{\odot}$. The density profiles obtained for both the dark matter haloes and the subhaloes were compatible with the Einasto profile form,

$$\rho(r) = \rho_{-2} \exp \left(-\frac{2}{\alpha} \left[\left(\frac{r}{r_{-2}} \right)^{\alpha} - 1 \right] \right). \quad (3.3)$$

This same Einasto form is applicable to the radial distribution of the subhaloes, with

¹ The neutralino is the lightest supersymmetric particle in a minimal supersymmetric model, whose mass is $m_{\nu} \sim 100$ GeV (Jungman et al., 1996). Its mass and decoupling energy lead to an exponential cut-off in the power spectrum at ≈ 0.6 comoving parsecs, which results in the mass scale found for the microhaloes.

$\alpha = 0.678$, and $r_{-2} = 0.81r_{200}$, independent of the subhalo mass.

It is interesting to compare the Einasto radial distribution with the cored NFW and isothermal profiles that were assumed for the calculation of the completeness correction factor for the estimation of the luminosity function in section 2.3. When comparing equally normalized distributions, one finds that the Einasto profile presents intermediate behaviour, approaching the cored NFW at large radii and the cored ISO for radii approaching the core radius. Therefore, a similar intermediate behaviour is expected for the luminosity function.

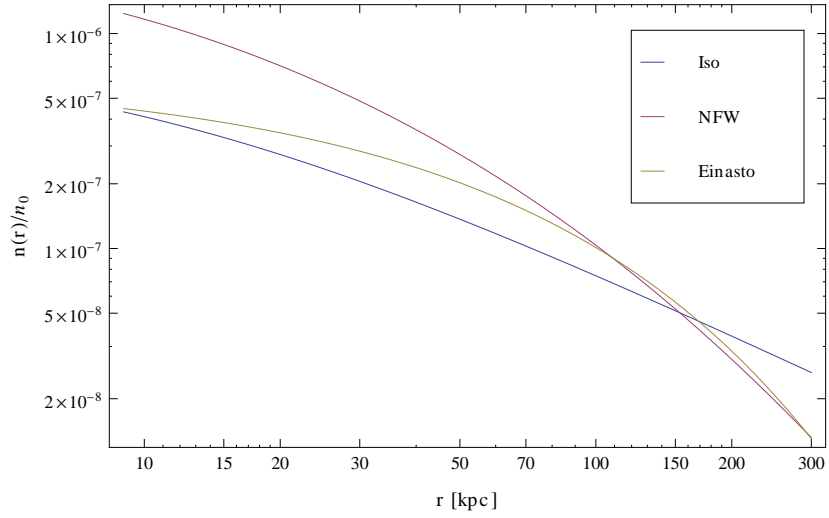


Figure 3.1: Comparison between Einasto, cored-NFW and cored-Isothermal subhalo number density profiles.

3.2 Semi-analytic models of galaxy formation

The technique known as *semi-analytic modeling* of galaxy formation consists in the application, on the merger tree of dark matter haloes, of a set of approximate analytic relations between the properties of galaxies and of the intergalactic gas (Baugh, 2006; Benson, 2010b).

A merger tree is a list of the masses and angular momenta of the haloes that merged in order to form a given halo in the present era (or at a given output redshift), as well as the times of the merger events.

In the context of a semi-analytic model (SAM), the merger tree can either be cal-

culated from an extended Press-Schechter formalism or directly extracted from a cosmological N-body simulation.

Then, all the astrophysical processes involving baryons are coded into approximate analytic relations which involve the properties of whole components of the idealized haloes+galaxies system (e.g. the total stellar mass of a disk or spheroid, the amount hot gas in the halo or the composition of the ISM). Each of these relations have a definite physical meaning with uncertainty coded into free parameters.

This approach allows one to evaluate, with a relatively low computational cost, the joint effect of the many astrophysical processes involved in galaxy formation. Also, due to the way these models are implemented, it is possible to turn on and off (or reduce the effectiveness of) one selected process and in this way to gain insight about its relative importance.

In many parts of this thesis modified version a SAM called GALACTICUS is used. This code, developed by Benson (2010a), features all the physics that can be found in a modern SAM, in a clear and module oriented code that facilitates modifications.

A detailed discussion on this specific version of the code, the personalisations made to it and the fiducial parameter set, can be found in appendix A.

In the following subsections, I discuss some of the fundamental concepts involved in a SAM, illustrating with the actual GALACTICUS (Benson, 2010a) implementation.

3.2.1 *Constructing the merger tree*

The base over which a SAM is developed is a dark matter haloes merger tree (schematically represented in figure 3.2). As was previously mentioned, there are two possible routes to obtain such a tree: one can extract it from a N-body simulation or build it using a Monte Carlo procedure.

The former has the advantage of accurately accounting for environmental effects on the dark matter structure, and allows properties like angular momentum and the actual spatial distribution of haloes to be accessed.

On the other hand, the extraction of the merger tree from simulations has disadvantages too. The resolution of the tree is limited to the resolution of the simulation; the limited number of snapshots – therefore the limited temporal resolution – may

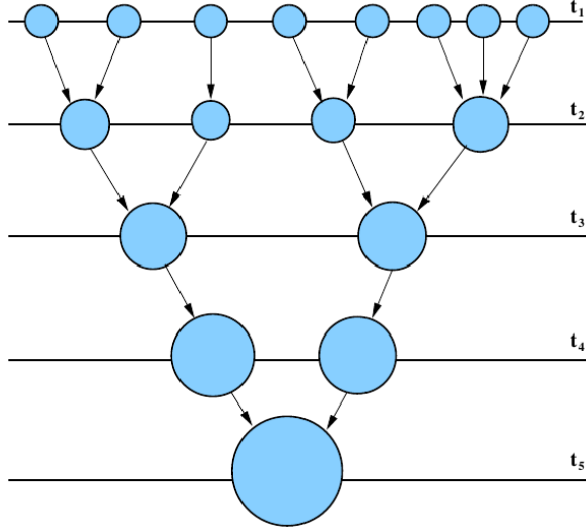


Figure 3.2: A dark matter haloes merger tree.

lead to errors (although these should not be particularly significant, as shown by Benson et al. 2011), and, evidently, there is the computational cost of running a big enough N-body simulation to obtain a significant sample of merger trees.

To generate a Monte Carlo merger tree, the point of departure is the expression obtained by Press & Schechter (1974) predicting the abundance of dark matter haloes:

$$\frac{dn}{dM} = \left(\frac{2}{\pi}\right)^{\frac{1}{2}} \frac{\rho_0}{M^2} \frac{\delta_c(t)}{\sigma(M)} \left| \frac{d \ln \sigma}{d \ln M} \right| \exp \left[-\frac{\delta_c^2(t)}{2\sigma^2(M)} \right] \quad (3.4)$$

where $\rho_0(t)$ is the mean density of the Universe, $\delta_c(t)$ is the critical density contrast necessary for a perturbation to collapse and $\sigma(M)$ is the mass variance, defined by

$$\sigma^2(M) = \int_0^\infty W^2(M, k) P(k, t) k^2 dk \quad (3.5)$$

where $P(k, t)$ is the matter power spectrum and $W(k, M)$ is a window function.

Lacey & Cole (1993) extended the original Press & Schechter formalism allowing an estimate of the distribution of the masses of the progenitors of a given halo. If a halo has mass M_f at a redshift z_f , its progenitors follow a distribution

$$\frac{dN}{dM} = \left(\frac{2}{\pi}\right)^{\frac{1}{2}} \frac{\sigma^2 M_f}{M^2} \frac{\delta_c - \delta_{c,f}}{(\sigma^2 - \sigma_f^2)^{\frac{3}{2}}} \left| \frac{d \ln \sigma}{d \ln M} \right| \exp \left[-\frac{(\delta_c - \delta_{c,f})^2}{(\sigma^2 - \sigma_f^2)} \right], \quad (3.6)$$

where M is the progenitor mass, z is its redshift and $\sigma = \sigma(M)$, $\delta = \delta(z)$, $\sigma_f = \sigma(M_f)$, $\delta_f = \delta(z_f)$.

Any statistical procedure that is able to generate a distribution of progenitors consistent with equation 3.6, can, then, be used to build the merger tree. For example, GALACTICUS uses the algorithm similar² to the one developed by Cole et al. (2000). In this scheme, first the two quantities following quantities are calculated

$$P = \int_{M_{\text{res}}}^{\frac{1}{2}M_f} \frac{dN}{dM} dM \quad \text{and} \quad F = \int_0^{M_{\text{res}}} \frac{dN}{dM} \frac{M}{M_f} dM, \quad (3.7)$$

where M_{res} is minimum mass (the mass resolution of the tree), P is the mean number of fragments with masses in the range $M_{\text{res}} < M < M_f/2$ and F is the fraction of mass in fragments below the resolution limit.

The algorithm involves choosing a redshift interval (or timestep), $dz = z_f - z$, such that $P \ll 1$, ensuring a small chance of multiple fragmentation. Then, a random number R is generated. If $R > P$ then the halo does not fragment from z_f to z . However, there is still the mass gained from the accretions below the resolution limit (which we will refer to as *smooth accretion*). Accounting for that, the mass of the parent halo is calculated as $M = M_f(1 - F)$. If $R < P$, then there is fragmentation, and a simple bipartition is assumed. The first fragment receives a random mass in the range $M_{\text{res}} < M_{p,1} < M_f/2$ while the second receives the remainder mass, i.e. $M_{p,2} = M_f(1 - F) - M_{p,1}$. This procedure is then repeated for each of the parent haloes, building up the tree.

3.2.2 Hot gas accretion

Once the gas was able to decouple from the background radiation, it started falling inside the dark matter haloes. This infall led to shock heating of the gas, resulting in haloes with a gas masses $M_{\text{hot}} = f_g M_{\text{halo}}$. This hot gas is in equilibrium with the halo,

² The actual algorithm GALACTICUS uses is the one described by Parkinson et al. (2008), in which a correction factor $G = G(\sigma/\sigma_f, \delta_f/\sigma_f)$ multiplies the quantities P and F of equation 3.7. With this correction, the method is able to reproduce accurately the merger trees obtained from N-body simulations.

having a temperature

$$T_{\text{vir}} = \frac{2}{3} \frac{GM_{\text{halo}}}{r_{\text{vir}}} \frac{\mu m_H}{k_B} \quad (3.8)$$

where r_{vir} is the virial radius of the halo, μ is the mean molecular weight of the gas, m_H is the mass of a hydrogen atom and k_B is the Boltzmann constant.

When two haloes merge, the hot gas mass in the SAM is summed up and the temperature is updated to the virial temperature of the resulting halo. It is important to notice that in this step, the galaxies inside the merging haloes do not merge, which means that one of the galaxies effectively loses its hot gas halo.

This removal of the hot gas halo of a galaxy when it becomes a satellite galaxy is known as *satellite starvation* (or strangulation) and is a way to model the fact that the *ram pressure* to which a subhalo is subject to typically exceeds the binding energy of its hot gas.

A dark matter halo can also gain mass through the “smooth accretion” – defined in the previous section – which can be understood as a constant sequence of small mergers below the mass resolution limit. Together with the dark matter, gas is accreted from the intergalactic medium at an assumed rate $\dot{M}_{\text{hot}} = f_g \dot{M}_{\text{halo}}$.

The most natural choice for the gas fraction is simply $f_g = \Omega_b/\Omega_{DM}$. However, we will see in sections 6.2 and 7.2 that there are processes that can interfere in the hot gas accretion, leading to a non-trivial form, i.e. $f_g = f_g(z, M_{\text{halo}})$.

3.2.3 Gas cooling and disk formation

The hot gas in pressure equilibrium with dark matter halo is subject to dissipative cooling processes, which lead to the loss of energy and, thus, of pressure support. Since the halo has nonzero angular momentum, the recently cooled gas accumulates itself on a disk in the centre of the halo, which later becomes the disk of a spiral galaxy.

The radiative cooling of the gas is characterized by the *cooling timescale*,

$$\tau_{\text{cool}} = \frac{3}{2} \frac{k_B T n}{\Lambda} \quad (3.9)$$

where n is the number density of gas particles and $\Lambda(\rho, z, T)$ is the cooling function, which in the GALACTICUS case is calculated by the Cloudy code (Ferland et al., 1998).

The cooling timescale is compared with the dynamical timescale, $t_{\text{dyn}} = V_{\text{vir}}/R_{\text{vir}}$, defining the *cooling radius*, r_{cool} , at the point where both match, i.e. $t_{\text{cool}}(r_{\text{cool}}) = t_{\text{dyn}}$.

3.2.4 Quiescent star formation in disks

While there has been some progress, a fully adequate quiescent star formation law is still to be found. Many star formation recipes are motivated by the empirical correlation found by Schmidt (1959) between the surface density of the star formation rate and the projected gas mass distribution, synthesised in the fit made by Kennicutt (1998)

$$\Sigma_{\text{SF}} \propto \Sigma_{\text{gas}}^N, \quad (3.10)$$

where $N \approx 1.4$.

Motivated by observations in the IR and at millimetre wavelengths that indicate that star formation occurs preferentially in giant molecular clouds (e.g. Solomon & Vanden Bout 2005), a different star formation law was proposed by Blitz & Rosolowsky (2006), where the star formation rate is proportional to the amount of molecular hydrogen

$$\Sigma_{\text{SF}} = \nu_{\text{SF}} \Sigma_{\text{H}_2} = \nu_{\text{SF}} f_{\text{mol}} \Sigma_{\text{HI}}, \quad (3.11)$$

where f_{mol} is the fraction of molecular hydrogen in the gas and

$$\nu_{\text{SF}} = \nu_{\text{SF},0} \left[1 + \left(\frac{\Sigma_{\text{HI}}}{\Sigma_{\text{BR}}} \right)^q \right]. \quad (3.12)$$

Blitz & Rosolowsky (2006) propose that f_{mol} is given by a power law of the hydrostatic pressure in the disk plane,

$$f_{\text{mol}} = \left(\frac{P}{P_{\text{BR}}} \right)^\alpha, \quad (3.13)$$

where the constants $P_{\text{BR}} \approx 4.5$ and $\alpha \approx 0.92$ were found by directly fitting observational data and the hydrostatic pressure in the disk is approximated by

$$P = \frac{\pi}{2} G \Sigma_{\text{gas}} \left(\Sigma_{\text{gas}} + \Sigma_{\star} \frac{\sigma_{\text{gas}}}{\sigma_{\star}} \right). \quad (3.14)$$

3.2.5 Galaxy mergers and spheroid formation

In a halo merger event, the galaxies in the smallest mass halo become satellites. This means that, to each satellite galaxy (with its corresponding dark matter halo) a set of random orbital parameters (relative to the galaxy in the centre of the most massive halo) will be attributed – chosen to be statistically consistent with what is observed in N-body simulations (Benson, 2005) and placing the satellite at the virial radius of the host halo.

The satellites orbit will then gradually lose their orbital energy because of dynamical friction and eventually merge with the central galaxy. This is calculated using the formula obtained by Jiang et al. (2008).

When disk galaxies of comparable sizes merge, their disk symmetry is destroyed, generating a spheroidal component instead. The turbulent environment produced by the merger leads to a strong increase in the star formation rate – a *starburst* – and a ready consumption of the gas from the original disk. Depending on the subsequent evolution (namely, the time for the assembly of a new disk), these spheroids can be identified with either elliptical galaxies or bulges of spiral galaxies.

To model merger and starburst events in GALACTICUS, one first makes a distinction between major and minor merger events. In the former case, the satellite and central galaxies have comparable masses, i.e. $M_{\text{satellite}} > f_{\text{major}} M_{\text{central}}$, where f_{major} is a free parameter set to 0.25 in the fiducial model (appendix A). For satellites of smaller masses the merger is considered to be minor.

In a *major merger*, the disk structures of both the satellites and the central are assumed to be destroyed. All the star and cold gas mass is then transferred to the spheroid component of the central galaxy. Since the star formation in bursts is still poorly understood, the following simple model is used to describe its star formation timescale

$$\tau_{\star} = \max \left(\frac{\tau_{\text{dyn}}}{\epsilon_{\star}}, \tau_{\text{min}} \right), \quad (3.15)$$

where $\tau_{\text{dyn}} = R/V$ is the dynamical timescale in the resulting spheroid and $\epsilon_{\star} = 0.008$ is a parameter that characterizes the star formations efficiency and $\tau_{\text{min}} = 1$ Myr is the minimum star formation timescale.

Knowing the star formation timescales, the star formation rate can be readily calculated from it, by dividing the cold gas

$$\psi = \frac{M_{\text{cold}}}{\tau_{\star}}. \quad (3.16)$$

In the case of a *minor merger* the satellite galaxy is not expected to appreciably disrupt the central galaxy. This is modelled by the transfer of the stellar and gas content from the components of satellite to the spheroid of the central galaxy, without any change in the disk of the central galaxy.

3.2.6 AGN feedback

The supermassive black holes located at the centre of galaxies are long known to have their properties correlated with those of their host galaxies. An important and well-known observational result is the Magorrian relation, the correlation between bulge mass and the black hole mass (Magorrian et al., 1998).

These correlations suggest a connection between the growth of the supermassive black hole and the formation of the host galaxy. At the same time, jets produced by the AGN can inject energy into the halo gas and mechanically remove the gas from the spheroid, injecting it back into the halo. These effects are known as *AGN feedback*.

This kind of feedback can explain the exponential cut-off that appears at the bright end of the luminosity function, by the regulation of the formation of galaxies in that range.

3.2.7 Other processes

I postpone the discussion of the supernovae feedback, reionization and magnetic field effects to the following chapters.

3.3 Summary

In this chapter I reviewed some of the techniques used to model the formation of structures and galaxies in the Universe.

Dark matter N-body simulations allow the study of the non-linear gravitational collapse taking into account the cosmological context. From these simulations, it was possible to obtain the mass functions, spatial correlation and density profiles of dark matter haloes.

The use of resimulation techniques allowed probing very small scales, discovering that even haloes less massive than the Local Group present a great amount of substructure.

Semi-analytic models of galaxy formation allow making definite predictions about direct observable properties of galaxies as luminosities, colors and morphologies.

Models of this type use the structural properties obtained from N-body simulations together with simplified equations that model the physics of star formation and the evolution of the interstellar and intergalactic media, codifying uncertainties as free parameters.

Chapter 4

Formulating the satellites problem

“La duda es uno de los nombres de la inteligencia”

Jorge Luis Borges

In section 3.1.1 of chapter 3, it was discussed how N-body simulations made important predictions on large scales. With the increase in computational power and development of techniques as the ones described in section 3.1.2, the investigation naturally proceeded to small scales.

Using high resolution cosmological simulations, Klypin et al. (1999) and Moore et al. (1999) showed that a rich amount of dark matter substructure can survive within dark matter haloes of total virial mass $\sim 10^{12} M_{\odot}$ – same mass scale as the Milky Way halo.

The properties of the small scale substructure resembled what was observed on cluster scale: the central concentration of mass in a given halo was surrounded by an intricate pattern of streams and clumps.

In order to objectively access those properties, it is convenient to define a *subhalo* as a locally overdense set of DM particles that are gravitationally bound to each other and belong to a halo.

In order to measure the deepness of the subhaloes’ gravitational potential without the need of dealing with the frontier of the subhalo (which is subject to considerable uncertainty), it is common to use *maximum circular velocity* of the subhaloes, defined by

$$V_{\max} = \max \left(\frac{G M(< r)}{r} \right)^{\frac{1}{2}}. \quad (4.1)$$

While this quantity is straightforward to be calculated for subhaloes in the sim-

ulations, it can also be obtained for the observed satellite galaxies of the Milky Way and M31. Assuming that the stellar orbits in the dwarf galaxies are isotropic, measurements of the line-of-sight velocity dispersion, σ_{los} , can be converted to maximum circular velocities through $V_{\text{max}} = \kappa \sigma_{\text{los}}$, with $\kappa = \sqrt{3}$.

If each satellite galaxy is embedded in a subhalo and if each subhalo harbours an embedded galaxy (i.e. if light efficiently traces the dark matter distribution on small scales), the distribution of objects with a given V_{max} should coincide for subhaloes and satellites.

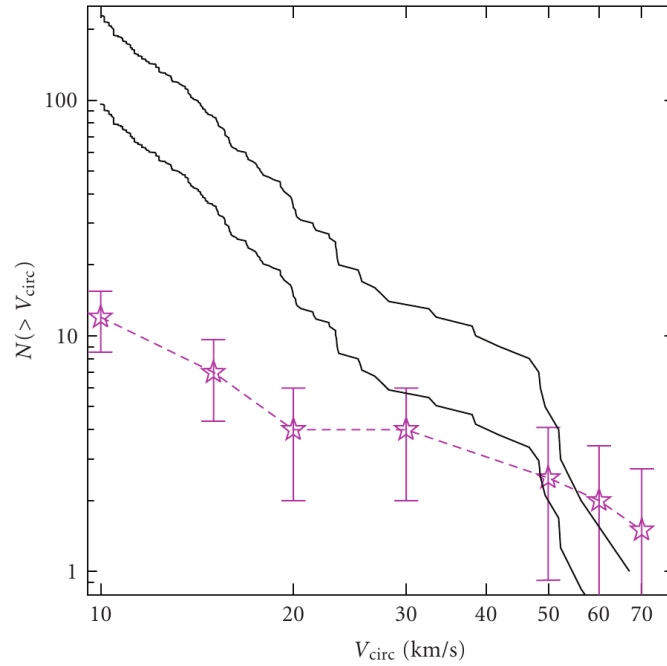


Figure 4.1: Cumulative maximum circular velocity function (CVF) of the Milky Way (classical) satellites and the simulated subhaloes. The dashed curve shows the CVF derived from Local Group data; the continuous top and bottom lines correspond to CVFs of subhaloes in simulations, with host haloes with circular velocities of 208 km/s and 160 km/s. Figure extracted from Kravtsov (2010).

In figure 4.1 we show the comparison between the maximum circular velocity functions (CVFs) obtained from simulations and observations. There is noticeable a lack of agreement in the shape of the CVF, which has a very different slope.

Only classical satellites are taken into account in figure 4.1, because of the uncertainties in the determination of V_{max} for the ultrafaint population. The ultrafaint satellites, however, are expected to have similar circular velocities, $V_{\text{max}} \approx 9$ km/s (Kravtsov, 2010). Thus, despite the slight increase in the number of objects, there

would be still discrepancy in slope of the CWF.

For the sake of definiteness, we quote the expression for the circular velocity obtained by Diemand et al. (2007), consistent with the results obtained by other groups (e.g. Springel et al. 2008).

$$N(> V_{\max}) \propto V_{\max}^{-3}, \quad (4.2)$$

while a power law fit to the data from satellite galaxies¹ gives (Klypin et al., 1999).

$$N(> V_{\max}) = (385 \pm 83) \times \left(\frac{V_{\max}}{10 \text{ km/s}} \right)^{-1.3 \pm 0.4}. \quad (4.3)$$

The assumption $\kappa = \sqrt{3}$, used to determine the circular velocities of the satellites, could be criticized, however, as too simplistic. It can be shown that, both the possible anisotropy in the stellar velocity dispersion tensor and for of the density profile would affect κ , changing V_{\max} by a factor of up to 2 or 3 (Peñarrubia et al., 2008).

As an alternative, instead of quantifying the mass content of galaxies using maximum circular velocities, one can determine the mass up to a fixed radius, $M(< R)$. Choosing small enough values for R , this approach leads to $M(< R)$ with a reduced the dependence with the properties of the (unknown) mass profile of the galaxy. At the same time, for sufficiently high resolutions, it is possible to unambiguously determine $M(< R)$ for the simulated subhaloes.

In figure 4.2, adopted from Strigari et al. (2007), we show the cumulative 0.6 kpc inner mass function obtained for the Milky Way satellites and the comparison with results of a cosmological N-body simulation. Again, the simulations predict a number of low mass objects much higher than what is observed.

The Missing Satellites Problem This discrepancy, between the number of satellite galaxies and the predicted number of subhaloes of compatible mass, loosely defines what became known in the literature as ‘the missing satellites problem’ (Kravtsov, 2010; Bullock, 2010). More precisely, the missing satellites problem can be understood as a discrepancy not only in the absolute number of objects, but in the slope of mass functions.

¹ Taking into account all classical satellite galaxies in the Local Group, i.e. satellites of both M31 and the Milky Way.

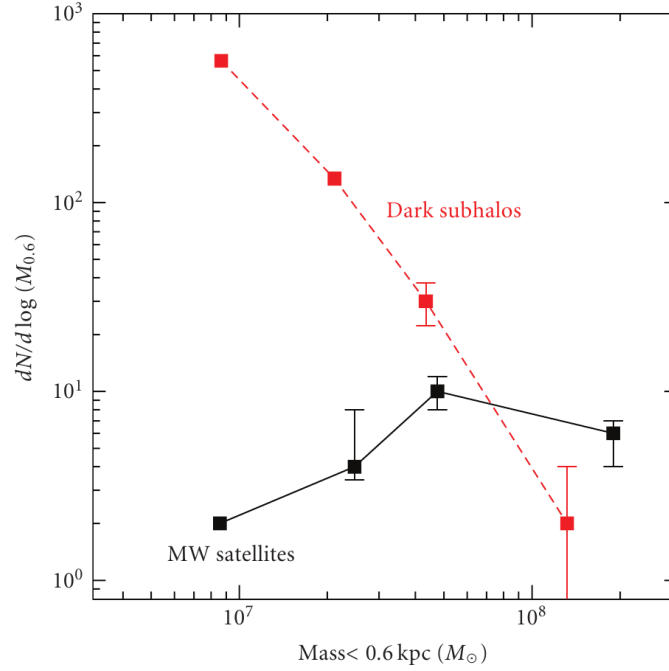


Figure 4.2: Cumulative inner mass function of the Milky Way satellites and the simulated subhaloes. Extracted from Strigari et al. (2007).

Tentative solutions to the missing satellites problem involve mainly three approaches:

1. Claiming that the observations are incomplete and biased, and that the discrepancies disappear when the bias and incompleteness are taken into account (Tollerud et al., 2008; Bullock et al., 2010);
2. Attributing the discrepancy to a real lack of subhaloes, which can be consequence of a non-standard dark matter model or of non-standard initial power spectrum (Zentner & Bullock, 2003);
3. Explaining the the discrepancy through an astrophysical mechanism that suppresses the formation of small galaxies (e.g. Macciò et al., 2010; Font et al., 2011).

It is unlikely that the incompleteness in the observations could fully solve itself the missing satellites problem, since – as it was discussed – the discovery of new ultrafaint galaxies would not alter the shape of the mass or circular velocity functions appreciably. Nevertheless, the limitations of observation are an important factor that must be taken into account.

If the answer to the missing satellites problem is of type 3, most subhaloes remain

dark, making the comparison between mass functions inappropriate – as the light-traces-mass hypothesis is no longer valid.

One alternative is to focus on more direct observables as the luminosity function which can be calculated by any model that tries to implement solution 3, and allows to test the tentative solution of type 1, since (as discussed in section 2.3) it can be corrected for the incompleteness. In fact, a shift towards examining the luminosity function and other observables (as the metallicity-luminosity relation) can be seen in the literature in the last decade.

Even solutions of type 2, are still required to correctly predict the observed properties of satellite galaxies, and would thus benefit from a comparison with more direct and/or reliable observables as the luminosity function.

The problem of the detection of “dark” subhaloes (or the lack of them) can be perceived as separate – and possibly more difficult – problem, which involves detailed study of the dynamical implications of the population of dark subhaloes on the rest of the system and/or subtle measurements of the lensing effects of those objects

In fact, at present, the only observational evidence of substructure in galactic haloes comes from the observation of flux anomalies in four-image gravitational lenses. The existence of these discrepancies in the fluxes measured for the multiples images of a same quasar is interpreted as been caused by the presence of substructures in the lens and allows the estimation of the fraction of substructure in the lens once a mass function is assumed (Dalal & Kochanek, 2002; Kochanek & Dalal, 2004).

Bearing in mind those considerations, I advocate that the missing satellites problem should be divided into two different (albeit complementary) aspects, which can be formulated explicitly as:

Satellites problem Which galaxy formation (and cosmological) model can predict the correct luminosity function of the satellite galaxies? Does it correctly predict other properties as the relation between the mass and the metallicity? Does it predict the observed constant inner mass? Do the satellite galaxies from this model populate subhaloes of masses compatible with what is observed?

Substructure problem Are there dark matter subhaloes? How do they affect the dynamics of the Local Group? How do they influence dark matter annihilation signal? Is it possible to detect them by gravitational lensing effects?

Because of the lack of reliable observational data allowing a clear treatment of the substructure problem, in the remainder of this thesis I focus solely on the satellites problem.

Chapter 5

Initial power spectrum distortions

*“Und schnell und unbegreiflich schnelle
Dreht sich umher der Erde Pracht;
Es wechselt Paradieses-Helle
Mit tiefer schauervoller Nacht;”*

Johann W. von Goethe

In the chapter 4 we have formulated the “missing satellite galaxies problem”, which can also be understood as “the excess of dark matter subhaloes problem”. In this chapter, we examine one class of tentative solutions, which questions the existence of the dark matter substructures obtained in the simulations discussed in chapter 3. As we have seen, those models rely on assumptions about the primordial power spectrum of density perturbations: namely, they assume a nearly scale invariant primordial power spectrum.

The motivation for this assumption is not unclear. On the theoretical side, a nearly scale invariant primordial power spectrum is the natural outcome of the simplest conceivable inflationary models (for a review, see Liddle & Lyth 2000). On the observational side, we find that both CMB (Komatsu et al., 2011) and large scale structure (Cole et al., 2005) are consistent with an initial power spectrum described by a simple power law with spectral index close to 1, hence, nearly scale invariant.

Nevertheless, the smallest scales of the power spectrum have not yet been *directly* probed. Thus, if the satellite galaxies population correctly traces the underlying mass distribution, the lack of satellites can be interpreted as evidence, albeit indirect, of a lack of power on the small scales.

I discuss here two classes of mechanisms that lead distortions in the initial power

spectrum. In section 5.1, I examine distortions generated by features in the inflaton potential, giving a simple example of a modified inflationary potential that leads to suppression of formation in the correct mass range (these results were originally published in Rodrigues & Opher 2010). In section 5.2 I briefly review how warm dark matter particles could alter the power spectrum in a similar way. Finally, in section 5.3 I show what is the predicted impact, on properties of galaxies, of a break in the initial power spectrum.

5.1 Features in the inflationary potential

Inflation has become an essential part of our description of the universe. It solves the classical cosmological problems of flatness, horizon and relics, and also provides precise predictions for the primordial density inhomogeneities, predictions that are in good agreement with data of the CMB anisotropies (Komatsu et al., 2011).

Despite these successes, the specific details of inflation are still unknown, since many different physical mechanisms and fields may generate a phase of accelerated cosmic expansion. For simplicity, it has become common practice to employ a scalar field, *the inflaton*, with a simple law for its potential, to generate inflation. This picture is usually understood as the effective counterpart of a deeper – and probably more complicated – theory. In this context, the most generally employed inflationary theory is the so-called chaotic inflation, characterized by a simple quadratic potential with an initial high field value for the inflaton.

Recently, due to advances in data quality and in anticipation of the data from the Planck satellite (The Planck Collaboration, 2006) and the Large Synoptic Survey Telescope (LSST Science Collaboration, 2009), for example, several groups started investigating more complicated forms for the inflaton potential to explain the present observational data. Pahud et al. (2009) used the CMB data to look for the presence of a general sinusoidal oscillation imprinted on the inflaton potential, for large field values (i.e., large spatial dimensions), placing strong limits on the amplitude of these oscillations. Ichiki & Nagata (2009) found – with a 99,995% confidence level – an oscillatory modulation for large spatial dimensions at $k \simeq 0.009 \text{ Mpc}^{-1}$, performing a Monte-

Carlo Markov-Chain analysis using the CMB data, confirming similar results obtained from the analysis of the CMB data using different techniques (Ichiki et al., 2009).

Theoretically, features in the inflaton potential are well motivated. Adams et al. (1997) showed that a class of models derived from supergravity theories gives rise to inflaton potentials with a large number of steps, each of these corresponding to a symmetry-breaking phase transition in a field coupled with the inflaton. Also, many transplanckian effects may generate oscillations in the primordial power spectrum of density inhomogeneities which could be described by an effective oscillating inflaton potential (Brandenberger & Martin, 2001; Martin & Brandenberger, 2003).

Bearing in mind the growing the plausability of oscillating features in the inflaton potential, the consequences, to the number of small dark matter haloes, of a simple localized oscillating modification of the inflaton potential for small field values are studied in the next subsections. In particular, it is shown that a non-negligible effect can be attained even restricting the analysis to the simple case of perturbations that remain in the slow-rollover regime.

5.1.1 The slow-roll formalism: a reminder¹

The primordial universe is assumed to be filled by an approximately homogeneous scalar field, the *inflaton*, governed by a Klein-Gordon equation of motion

$$\ddot{\phi} + 3H\dot{\phi} + \frac{dV}{d\phi} = 0 \quad . \quad (5.1)$$

The Friedmann equation becomes

$$\left(\frac{\dot{a}}{a}\right)^2 = \frac{8\pi}{3m_{pl}^2} \left[V(\phi) + \frac{1}{2}\dot{\phi}^2 \right] . \quad (5.2)$$

In order to have an inflationary period, the second derivative of the field and the kinetic term of the Friedmann equation must both be small when compared with the

¹ In this subsection a rather succinct review of the slow-roll inflationary formalism is made. For a more comprehensive treatment, reader is referred to, for example, Liddle & Lyth (2000).

other terms. This can be obtained under the conditions of slow-roll,

$$\epsilon \equiv \frac{1}{8} \left(\frac{V'(f)}{V(f)} \right)^2 \ll 1 \quad (5.3)$$

and

$$\eta \equiv \frac{1}{4} \left(\frac{V''(f)}{V(f)} \right) \ll 1 \quad , \quad (5.4)$$

where the following notation was used

$$f \equiv \frac{\sqrt{8\pi}}{m_{pl}} \phi \quad \text{and} \quad V'(f) \equiv \frac{dV}{df} \quad . \quad (5.5)$$

The comoving wavenumber, k , of each mode of the spectrum of density perturbations can be related to value of the inflaton field, f , at the time this mode was leaving the Hubble sphere using

$$\frac{k}{a_0 H_0} = \exp[60 - N(f)] \quad (5.6)$$

with

$$N(f) = 4 \int_{f_e}^f \frac{V}{V'} df \approx (f^2 - 1/2) \quad . \quad (5.7)$$

The approximation used in Eq. (5.7) is justified by the fact that the assumed deviations of the chaotic inflaton potential ($V \propto f^2$) are very small (the interesting deviations, shown in section 5.1.4 are of order 5%).

The dimensionless curvature power spectrum, $\mathcal{P}_{\mathcal{R}}$, is related to the inflaton potential, in the slow-roll approximation, by

$$\mathcal{P}_{\mathcal{R}}(k) \propto \frac{V^3(f(k))}{V'^2(f(k))} \quad , \quad (5.8)$$

and the normalization of the power spectrum that will be used is the one obtained from WMAP5 (Hinshaw et al., 2009).

From $\mathcal{P}_{\mathcal{R}}$ it is possible to obtain \mathcal{P}_{δ} , the power spectrum of the density perturbations using (Liddle & Lyth, 2000)

$$\mathcal{P}_{\delta}(k, t) = \left[\frac{2(1+w)}{5+3w} \right]^2 \left(\frac{k}{a(t) H(t)} \right)^4 T^2(k) \mathcal{P}_{\mathcal{R}} \quad (5.9)$$

where w is the equation of state parameter of the dominant component at instant t .

For the transfer function, $T(k)$, the analytical fit obtained by Eisenstein & Hu (1998) is used. This fit takes into account the presence of dark energy and baryons.

5.1.2 The mass function

The mass function gives the number density, $n(m)$ of DM haloes of mass between m and $m + dm$. In order to calculate this quantity, it is first to obtain the variance from the expression

$$\sigma^2(R, t) = \int_0^\infty W^2(k, R) \mathcal{P}_\delta(k, t) \frac{dk}{k} \quad (5.10)$$

where, for simplicity, a Gaussian window function was adopted, i.e.

$$W^2(k, R) = \exp(-k^2 R^2) . \quad (5.11)$$

In order to evaluate the mass function at the present time, we set in equation 5.9

$$a(t)H(t) = a_0 H_0 = (2997.9)^{-1} h \text{ Mpc}^{-1} . \quad (5.12)$$

Using the Press & Schechter (1974) formalism, we have

$$n(m) dm = -\frac{\bar{\rho}}{m} \sqrt{\frac{2}{\pi}} \frac{\delta_c(t)}{\sigma^2} \frac{d\sigma}{dm} \exp\left(\frac{-\delta_c^2}{2\sigma^2}\right) dm , \quad (5.13)$$

where $\delta_c \approx 1.61$ is the critical density contrast, $\bar{\rho}$ is the average density of the universe and the mass, m , is related with the length, R , from the expression

$$R(m) = \sqrt{\frac{1}{2\pi}} \left(\frac{m}{\bar{\rho}}\right)^{\frac{1}{3}} . \quad (5.14)$$

5.1.3 Modified potentials

The modified potential that will be referred to as ‘saw-tooth’ is constructed by substituting the small field part of the quadratic potential by an oscillatory linear modification.

This potential is shown in figure 5.1 and can be simply defined as follows: let λ be

the wavelength of the oscillation and f_a the field when the modification begins, for $f > f_a$, $V(f) = Af^2$; for $f < f_a$ we define $f_n = f_a - f n \lambda$.

For $f_n - \frac{1}{4}\lambda < f \leq f_n$, the potential has the form,

$$V(f) = A \frac{f_n^2 - (1-b) \left(f_n - \frac{1}{4}\lambda\right)^2}{\frac{1}{4}\lambda} + Af_n^2, \quad (5.15)$$

for $f_n - \frac{1}{2} < f \leq f_n - \frac{1}{4}\lambda$,

$$V(f) = A \frac{(1-b) \left(f_n - \frac{1}{4}\lambda\right)^2 - \left(f_n - \frac{1}{2}\lambda\right)^2}{\frac{1}{4}\lambda} \left(f - f_n + \frac{1}{4}\lambda\right) + A(1-b) \left(f_n - \frac{1}{4}\lambda\right)^2, \quad (5.16)$$

for $f_n - \frac{3}{4} < f \leq f_n - \frac{1}{2}\lambda$,

$$V(f) = A \frac{\left(f_n - \frac{1}{2}\lambda\right)^2 - (1+b) \left(f_n - \frac{3}{4}\lambda\right)^2}{\frac{1}{4}\lambda} \left(f - f_n + \frac{1}{2}\lambda\right) + A \left(f_n - \frac{1}{2}\lambda\right)^2, \quad (5.17)$$

and for $f_{n+1} < f \leq f_n - \frac{3}{4}\lambda$,

$$V(f) = A \frac{(1+b) \left(f_n - \frac{1}{4}\lambda\right)^2 - \left(f_n - \frac{1}{2}\lambda\right)^2}{\frac{1}{4}\lambda} \left(f - f_n + \frac{1}{4}\lambda\right) + A(1+b) \left(f_n - \frac{1}{4}\lambda\right)^2. \quad (5.18)$$

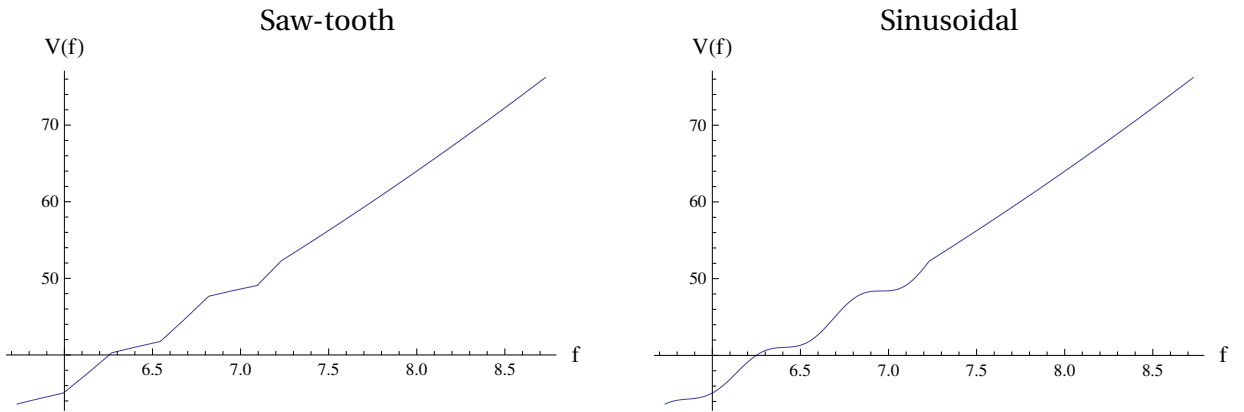


Figure 5.1: Saw-tooth and sinusoidal potentials, with $b = 0.025$ and $\lambda = 0.55$.

We take $f_a = 7.232$ in order to obtain changes in the variance for mass scales $M \lesssim 10^8 M_\odot$. We are in the parameter space region of slow-roll inflation. The part of the parameter space which allows for this regime – i.e., where the slow-roll parameters (equation 5.3 and equation 5.4) are smaller than 1 – is shown in figure 5.2.

We also analyse the case when the modification of the potential is a simple sine

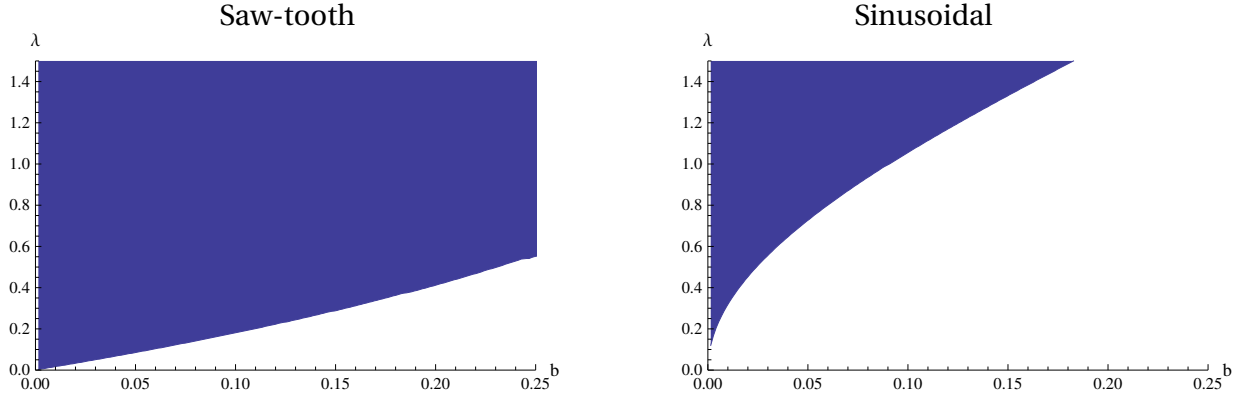


Figure 5.2: The shaded areas indicate the regions of the parameter space, (λ, b) , where the saw-tooth and sinusoidal potentials are compatible with slow-roll inflation.

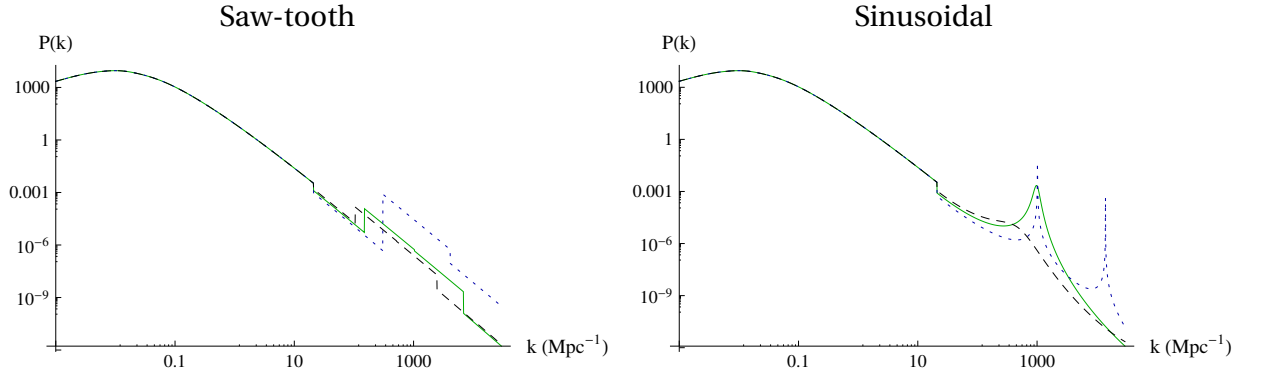


Figure 5.3: Matter power spectrum obtained in the context of the modified inflation model. In the left-hand panel, the power spectrum obtained using a saw-tooth modification to the inflaton potential with different values of b and λ . In the right-hand panel, the sinusoidal modification is used. The continuous (green) curves correspond to $b = 0.025$ and $\lambda = 0.55$; the dotted (blue) curves, to $b = 0.050$ and $\lambda = 0.75$, and the dashed (black) curves, to $b = 0.015$ and $\lambda = 0.45$.

wave,

$$V(f) = \begin{cases} Af^2 \left[1 + b \sin \left(\frac{2\pi f}{\lambda} \right) \right] & , f \leq f_a \\ Af^2 & , f > f_a \end{cases} \quad (5.19)$$

which is shown in the right panel of figure 5.1. The regions of the parameter space which admit slow roll are shown in 5.2.

5.1.4 Results

The power spectrum of density perturbations, $P(k) = 2\pi^2 \mathcal{P}_\delta(k)/k^3$, was calculated following equation 5.9, for both the sinusoidal and sawtooth potentials, the results are shown in figure 5.3.

In Fig. 5.4 we plot the ratio of the mass function obtained from the saw-tooth potential to the mass function of a featureless quadratic potential (i.e., $n_{\text{saw-tooth}}(m)/n_{\text{ch}}(m)$)

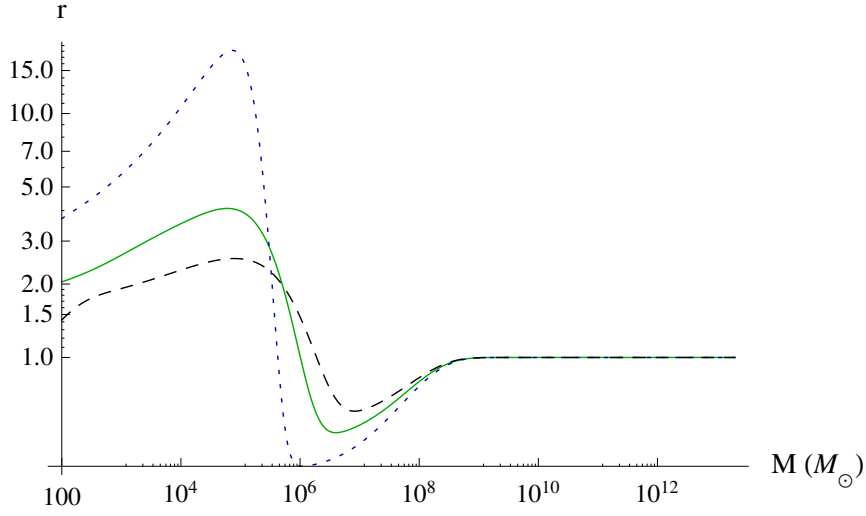


Figure 5.4: Ratio $r = n_{\text{saw-tooth}}(m)/n_{\text{chaotic}}(m)$. The continuous (green) curve corresponds to $b = 0.025$ and $\lambda = 0.55$; the dotted (blue) curve, to $b = 0.050$ and $\lambda = 0.75$, and the dashed (black) curve, to $b = 0.015$ and $\lambda = 0.45$.

), for different values of the parameters b and λ , with b varying from 1.5% to 5%.

When using parameters $b = 0.05$ (i.e., a 5% modification of the chaotic potential) and $\lambda = 0.75$, we find a 47% suppression in the number of haloes for masses between 10^7 and $10^8 M_\odot$.

In Fig. 5.5 we plot the ratio of the mass function obtained from the sinusoidal potential to the mass function of a featureless quadratic potential, again for different values of the parameters b and λ . Using parameters $b = 0.05$ and $\lambda = 0.75$, we find a 54% suppression in the number of haloes for masses between 10^7 and $10^8 M_\odot$.

A small amplitude ($b = 5\%$) saw-tooth oscillatory inflaton potential, with a “wavelength” $\lambda = 0.75$, causes a factor of $\sim 1/2$ decrease in the number of haloes of masses $10^7 - 10^8 M_\odot$.

The conclusion is that even small modifications to the inflaton potential can cause large changes in the predicted halo mass function. In particular, we show that plausible simple oscillatory modifications can lead to suppression of the number of haloes in the mass range typically associated with the dwarf galaxies of the Milky Way. This specific potentials also lead to an appreciable increase² in the number of haloes of mass $< 10^6 M_\odot$ by factors $\sim 15 - 60$.

In section 5.3, the consequences of this toy model to the formation of small galaxies

² This increase in the number of haloes in this small mass range may be interesting to a complementary astrophysical problem: the formation of population III stars.

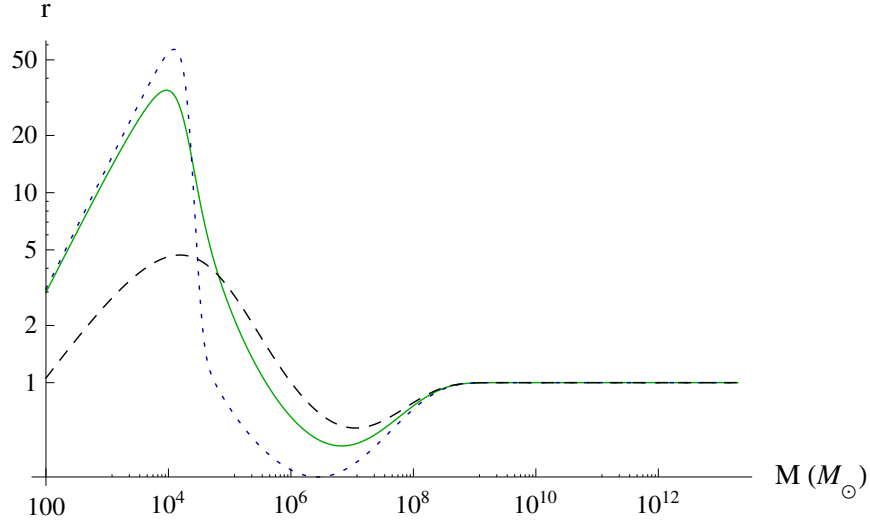


Figure 5.5: Ratio $r = n_{\text{sin}}(m)/n_{\text{chaotic}}(m)$. The continuous (green) curve corresponds to $b = 0.025$ and $\lambda = 0.55$; the dotted (blue) curve, to $b = 0.050$ and $\lambda = 0.75$, and the dashed (black) curve, to $b = 0.015$ and $\lambda = 0.45$.

is further examined.

5.2 Warm dark matter

Even in the context of a standard inflationary scenario producing initially a scale-invariant featureless power spectrum, it is possible to obtain a damping on small scales because of the properties of the dark matter particles.

The phenomenon involved is known as *free streaming*. During the radiation-dominated epoch, the growth of any density perturbation is suppressed. Thus, before the energy equipartition between matter and radiation, the collisionless dark matter particles can stream out of the overdense regions, smoothing out the inhomogeneities.

To take this effect into account properly, it is necessary to solve the Boltzmann equation for the dark matter component. However, it is possible to estimate the free streaming length scale by simply calculating the length scale that a particle would be able to travel from its decoupling (assuming it is a thermal relic) until the equipartition time.

The free streaming scale of a dark matter particle of mass m_W and abundance

$\Omega_W h^2$, is given by (Zentner & Bullock, 2003)

$$\lambda_{\text{FS}} \approx 0.11 \left(\frac{\Omega_W h^2}{0.15} \right)^{\frac{1}{3}} \left(\frac{m_W}{1 \text{ keV}} \right)^{-\frac{4}{3}} \quad (5.20)$$

and this change produces a sharp cut in the power spectrum, given approximately by (Bardeen et al., 1986)

$$P(k) = P_0(k) \times \exp \left[-k\lambda_{\text{FS}} - (k\lambda_{\text{FS}})^2 \right] \quad (5.21)$$

where P_0 is the power spectrum without damping.

If the dark matter particle is light enough, its free streaming length is non-negligible, and depending on the mass of the particle, there will be a suppression effect in the power spectrum similar to the one produced by inflation in the previous section. This defines *Warm Dark Matter*.

5.3 Effects on galaxy properties

The reduction in the number of small haloes does not, by itself, solve the satellites problem. It is necessary to check whether a model constructed with a non-trivial primordial power spectrum would predict galaxy properties in agreement with the ones discussed in chapter 2.

In order to understand how features in the primordial power spectrum may affect the properties of galaxies, I ran GALACTICUS semi-analytic model using an initial power spectrum with a sharp suppression. Thus, the initial power spectrum employed had the simple following form

$$P(k) = \begin{cases} \vartheta k^{n_s} & , k \leq k_{\text{break}} \\ s \times \vartheta k^{n_s} & , k > k_{\text{break}} \end{cases} \quad (5.22)$$

where k_{break} is the wavenumber above which the suppression takes place, $s = 0.25$ is the suppression parameter and the normalization constant, ϑ , is chosen in order to obtain the correct value for σ_8 .

This modified power spectrum was used as input for the GALACTICUS semi-analytical

model and compared with the fiducial model. Initially, a low resolution run covering the whole mass range (see table A.1 in the appendix) was made. As a result, the present b_J luminosity function could be calculated. The results are shown in figure 5.6.

As it could be anticipated, this observable is not significantly affected by the break in the initial power spectrum: the only changes are the oscillations due to numerical noise. The same hold for other observables as the stellar mass function and HI mass function.

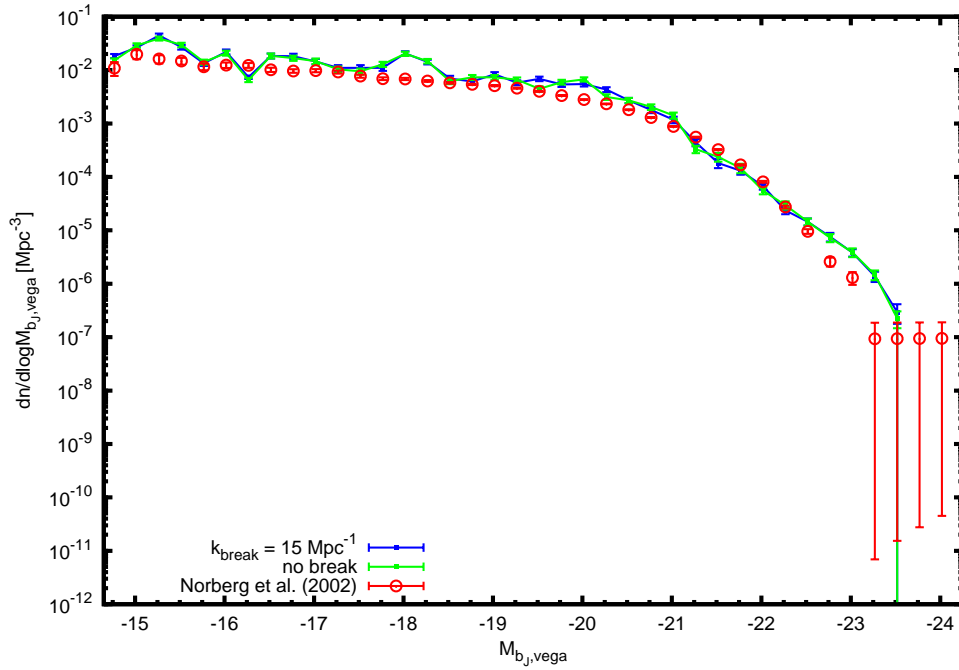


Figure 5.6: Effect of a 25% suppression of the power spectrum at wavenumbers greater than $k_{\text{break}} = 15 \text{ Mpc}^{-1}$ on the b_J luminosity function.

The code was ran again, this time using a higher resolution and processing only merger trees corresponding to final dark matter halo masses similar to that of the Milky Way (i.e. in the range between $5 \times 10^{11} M_{\odot}$ and $5 \times 10^{12} M_{\odot}$). In order to assure further similarity with the Milky Way system, merger trees where no central bright galaxy could found were discarded (for a more detailed discussion, see appendix A).

The resulting V -band luminosity function for the satellite population of a Milky-Way-like galaxy is shown in figure 5.7. Around $M_V = -7$, the modified power spectra lead to reduction of 50% in the number of galaxies relative to the fiducial case, allowing a good match between the model and the observations.

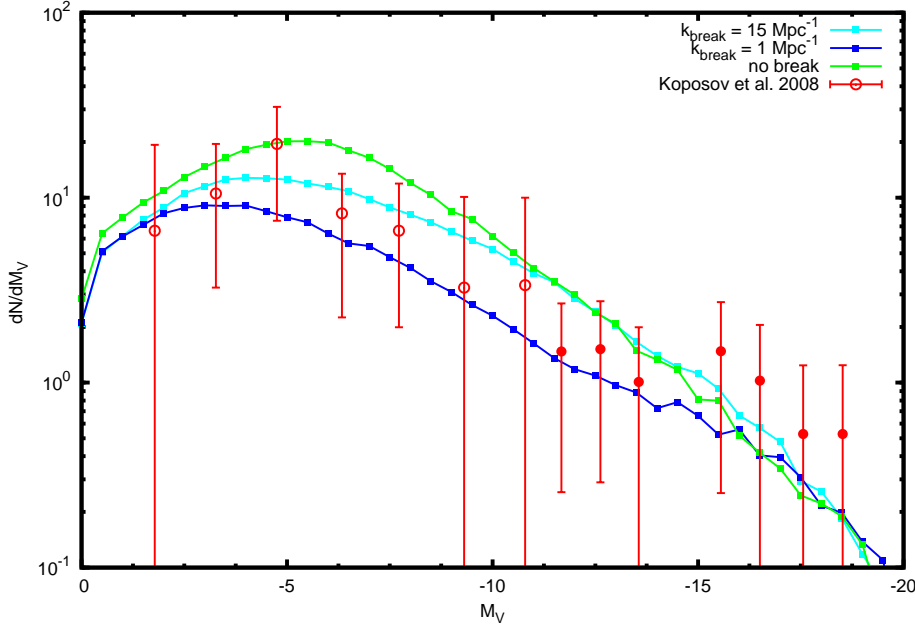


Figure 5.7: Effect of a suppression of the power spectrum on the V luminosity function of the satellites of MW-like galaxies.

To further study the consequences of the modified initial power spectrum on the satellite population, it is examined, in figure 5.8, the effect on the luminosity-metallicity relation. It can be seen that the suppression in $P(k)$ leads to an increase in the metallicity of the faint galaxies.

This change is explained by the fact that the SNe feedback (which will be further discussed in section 6.1) is more effective in smaller haloes. This leads to a bigger gas outflow, which in turn removes from the galaxy a greater fraction of the newly formed heavy elements, consequently slowing down the chemical enrichment. In the models with modified initial power spectra, the haloes inhabited by faint galaxies are typically more massive, therefore have less outflow, hence have more metal enrichment.

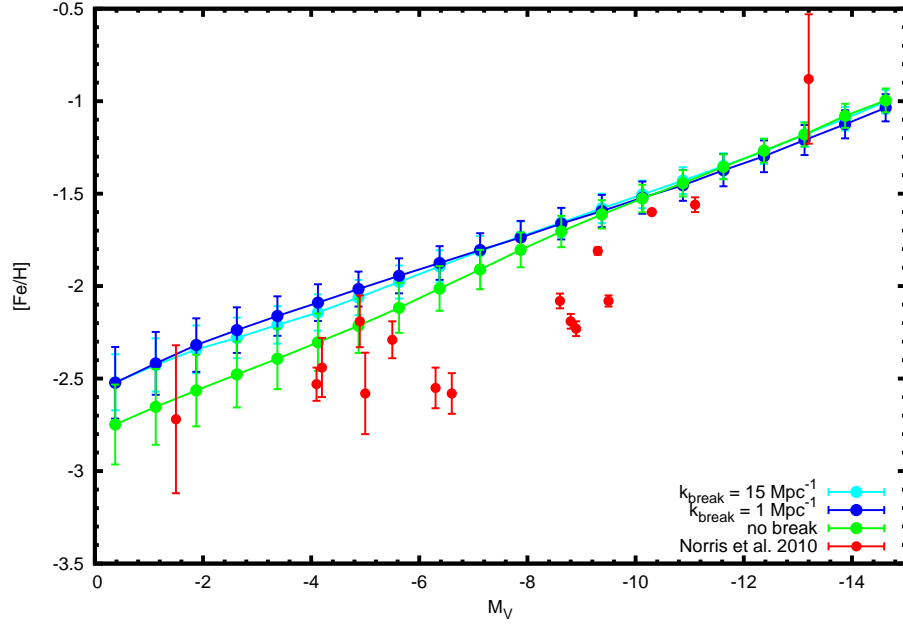


Figure 5.8: Effect of a suppression of the power spectrum on the the Metallicity-Luminosity relation of the satellites of a MW-like galaxy.

5.4 Summary and discussion

In the beginning of this chapter, I showed how a simple oscillatory change in the inflaton potential could lead to a distortion in the initial power spectrum and the reduction in the amount of dark matter substructure. Albeit simple, this specialized potential can be the effective counterpart of, for example, multi-field inflation model (which sometimes lead to discontinuities in the potential or its derivative). The amplitude of the superimposed modification is also extremely small.

It was, then, reviewed how warm dark matter models could lead to similar effects, due to the larger free-streaming length, which leads to the suppression number of structures bellow a specific mass scale.

Finally, I test whether a break in the power spectrum would have other consequences to the galaxy formation process. It was shown that the break leads to no contradiction between models and observations on large mass scales and enhances the match for the predictions of the luminosity function of the satellite galaxies of sys-

tems similar to the Milky Way. This confirms and extends the naïve intuition that a model with break in the initial power spectrum allows the prediction of the correct number of faint satellites.

However, to completely solve the satellites problem, the metallicity-luminosity relation has also to be correctly predicted. There is a non-negligible change in the metallicity-luminosity relation: with the absence of very small mass haloes, there is also a lack of low metallicity faint galaxies. Nevertheless, it is still necessary to improve the recipes for chemical enrichment, since neither the standard model, nor the model with a break in $P(k)$ were able to predict the correct shape for the metallicity-luminosity relation.

Chapter 6

SNe feedback and reionization

“Raffiniert ist der Herrgott, aber boshaft ist er nicht.”

Albert Einstein

In chapter 5 we studied how the features in the primordial power spectrum could alleviate the missing satellites problem and what are the physical mechanisms that could generate such features.

We found out that these changes in the initial power spectrum may lead to a suppression in the number of substructures and allow the prediction of the correct luminosity function. That approach, however, is burdened by addition of more complex inflationary physics or non trivial warm dark matter particle.

An alternative explanation for the discrepancies between the predictions of Λ CDM-based models and the observations may reside in the feedback processes involved in galaxy formation. Thus, the predicted number and properties of the dark matter subhaloes population may be correct but a baryonic physical process may be strongly suppressing the formation of a bright galaxies in small mass haloes.

In this chapter we analyse two processes which are traditionally associated with the regulation of low mass galaxy formation: the feedback from supernovae (section 6.1) and the effects of reionization (section 6.2).

Magnetic fields, a third type baryonic process that may influence the formation of dSph, will be discussed separately – in greater detail – in chapter 7.

6.1 Supernovae feedback

The supernovae explosions lead to energy and momentum injection in the interstellar medium. Part of this energy results in the removal of gas from the galaxy.

In GALACTICUS, as in most SAMs, the supernovae feedback in the disk or spheroid component is modelled through the following expression for the rate at which the gas is outflowed

$$\dot{M}_{\text{out}} = \dot{M}_{\star} \left(\frac{V_c}{V} \right)^{\alpha}, \quad (6.1)$$

where V is the maximum circular velocity of the component at its scale radius, \dot{M}_{\star} is the star formation rate and V_c and α are free parameters.

To further understand equation 6.1, let us assume (following the reasoning exposed by Benson 2010b; Murray et al. 2005) that a fraction ζ of the supernovae energy is transferred to gas that flows out of galaxy with escape velocity. Assuming that the rate at which the energy is released by supernovae is proportional to the star formation rate¹ (i.e. that the formation of SNe is *instantaneous*), we find $\dot{E}_{\text{released}} = \dot{M}_{\star} E_{SN}$, where E_{SN} is the energy of a supernova explosion, thus

$$\frac{1}{2} \dot{M}_{\text{out}} V_{\text{esc}}^2 = \zeta E_{\text{released}} = \zeta \dot{M}_{\star} E_{SN},$$

therefore

$$\dot{M}_{\text{out}} = \dot{M}_{\star} \frac{2\zeta E_{SN}}{V_{\text{esc}}^2}, \quad (6.2)$$

where V_{esc} is the escape velocity of the component.

Because $V \propto V_{\text{esc}}$, equation 6.2 is nothing more than a special case of equation 6.1, corresponding to the choice $\alpha = 2$.

This apparently natural choice for the α parameter, may be misleading. Murray et al. (2005), for example, studies how the momentum from the supernovae explosion

¹ In a more realistic treatment, one can take into account the delay between the formation event of a stellar population and the actual time at which the massive stars become supernovae. Then, one would get

$$\dot{E}_{\text{released}} = \int_{\text{formation}}^t dt' \dot{M}_{\star}(t') \dot{E}_{SN}(t - t').$$

Since this time delay is much smaller than the other timescales, this approximation is usually safe.

can drive the outflow winds. They estimate the maximum momentum deposition as

$$\dot{P} \sim 2 \times 10^{33} \text{ g cm s}^{-2} \left(\frac{\dot{M}_\star}{1 \text{ M}_\odot \text{ yr}^{-1}} \right). \quad (6.3)$$

The momentum input can be related to the outflow mass rate through $\dot{P} \approx \dot{M}_{\text{out}} V_{\text{esc}}$, what leads us to $\alpha = 1$, i.e.

$$\dot{M}_{\text{out}} \propto \dot{M}_\star \times V_{\text{esc}}^{-1}. \quad (6.4)$$

Typically, because of the lack of clarity in the details about how supernovae feedback operates – considering the complexity involved in realistically modelling the interaction between the SN remnants and the ISM – most SAMs leave the exponent as a free parameter. For some SAMs values $\alpha \approx 2$ seem to work (e.g. Baugh et al. 2005, Kang et al. 2005). Nevertheless, many others need higher values, with $\alpha \approx 3$, to correctly fit observations (e.g. Bower et al. 2006, Benson & Bower 2010).

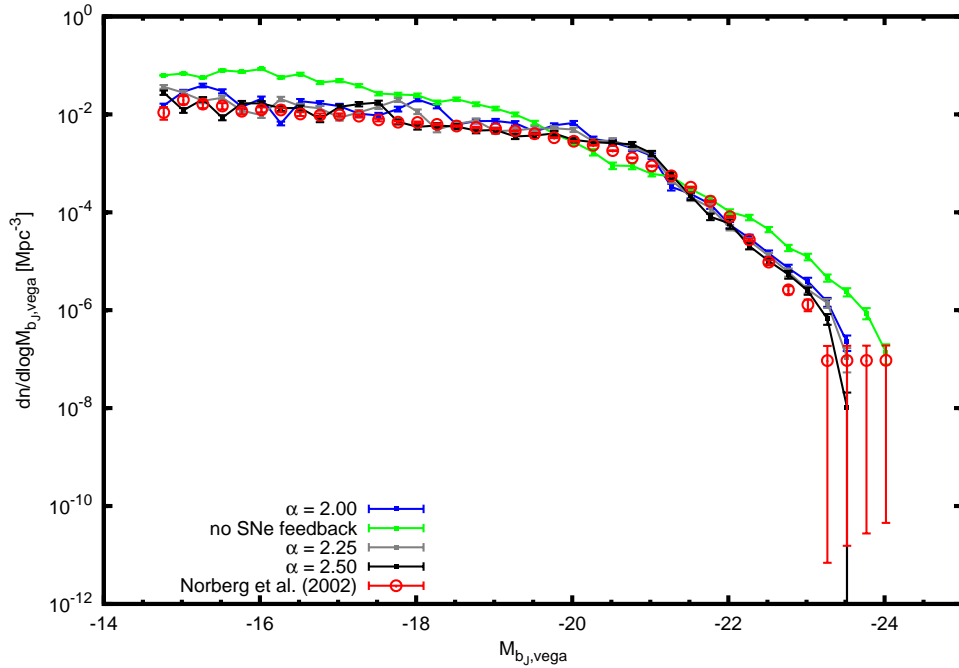


Figure 6.1: SNe feedback effects on the b_J Luminosity Function.

To illustrate the impact of SNe feedback on the properties of galaxies, I ran GALACTICUS with this process disabled (setting $V_c = 0$) and compared with the cases of $\alpha = 2$, $\alpha = 2.25$ and $\alpha = 2.5$. As in the study of the modifications to the initial power spec-

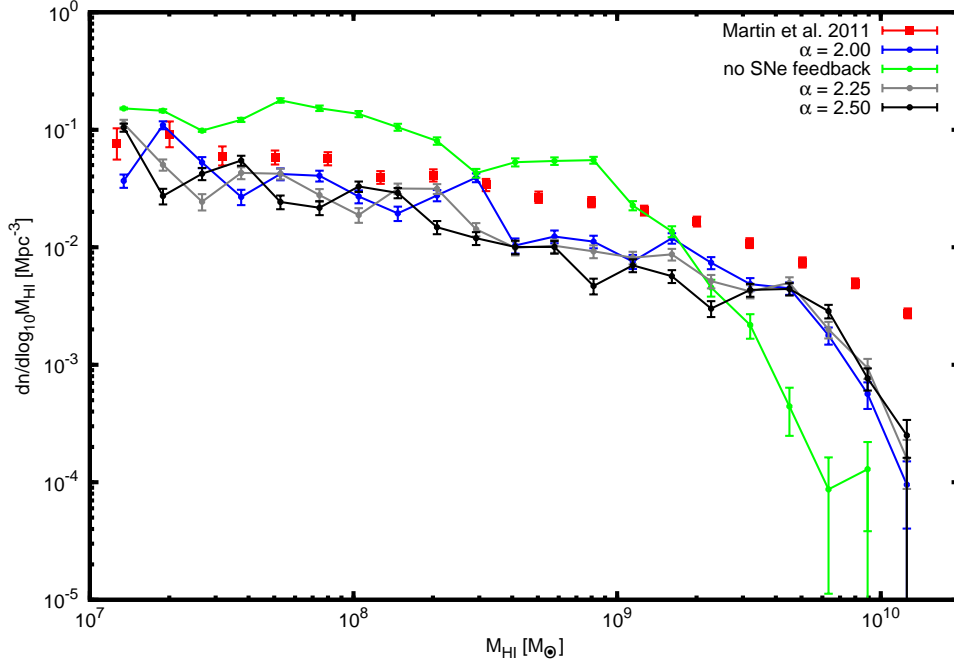


Figure 6.2: Effect of changing α on the HI Mass Function

trum, for each test two runs were made: a low resolution run covering the full mass range and a high resolution run focusing on Milky-Way-like haloes.

In figure 6.1, the overall b_J -band luminosity function is displayed. The outflow of gas due to SNe feedback suppresses the star formation in small mass haloes and its absence results in an excess in the faint end of the luminosity function. This can be confirmed looking into the HI mass function, figure 6.2, which show an excess of cold gas in the switched-off case².

It can be seen that the variation of the α parameter does not significantly affect the properties of the overall galaxy population. This does not hold true if one looks specifically at the satellite population.

In figure 6.3, it is shown the V -band luminosity function of the satellites of a halo similar to the Milky Way's. One notices that, in the absence of SNe winds, the luminosity function peaks at $M_V \approx 11$. In the presence of SNe generated outflows, the luminosity function is deformed, with both the position of the peak and the normalization being functions of α and V_c .

² To obtain the HI mass function, the cold gas mass function was calculated from the output file and multiplied by a factor 0.54 following Power et al. (2010).

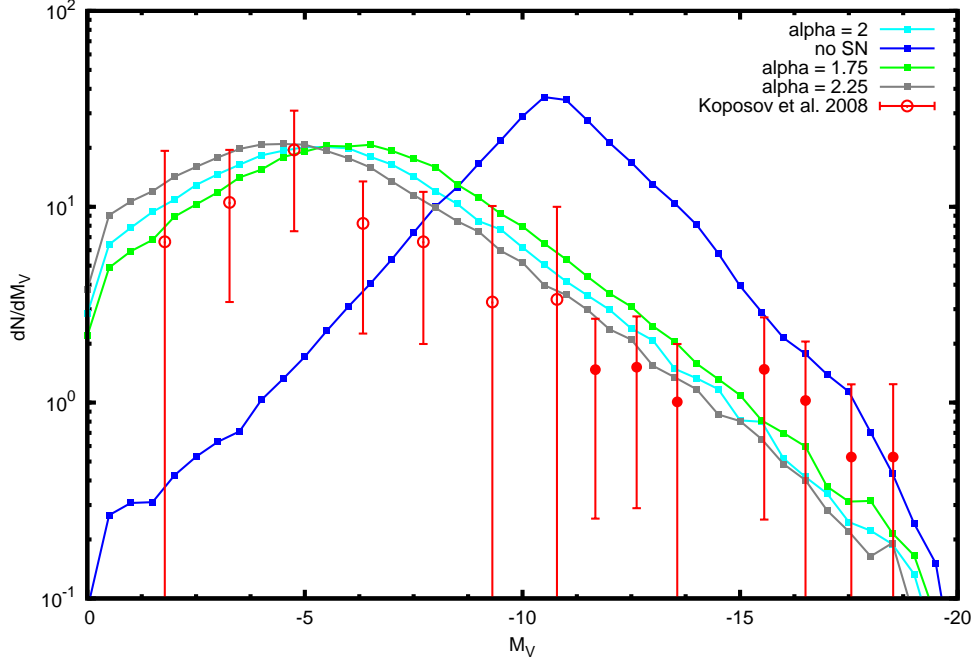


Figure 6.3: Effect of changing α on the V Luminosity Function of the satellites of MW-like galaxies.

Thus, SNe feedback is required to allow the prediction of the correct shape of the luminosity function. Besides that, a high enough choice of α leads to a reduction in the number of faint galaxies and allowing a good match between predicted and observed values.

To find out more about this possibility, it was studied what would be the effect of the different choices of α on the luminosity-metallicity relation. This is shown in figure 6.4, where it can be seen that α regulates the overall normalization of this relation.

Unsurprisingly, the outflows slow down the metal enrichment, with higher values of α leading to a lower metal content. The absence of SNe feedback, on the other hand, leads to an implausible highly metallic satellite population.

6.2 Reionization

Another astrophysical process that has significant influence on galaxies of smaller mass is the reionization of the Universe.

At $z \approx 1100$, after the recombination, the Universe was approximately neutral, filled mainly by HI. The first stars that formed (and possibly also quasars) emitted

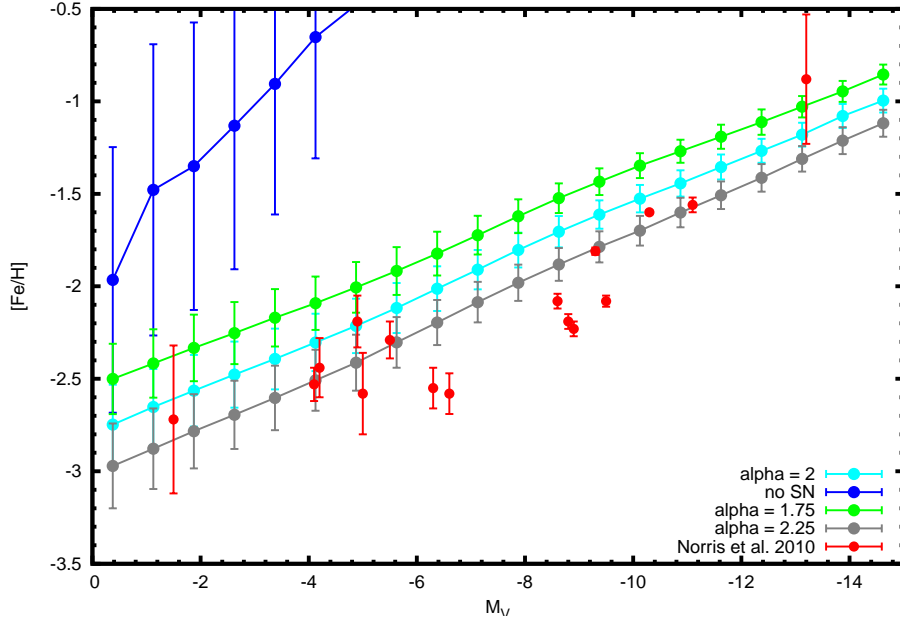


Figure 6.4: Effect of changing α on the Metallicity-Luminosity relation of the satellites of a MW-like galaxy.

enough UV radiation to ionise the interstellar medium gas around them, creating bubbles of ionized gas (Strömgren spheres). Eventually, these growing bubbles would merge together, gradually ionizing all the interstellar and intergalactic media (Loeb & Barkana, 2001).

The UV background responsible for reionizing the intergalactic medium (IGM) also heats it. This affects the galaxy formation picture delineated in chapter 3 in two ways:

1. The heating of the IGM increases its pressure. This extra thermal pressure will interfere with the accretion of gas by the dark matter haloes.
2. The ionizing background reduces the rate of radiative cooling of the gas inside the dark matter haloes.

The second effect can be modelled by taking into account the photon background in the calculation of the cooling function whose form is altered by reionization. Typically, considering the photoionizing background leads to reduction in $\Lambda(T)$ for temperatures below $T \sim 10^4$ K (see, for example, figure 1 of Benson et al. 2002).

While far from negligible, this effect is not – typically – as dramatic in its influence on small mass galaxy formation as the first one, on which I will focus in the rest of this

exposition.

At first sight, the effect 1 should be simple to model: intuitively, the increase in the IGM temperature would lead to an increase in the Jeans mass, avoiding collapse of structures bellow it. But does this picture hold in the non-linear regime?

Using a set of hydrodynamical simulations Gnedin (2000) showed that the gas fraction, f_g (defined in section 3.2.2), is well described by the expression

$$f_g(M_h, z) = \frac{\Omega_b/\Omega_m}{[1 + (2^{1/3} - 1) M_c(z)/M_h]^3} \quad (6.5)$$

where M_h is the halo mass and $M_c(z)$ is a characteristic mass – which corresponds to the mass of a halo whose gas content is 50% of the universal gas fraction.

In that same work, it was found that M_c does not correspond to the Jeans mass, but instead to the *filtering mass*, M_F .

The filtering scale is the characteristic length scale over which the baryonic perturbations are smoothed out as compared to the dark matter ones (Gnedin & Hui, 1998), defined as

$$\frac{\delta_b}{\delta_{tot}} = 1 - \frac{k^2}{k_F^2} + O(k^4) , \quad (6.6)$$

where δ_b is the density contrast of baryonic matter and δ_{tot} , the total density contrast. For k comparable to k_F , the density contrast δ_b is severely depressed.

It is possible to relate the comoving wavenumber associated with this length scale with the Jeans wavenumber, k_J by the equation

$$\frac{1}{k_F^2(t)} = \frac{1}{D(t)} \int_0^t dt' a^2(t') \frac{\ddot{D}(t') + 2H(t')\dot{D}(t')}{k_J^2(t')} \int_{t'}^t \frac{dt''}{a^2(t'')} , \quad (6.7)$$

where $D(t)$ is the growth function of the density perturbations and

$$\frac{k_J}{a} = \left(\frac{4\pi G\rho}{c_s^2} \right)^{1/2} . \quad (6.8)$$

under the assumption of a flat and matter-dominated universe the expression becomes more legible:

$$\frac{1}{k_F^2(a)} = \frac{3}{a} \int_0^a \frac{da'}{k_J^2(a')} \left[1 - \left(\frac{a'}{a} \right)^{\frac{1}{2}} \right] , \quad (6.9)$$

which, using $M_F \equiv \frac{4\pi}{3} \rho \left(\frac{2\pi a}{k_F} \right)^3$, can be written as

$$M_F^{\frac{2}{3}} = \frac{3}{a} \int_0^a da' M_J^{\frac{2}{3}}(a') \left[1 - \left(\frac{a'}{a} \right)^{\frac{1}{2}} \right]. \quad (6.10)$$

Therefore, we (reassuringly) find that the filtering mass consists of an special case of a weighted time-average of Jeans mass.

Despite the clear physical motivation of the “filtering mass formalism” presented above and its widespread application on SAMs (e.g. Benson et al., 2002; Macciò et al., 2010), more recent high resolution simulations show that this description may be not fully correct.

Okamoto et al. (2008) show that M_F overestimates the characteristic mass (see also, Hoesft et al. 2006) and suggest different – rather more complex – prescription to the modelling of reionization. In this picture, the mass of baryons accreted to a halo is given by

$$M_b = \begin{cases} \frac{\Omega_b}{\Omega_0} M_h & , T_{\text{vir}} \geq T_{\text{acc}} \\ \sum_i \xi_i M_{b,i} & , T_{\text{vir}} < T_{\text{acc}} \end{cases} \quad (6.11)$$

where $M_{b,i}$ is the mass of the i^{th} progenitor and the sum is made over all progenitors.

Also, $T_{\text{acc}} \equiv \max(T_{\text{IGM}}, T_{\text{eq}})$, with T_{IGM} being the temperature of IGM gas adiabatically compressed to the density of accreting gas and T_{eq} is the equilibrium temperature at which radiative cooling balances photoheating for gas at the density expected at the virial radius.

The factor ξ_i are defined as

$$\xi_i = \begin{cases} \exp(-\delta t_i / t_{\text{evp},i}) & , T_{\text{vir},i} < T_{\text{evp},i} \\ 0 & , T_{\text{vir},i} \geq T_{\text{evp},i} \end{cases}, \quad (6.12)$$

where δt_i is the time since the last merger of the i^{th} progenitor; $t_{\text{evp},i} \equiv \frac{r_{\text{vir},i}}{c_s(\Delta_{\text{evp}})}$ is the timescale for evaporating gas from it, and T_{evp} corresponds to the equilibrium temperature of gas at an overdensity $\Delta_{\text{evp}} = 10^6$.

From the procedure described above, Okamoto et al. (2008) were able to calculate a

characteristic mass $M_c(z)$ that led to a gas fraction consistent with the results obtained in the high resolution simulation. This $M_c(z)$ differs from $M_F(z)$ by a factor of ≈ 10 for $z = 0$ and gets near to the filtering mass for higher redshifts.

An alternative – more pragmatic – approach, first employed by Macciò et al. (2010), is to simply apply a correction, $\gamma(z)$, to the filtering mass in order to re-establish its agreement with the simulations. In that case, the gas fraction is described equation 6.5, using

$$M_c(z) = \gamma(z)M_F(z) \quad \gamma(z) = (1+z)^{1.1}/11.8. \quad (6.13)$$

In what follows we will use this scheme, which allows us to retain our intuitions about the Jeans and filtering masses without losing too much accuracy at low redshifts. Bearing in mind that this is less than a perfect solution, we will provide tests on the impact of γ .

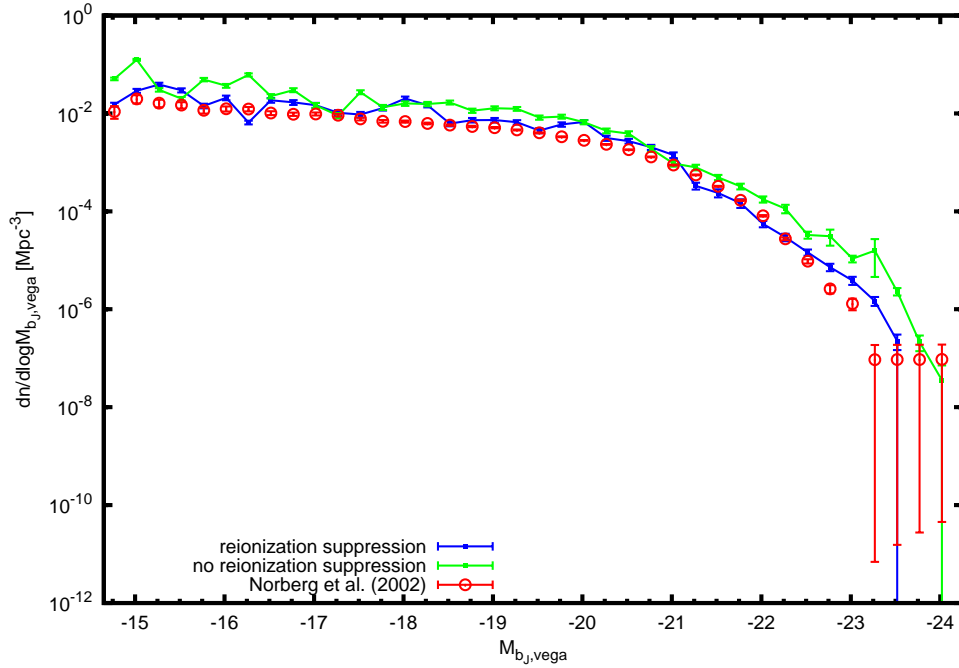


Figure 6.5: Effect of reionization on the b_J Luminosity Function.

In figure 6.5, the b_J luminosity function is shown in the presence and absence of reionization suppression (using a low resolution run as it was described in the previous section). As expected, the effect is more important in the faint end, where the

galaxies have small masses, thus more prone to have the gas accretion suppressed by the thermal pressure.

In order to do this calculation, the temperature variation of the IGM was parametrized following Kravtsov et al. (2004)

$$T(z) = \begin{cases} T_{\text{rei}} \left(\frac{1+z_s}{1+z} \right)^\alpha & , \quad z > z_s \\ T_{\text{rei}} & , \quad z_s \geq z \geq z_r \\ T_{\text{rei}} \left(\frac{1+z}{1+z_r} \right) & , \quad z < z_r \end{cases} \quad (6.14)$$

where $T_{\text{rei}} = 10^4$ K, $z_s = 11$ corresponds to the redshift of the beginning of the reionization and $z_r = 10$ and to redshift of complete reionization.

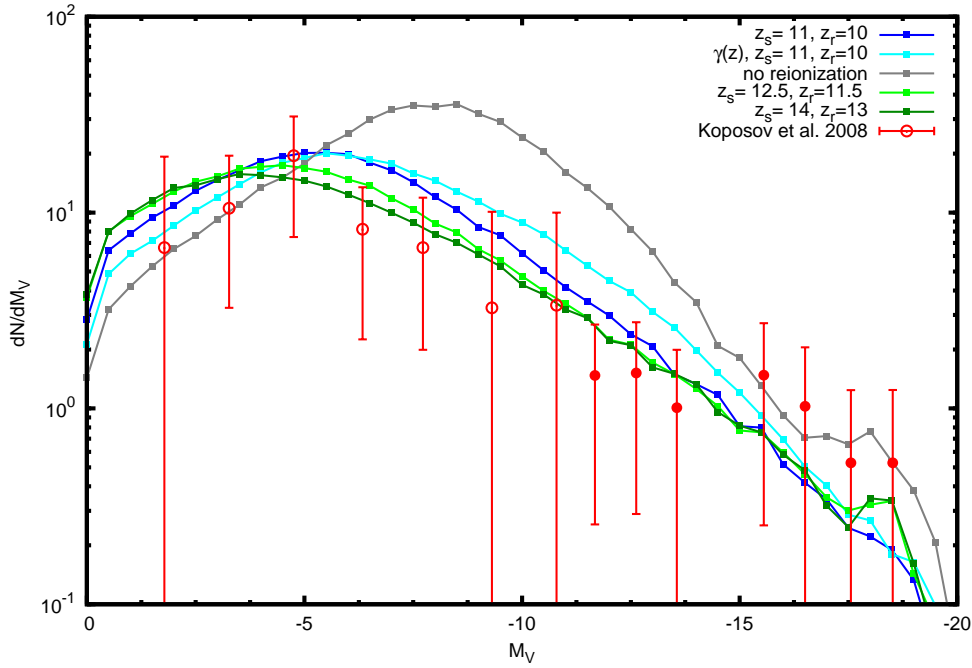


Figure 6.6: Effect of reionization on the V luminosity function of the satellites of MW-like galaxies.

The photoionizing background is key to obtain the correct properties for the satellite galaxies population. In figure 6.6, it is displayed the V -band luminosity of the satellites of a Milky-Way-like galaxy, obtained from using a high resolution GALACTICUS run.

Without reionization the model is – as in the no-SNe-feedback case – unable to

produce the correct shape for the luminosity function, leading to the prediction of an excess of galaxies with magnitudes $M_V \sim 8$.

The $\gamma(z)$ correction leads to a small increase in the number of bright satellites ($M_V \sim 14$) but has little effect on the faint population. This happens because these small haloes accrete most of their baryons at higher redshifts (when $\gamma \approx 1$) and then merge into larger systems. This makes them lose their hot gas haloes because of the ram pressure of the central galaxy (the “starvation” mentioned in section 3.2.2), and after that, mechanisms that influence on the hot gas accretion will stop playing any role to that galaxy.

It can also be seen in figure 6.6 that while the choice of values of $z_r = 10$ and $z_s = 11$ – which are consistent with the WMAP 7 year observations (Komatsu et al., 2011) – do not lead to the correct number of dwarf galaxies. In order to allow an agreement between the observed and predicted luminosity functions, an earlier reionization epoch is required.

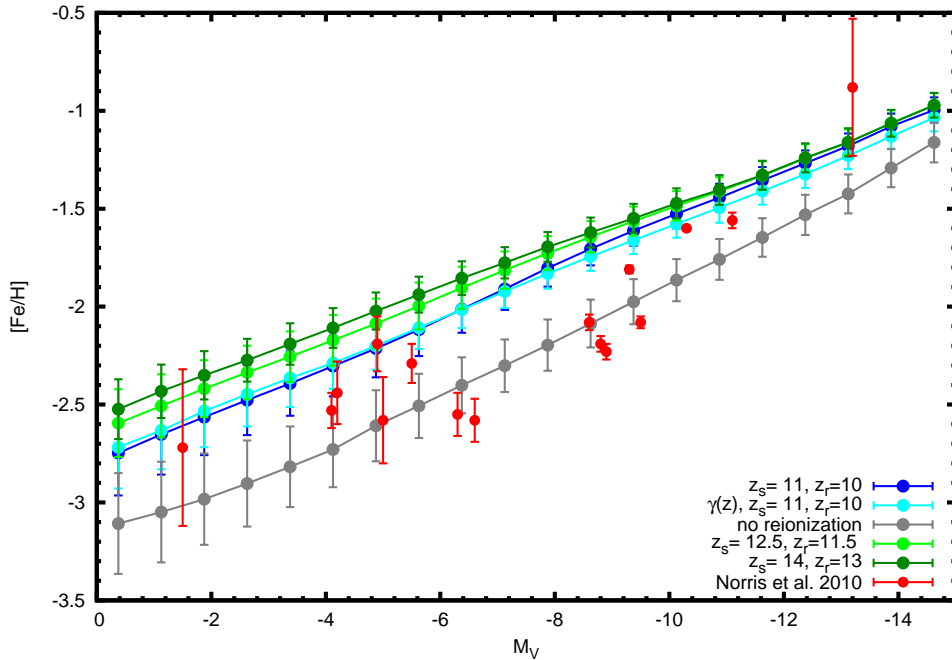


Figure 6.7: Effect of reionization on the Metallicity-Luminosity relation of the satellites of a MW-like galaxy.

The suppression of gas accretion due to the photoionizing background will also affect chemical evolution of the dwarf galaxies, as it is displayed in figure 6.7. It can

be seen that without reionization the metal content of the satellite population is increased.

This is an intriguing result. One could expect that the reduction in the gas accretion caused by the magnetic fields would lead to an earlier halt in the star formation, resulting in a less enriched galaxy population.

Nevertheless, result is explained by the fact that the gas accretion suppression results in less stars, and thus in less luminosity for haloes of a particular mass.

Thus, galaxies whose brightnesses are in the same magnitude bin in the different runs will inhabit haloes of different mass: if a magnitude bin is associated with haloes of typical mass M_r in a run with reionization suppression, that same magnitude bin will correspond to a more massive halo, with $M_{nr} < M_r$, in a run where reionization suppression was switched off.

Since more massive haloes can retain their metal more efficiently, this results in the increase in the metal content for the faint galaxies population.

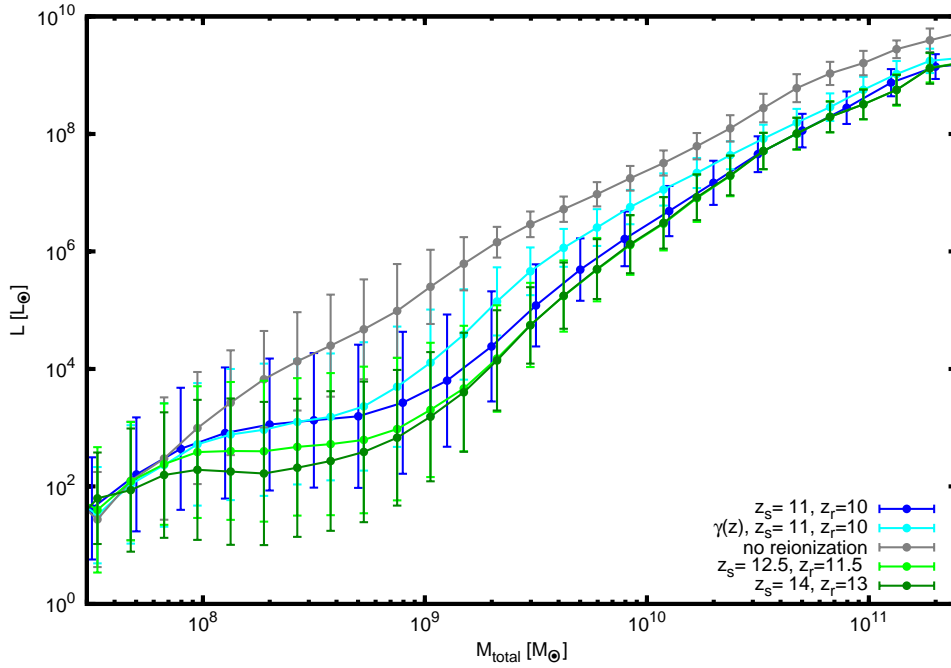


Figure 6.8: The effect of reionization on the mass-luminosity relation of satellite galaxies.

To further clarify this issue, it is worth looking at the mass-luminosity (M - L) relation, shown in figure 6.8. Without reionization the subhalo mass relates to the lumi-

luminosity of its galaxy through a simple power law, $L/L_{\odot} \propto (M_{\text{total}}/M_{\odot})^{2.1}$. When reionization suppression is taken into account, the luminosity is reduced about by factor of 10 in the more massive subhaloes and there is an approximate plateau in the M - L relation for subhalo masses between $10^8 - 10^9 M_{\odot}$.

6.3 Summary and discussion

In this chapter, two mechanisms important for the regulation of the formation of satellite galaxies were discussed: the outflows of gas produced by supernovae explosions and the suppression of gas accretion during the reionization epoch.

Both processes suppress the formation of faint galaxies and interfere with the shape of the luminosity function, reducing its amplitude and moving its peak to the fainter end.

A good match between the predicted and observed satellite luminosity function can be obtained by relaxing the constraints on the parameters of the SNe feedback, choosing an $\alpha \sim 2.5$. This, however, contradicts the simple energetic arguments presented, which imply $1 \leq \alpha \leq 2$.

Reionization, too, can be adjusted with the purpose of allowing a match between the predicted and observed satellite luminosity functions. This leads, however, to a reionization redshift significantly lower than what is observed.

The consequences of those two processes to the luminosity-metallicity relation were also studied. Interestingly, it was found that these processes alter the relation in opposite ways: increasing the SN feedback in order to obtain a match of the luminosity function leads to a decrease in the stellar metallicity for the galaxies of a given magnitude, while the increase in the effect of photoheating by the ionizing background leads to an increase in the metallicity for that same magnitude.

Magnetic fields and galaxy formation

Magnetic fields seem to be an ubiquitous feature of the Universe. Their presence can be observed in almost every considered astrophysical scale. From planets to clusters of galaxies we find magnetic fields playing important – sometimes crucial – roles in the dynamics and evolution of the system.

Two important tools for the observation of Galactic and extragalactic magnetic fields are: the synchrotron emission of free relativistic electron – whose intensity measures the total field strength and polarization measures the fields orientation – and the Faraday rotation due to the propagation of electromagnetic radiation through an ionized medium. Another important observational tracer is the Zeeman splitting of spectral lines, although this effect is usually too small to be used in extragalactic context.

The observed magnetic field near the solar neighbourhood has a strength of circa $6 \mu\text{G}$, while the inner part of the Galaxy and the centre of other spiral galaxies have $B \sim 10 \mu\text{G}$ (Beck, 2008). Magnetic fields are also detected in clusters of galaxies, with values between $\sim 1 \mu\text{G}$ and $\sim 10 \mu\text{G}$ at the centre of cooling cores (Govoni & Feretti, 2004).

There are two major possible explanations for the observed field values: either the magnetic field is of fully primordial origin, having being amplified through adiabatic compression during protogalactic cloud collapse (Grasso & Rubinstein, 2001); or – more likely – the observed magnetic field values are the result of dynamo amplification processes in the galactic environments (Widrow, 2002; Carilli & Taylor, 2002).

Even the in the second case, however, some mechanism is required to generate the

seed fields that the dynamo will amplify. Primordial magnetic fields are, again, strong candidates for these seed fields.

Despite being routinely observed and of their possible importance, magnetic fields have not been taken into account by any major galaxy formation model¹. In this chapter, I discuss one possible influence of magnetic fields to galaxy formation, that turns out to be of importance to the satellite galaxy problem. I focus on the consequences of the existence of primordial/seed fields on the accretion of gas by haloes and on the properties of the satellite galaxies that inhabit a halo of similar to the Milky Way halo.

In section 7.1, I briefly review our knowledge about primordial magnetic fields; in section 7.2, is shown how the presence of such a field would influence the filtering mass (these results were previously presented in Rodrigues, de Souza & Opher 2010; de Souza, Rodrigues & Opher 2011). In section 7.3 I use the GALACTICUS semi-analytic model to study in more detail the consequences of the modified filtering mass on the properties of the satellite galaxies population (this results will appear in Rodrigues, Baugh & Opher 2011).

7.1 *Primordial Magnetic Fields*

In this work, the term “primordial magnetic fields” designates magnetic fields whose properties are similar over large spatial scales ($\sim c H^{-1}$) and which were generated through some common process in the early Universe (i.e. $z \gg 100$).

The QCD and electroweak phase transitions in the early universe present good conditions for the generation of primordial magnetic fields. During these events, fundamental changes in the nature of particles occur and a significant amount of free energy is released in a short period of time, conditions that can naturally produce electric currents and magnetic fields (Subramanian, 2008; Hogan, 1983; Cheng & Olinto, 1994; Ahonen & Enqvist, 1998).

Natural fluctuations of the early universe’s plasma could also produce magnetic fields. de Souza & Opher (2008, 2010) showed that the application of the Fluctuation Dissipation Theorem immediately after the quark-hadron transition lead to the pro-

¹ At least to the knowledge of this author.

duction of magnetic fields with average intensity $B = 9 \mu\text{G} (0.1 \text{ pc}/L)^{3/2}$ for a region of size L .

Inflation also provides good conditions for the generation of magnetic fields. By exponentially stretching of wave modes, it allows the production of fields correlated on very large scale. Also, vacuum fluctuations of the electromagnetic field can be excited and converted into classical fluctuations if the mode grows larger than the Hubble radius.

A difficulty with fields of inflationary origin, however, is that the accelerated expansion period not only allows the generation of magnetic fields but also decreases their intensity, since a conformally invariant electromagnetic action and a conformally flat universe lead to $B \propto a^2$.

Most inflationary magnetic field generation mechanisms, thus, rely on the breaking of the conformal invariance. This can be done by coupling the electromagnetic field to gravity (e.g. $R_{\mu\nu}A^\mu A^\nu$, $RF_{\mu\nu}F^{\mu\nu}$), or to another field — for example, in a model where the inflaton potential was $V(\phi) \propto \exp(\phi)$, Ratra (1992) obtains fields $\sim 1 \text{ nG}$, by coupling the electromagnetism to the inflaton through a term proportional to $\exp(\phi)F_{\mu\nu}F^{\mu\nu}$.

An important class of theories for the creation of seed magnetic fields is that of theories based on a Biermann battery mechanism (Biermann, 1950).

This mechanism can act in diverse astrophysical systems and scales. In some cases, the produced magnetic fields could span scales large enough to be compatible with reasoning of the rest of this chapter (despite not being strictly primordial in the sense of the first paragraph of this section). This is the case for fields associated with the large scale structure formation (Peebles, 1967; Rees & Reinhardt, 1972; Wasserman, 1978).

Alternatively, magnetic fields could be generated by a Biermann battery *locally*. This could have occurred during the collapse protogalaxies (Davies & Widrow, 2000), during star formation or supernova explosions (Hanayama et al., 2005; Miranda et al., 1998). In this scenarios, the local magnetic field would be amplified and later ejected from the galaxies into the intercluster medium (possibly through the AGN jets Xu et al. 2010).

On the observational side, important constraints can be derived from matter and CMB power spectra. Yamazaki et al. (2010) find, on a comoving scale of 1 Mpc, a best fit value of $B = 0.85 \pm 1.25$ nG (which leads to an *upper-limit* of 2.98 nG at 95% CL).

The reionization of the Universe also puts upper limits of $\sim 0.7 - 3$ nG for the primordial field, depending on the assumptions on the stellar population that is responsible for reionizing the Universe (Schleicher et al., 2008).

From the observation of TeV blazars, Neronov & Vovk (2010) find a *lower-limit* of 3×10^{-16} G for the strength of intergalactic magnetic fields.

Finally, it is observed that in our galaxy, the magnetic field is coherent over kpc scales with alternating directions in the arm and inter-arm regions (e.g. Kronberg 1994; Han 2008). Such alternations are expected for magnetic fields of primordial origin (Grasso & Rubinstein, 2001).

7.2 Effects on the filtering mass

In section 6.2 it was discussed the concept of filtering mass and how it can be used to parametrize the gas accretion to a dark matter halo, allowing one to model the reionization epoch. During reionization, the intergalactic gas is heated up and therefore has its pressure increased, what leads to an increase in the Jeans mass and in the filtering mass. It is shown in this section that magnetic fields can affect the filtering mass in an analogous way.

7.2.1 Homogeneous magnetic fields

I start by examining magnetic fields which are uniform in domains larger than a typical dark matter halo and therefore can be taken as effectively “homogeneous” in the reasoning that follows.

In addition, the calculation aims modelling the accretion of gas by the whole halo, therefore it will not be taken into account the amplification of the fields by the turbulent environment which can be found in the small volume in the vicinity of the galaxy centre of the halo.

The first step is to rewrite the expression for the Jeans length in a way that takes into

account the presence of magnetic fields. Even before reionization epoch, the Universe had a degree of reionization sufficiently high ($x_e \sim 10^{-4}$ after the recombination) to couple magnetic fields to the medium. Under these circumstances the maximum velocity a perturbation can travel through the plasma is that of a (fast) magneto-acoustic wave

$$c_f = \sqrt{c_s^2 + c_A^2}, \quad (7.1)$$

where c_s is the sound speed and $c_A^2 = \frac{B^2}{4\pi\rho}$ is the Alfvén speed.

The pressure due to the magnetic field can, therefore, be taken into account in the Jeans wavenumber by making the substitution²: $c_s \rightarrow c_f$, in equation 6.8, which results in

$$\left(\frac{k_J}{a}\right)^2 = \frac{4\pi G\rho}{c_f^2} = \frac{4\pi G\rho}{c_s^2 + c_A^2}. \quad (7.2)$$

Thus, the Jeans mass, is given by

$$M_J = \frac{1}{6\sqrt{\pi}} \bar{\rho}^{-\frac{1}{2}} G^{-\frac{3}{2}} \left(\frac{B^2}{4\pi\bar{\rho}} + \frac{5}{3} \frac{k_B T}{m_H \mu} \right)^{\frac{3}{2}}, \quad (7.3)$$

where $\bar{\rho}$ is the mean density and it was assumed $c_s = \sqrt{\gamma k_B T / (\mu m_H)}$, with m_H being the mass of a hydrogen atom, μ the mean molecular weight and k_B the Boltzmann constant.

This expression generalizes previous calculations of the Jeans mass which only considered its limiting cases: $B \rightarrow 0$, the usual Jeans mass, or $T \rightarrow 0$, the magnetic Jeans mass (Kim et al., 1996).

Because of the conservation of the magnetic flux, the magnetic field evolve as

$$B = B_0 \left(\frac{a_0}{a} \right)^2. \quad (7.4)$$

Knowing the Jeans mass scale, it is possible to determine the filtering mass em-

² This Ansatz can be further checked by estimating the Jeans mass using the magnetic virial theorem (see, for example, Padmanabhan 2000):

$$2\mathcal{K} + \mathcal{V} + \mathcal{M} = 0$$

which allows us to re-obtain equation 7.3 (except for an order of unit numerical factor), using $\mathcal{K} = \frac{3}{2} \frac{M}{\mu m_H} kT$, $\mathcal{V} = -\frac{3}{5} \frac{GM}{R}$, $\mathcal{M} = \frac{M}{\rho} \frac{B^2}{8\pi}$, for the kinetic, gravitational and magnetic energies, respectively.

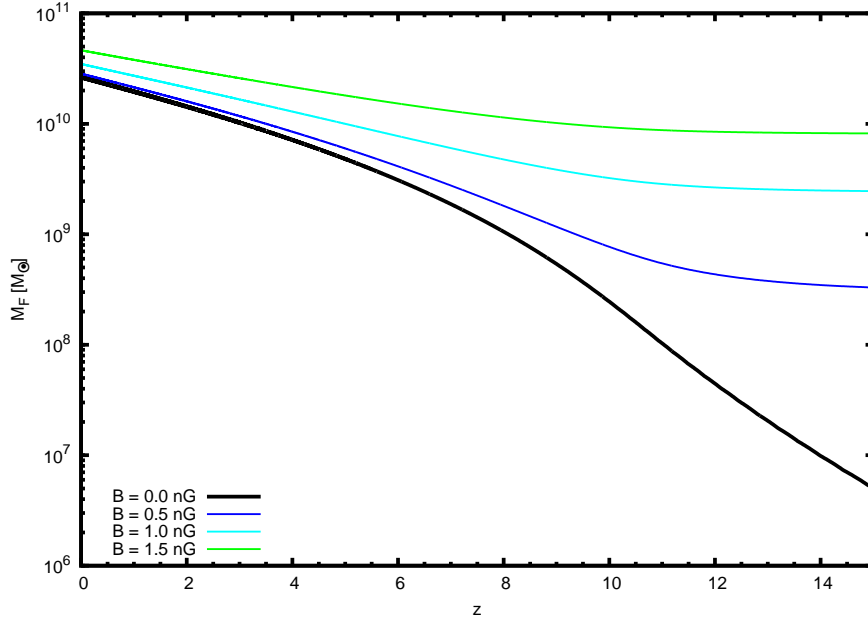


Figure 7.1: Variation of the filtering mass with redshift in the presence of homogeneous magnetic fields of different strengths.

ploying equation 6.10. In figure 7.1 the impact of a small homogeneous magnetic field is shown. A significant change in the filtering mass can be seen, particularly at high z , i.e. before or during the reionization of the Universe.

7.2.2 Random magnetic fields

Many mechanisms for the generation of magnetic fields do not produce the high coherence lengths which were assumed for the last section. To increase the generality, the case of magnetic fields structured as small randomly oriented field *cells* will be now considered.

For a random magnetic field, the magnetic pressure in a region of comoving size L greater than the comoving size of a magnetic cell, L_0 , is given by (Hindmarsh & Everett, 1998)

$$p = \frac{B_{rms}^2}{8\pi} \quad (7.5)$$

with the following expression for the rms average of the field (Grasso & Rubinstein,

2001; de Souza & Opher, 2008)

$$B_{rms}(a) = \sqrt{\langle B^2 \rangle} = B_0 \left(\frac{L_0}{L} \right)^p \left(\frac{a_0}{a} \right)^2, \quad L > L_0, \quad (7.6)$$

where B_0 is the field intensity in an individual cell.

For $L < L_0$, the average is being made inside a single cell, hence

$$B_{rms}(a) = B_0 \left(\frac{a_0}{a} \right)^2, \quad L < L_0. \quad (7.7)$$

The parameter p depends on the geometry of the field considered. A common outcome of primordial magnetic field models is the case where each cell contains a *dipole field*, which leads to $p = 3/2$ (Hindmarsh & Everett, 1998; de Souza & Opher, 2008, 2010).

If, on the other hand, the magnetic fields appear in the form of large ring-like fields (as found by Ahonen & Enqvist 1998; Enqvist & Olesen 1993) in cells with randomly oriented planes of inclination, one finds $p = 1$ (since this is equivalent to a random walk on a 2D surface of a sphere).

The random magnetic fields can be taken into account in the treatment of the previous section by replacing c_A in equation 7.2 by the effective value $\bar{c}_A^2 = \frac{B_{rms}^2}{4\pi\rho}$, which is consistent with equation 7.5.

The calculation of the Jeans mass now involves choosing between the single-cell and multi-cell regimes. To do so, we first tentatively calculate the (comoving) Jeans length, L_j , assuming a multi-cell regime. Thus, from equations 7.6 and 7.3,

$$L_j^6 = \left(\frac{\kappa}{G} \right)^3 \left[\frac{\kappa B_0^2}{3} \left(\frac{L_0}{L_j} \right)^{2p} + \frac{5}{3} \frac{k_B T(z)}{\mu m_H} (1+z)^{-1} \right]^3. \quad (7.8)$$

where $\kappa \equiv \frac{2G}{\Omega_{m0} H_0^2}$, with

$$\bar{\rho} = \Omega_{m0} \frac{3H_0^2}{8\pi G} (1+z)^3 = \frac{3}{4\pi} \frac{(1+z)^3}{\kappa}, \quad (7.9)$$

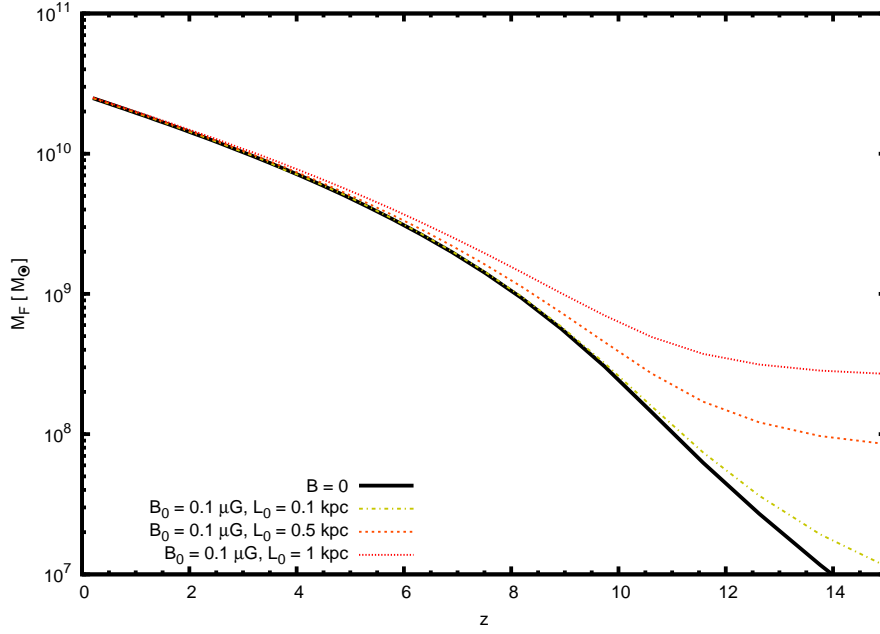


Figure 7.2: Effect of a *dipole-like* ($p = 3/2$) random magnetic field on the filtering mass.

and

$$L_j^3 = \frac{M_J}{\frac{4}{3}\pi\rho}(1+z)^3 = \kappa M_J. \quad (7.10)$$

If $L_j > L_0$, then the assumption of a multi-cell regime was correct. The solution of equation 7.8 is, thus, the comoving Jeans length and the Jeans mass is given by equation 7.10.

Alternatively, if $L_j < L_0$, then the average is done inside a single cell, using equation 7.7, and the Jeans mass is given by

$$M_J^2 = \frac{\kappa}{G^3} \left[\frac{\kappa}{3} B_0^2 + \frac{5}{3} \frac{k_B T(z)}{\mu m_H (1+z)} \right]^3. \quad (7.11)$$

Having obtained the Jeans mass, it is possible to substitute it in equation 6.10 and calculate how a random primordial magnetic field affects the filtering mass.

The results are shown – for a range of values of L_0 and B_0 – in figures 7.2 and 7.3, in the case of dipole-like magnetic fields, and in figures 7.4 and 7.5, it in the case of ring-like magnetic fields.

The scale dependence, introduced by the calculation of the average magnetic field, leads to very small effects of random primordial magnetic fields on the fil-

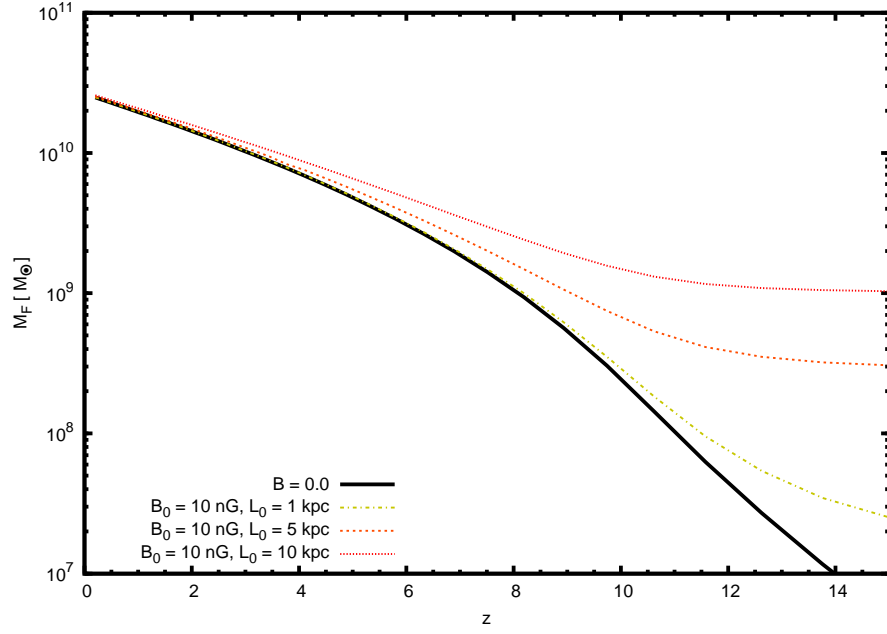


Figure 7.3: Effect of a *dipole-like* ($p = 3/2$) random magnetic field on the filtering mass.

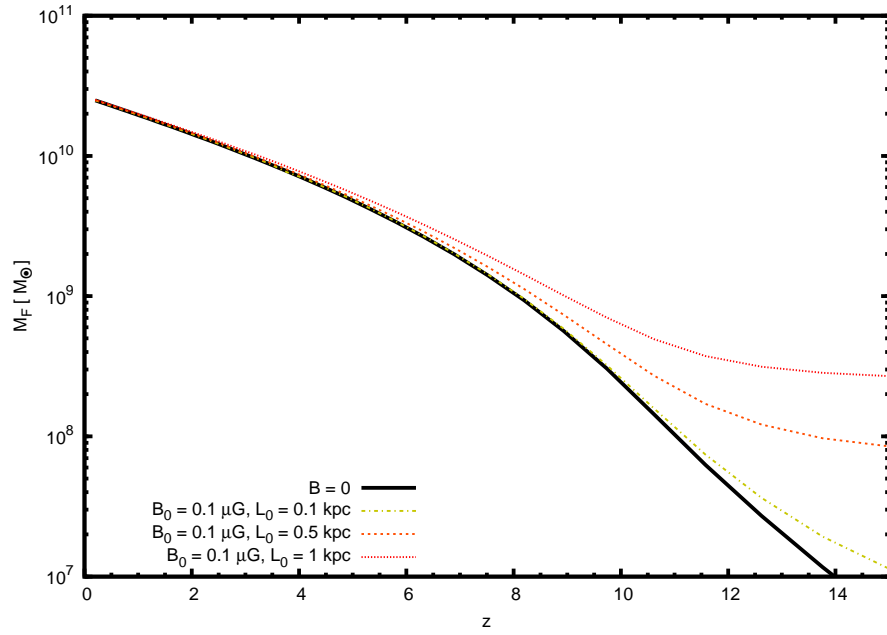


Figure 7.4: Effect of a *ring-like* ($p = 1$) random magnetic field on the filtering mass.

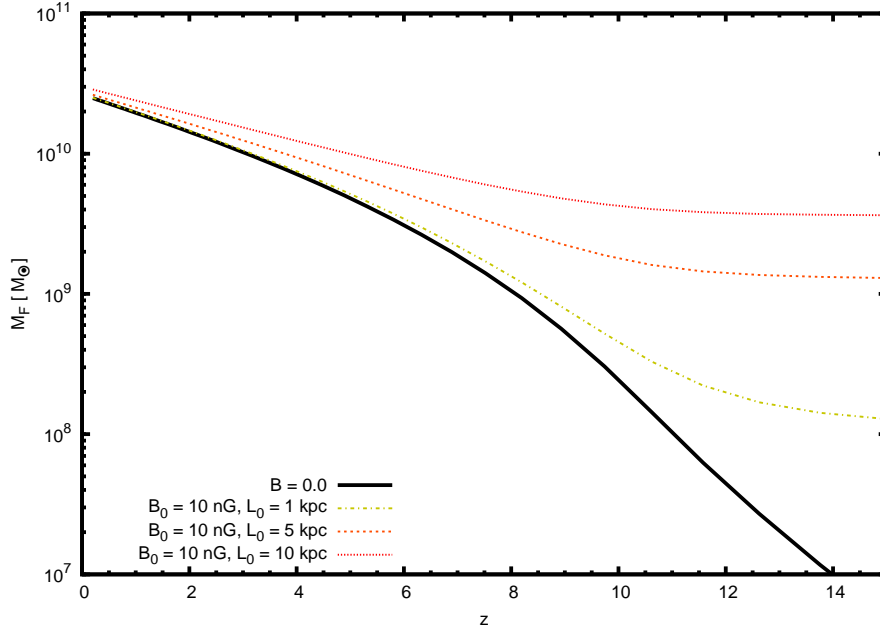


Figure 7.5: Effect of a *ring-like* ($p = 1$) random magnetic field on the filtering mass.

tering mass at low redshifts. However, effects become appreciable when approaching reionization (reminding that in the temperature parametrization used, reionization occurs between $z = 10$ and $z = 11$).

One important feature of these results is that this difference in behaviour with redshift for the different field geometries. This suggests the interesting possibility of testing the field geometry through observations of the clustering of baryonic structure at different redshifts.

The importance of such a test can be further appreciated if one takes into account that, presently, the most stringent constraints for a primordial magnetic field come from the CMB, which sets an upper limit for large scale fields of ~ 3 nG. The analysis presented here allows this upper limit to be translated into an upper limit for the filtering mass $M_F \lesssim 10^{11} M_\odot$ which varies very slowly with redshift. The CMB leaves, therefore, a degeneracy between a wide range of possible models of primordial magnetic fields. This degeneracy could in principle be broken, however, by looking at observable imprints on structure formation left by those fields.

Nevertheless, there is one difficulty: the values of L_0 and B_0 shown in the figures are actually higher than the predictions of many models of random primordial magnetic

fields that can be found in the literature. To quote some examples:

- the model of de Souza & Opher (2008) based on plasma fluctuations leads to a dipole-like field with a comoving $B_0 \approx 0.1 \mu\text{G}$ and $L_0 \approx 1 \text{ pc}$;
- Hogan (1983), with a model which generates dipole-like fields the quark-hadron phase transition, finds $B_0 \approx 2 \times 10^{-17} \text{ G}$ and $L_0 \approx 1 \text{ AU}$;
- Cheng & Olinto (1994) obtains $B_0 \approx 10^{-16} \text{ G}$ and $L_0 \approx 1 \text{ pc}$ for dipole fields generated during the electroweak phase transition;
- Baym et al. (1996) finds ring-like fields with $B_0 \sim 10^{-7}$ to 10^{-9} G and $L_0 \sim 10 \text{ AU}$;

7.3 *Impact of a primordial magnetic field on the formation of satellite galaxies*

The changes in the filtering mass discussed in the last section provide evidence that the impact of magnetic fields should be important in galaxy formation. Since the increase in the filtering mass is stronger at high redshifts, which is precisely the epoch of formation of the smallest galaxies, one would expect that a strong enough magnetic field could lead to a suppression of the formation of small galaxies.

To test this hypothesis and to access the extension of the changes in the properties of the galaxies that can be caused by the introduction of a magnetic field, I modified and ran the GALACTICUS semi-analytic model of galaxy formation (see appendix 3.2 for details).

Since the effect of a homogeneous magnetic field is more intense than the case of random magnetic fields, particularly in low or intermediate redshifts, only they were included in the analysis.

As in the case of the effects studied in previous chapters, the results that are presented below were obtained doing 2 runs for each choice of magnetic field intensity: a low resolution run with big mass range, to study the impact of the effect on the overall galaxy population; and a high resolution run of haloes in the mass range $[5 \times 10^{11} M_\odot, 5 \times 10^{12} M_\odot]$.

In figure 7.6 it is shown the b_J luminosity function under the effect of primordial magnetic fields of intensities 0.5 nG and 1 nG, obtained from the low resolution run. One finds that the overall impact of the primordial magnetic fields is very reduced, merely altering the shape of the noise in the case faint end. The same kind result is obtained for the stellar mass function, presented in figure 7.7.

In figure 7.8 it is plotted the HI mass function³. Again, despite changes in the superimposed noise pattern, the models with and without magnetic fields are essentially indistinguishable.

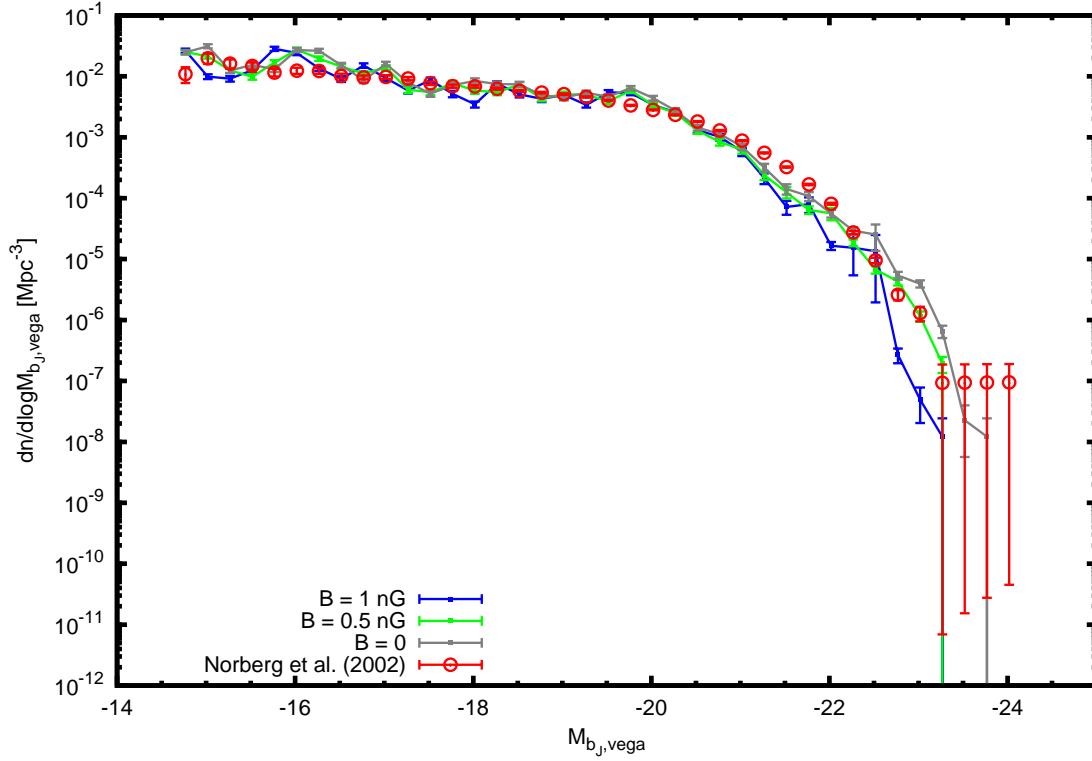


Figure 7.6: The b_J luminosity function for different values of homogeneous primordial magnetic field.

Thus, the presence or absence of magnetic fields smaller or equal 1 nG do not interfere in the overall galaxy population properties. The next step is to search for effects on the satellite population. In order to select systems sufficient similar to the Milky Way (MW), we discarded any merger tree whose central galaxy had $M_V > -18.1$ or $M_V < -23.1$ (galaxies whose luminosity is greater or smaller than the Milky Way by a factor ~ 10). We also required that the selected merger trees had at least one bright

³ To obtain the HI mass function, the cold gas mass function was calculated from the output file and multiplied by a factor 0.54 following Power et al. (2010).

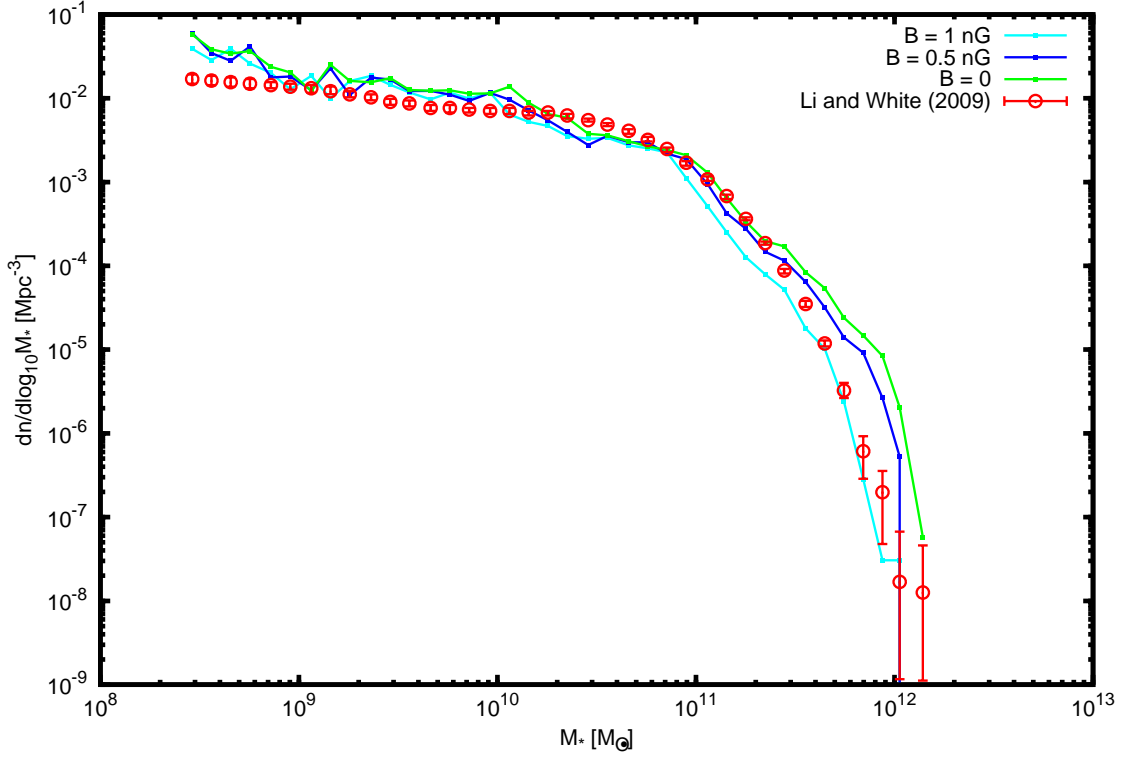


Figure 7.7: The stellar mass function for different values of homogeneous primordial magnetic field.

($M_V < -12$) satellite.

After selecting for MW-like haloes in the high resolution run, it was obtained the V-band satellite luminosity function which is shown in figure 7.9.

Interestingly, the presence of a magnetic field of intensity as small as 0.5 nG leads to a luminosity function already consistent with the observations.

In figure 7.10 the metallicity-luminosity relation under the effect of magnetic fields is shown. One can notice that, for $M_V > -10$ there is a change in the slope of the predicted relation, leading an increase in the stellar metallicity of faint galaxies.

The explanation for this at slightly counter-intuitive behaviour is the same as in the case of reionization – as it was exposed in the end of section 6.2. Because of the magnetic pressure, subhaloes of a given mass form less stars and are therefore less luminous.

Thus, if one chooses galaxies with a fixed magnitude, one finds that the subhaloes which host these galaxies, in the model with magnetic pressure, are more massive than in the case of the model without magnetic fields. Since more massive haloes can

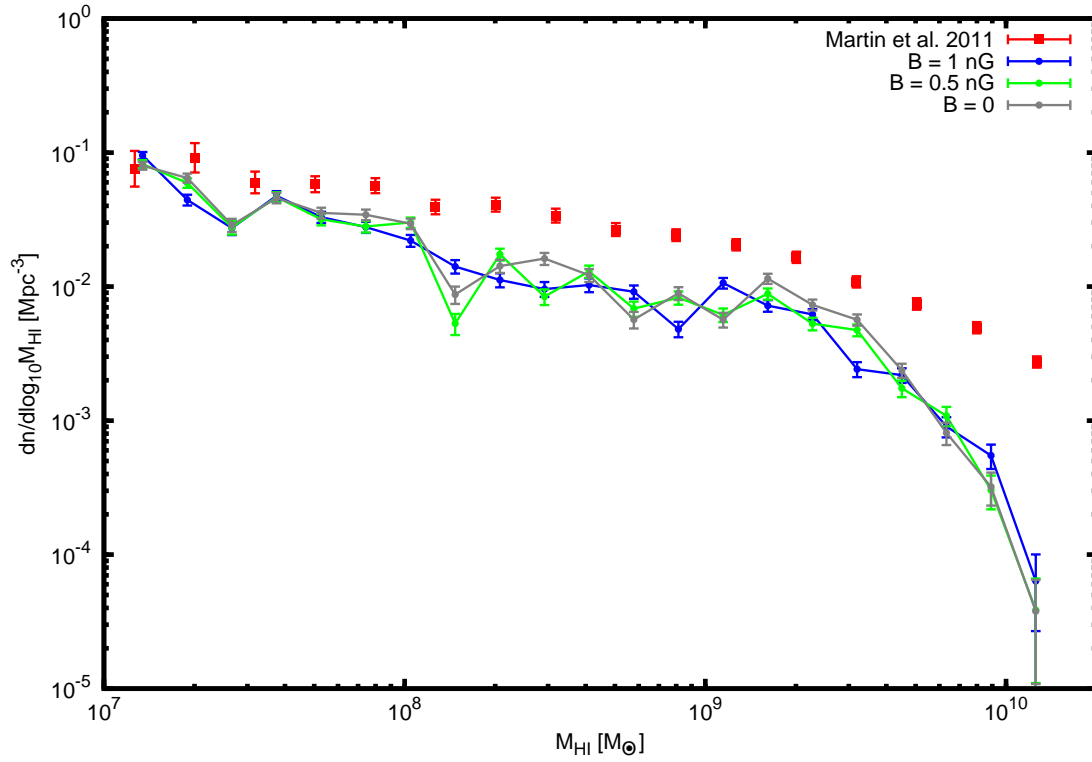


Figure 7.8: The HI mass function for different values of homogeneous primordial magnetic field.

retain metals more efficiently, this results in the observed increase in the luminosity-metallicity relation.

To confirm this picture, in figure 7.11 the mass-luminosity relation is plotted (as it was made in the end of chapter 6). The magnetic pressure leads to an important reduction in the luminosity of small mass subhaloes.

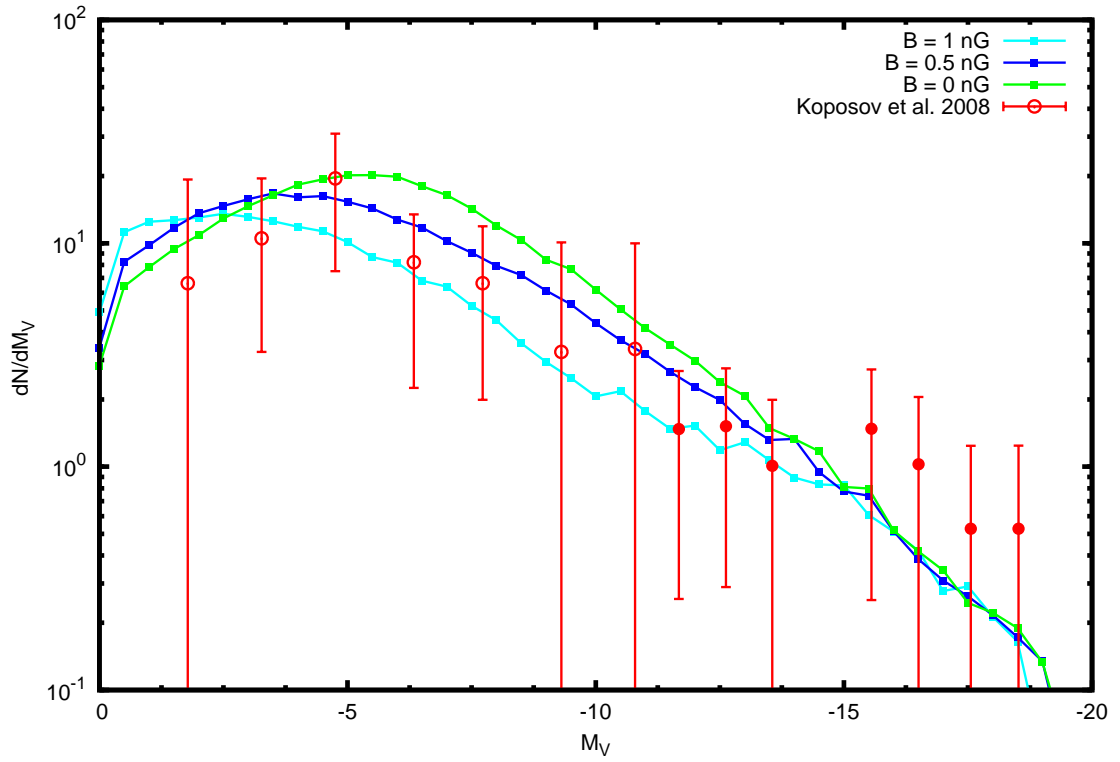


Figure 7.9: The V luminosity function function of satellite galaxies for different values of homogeneous primordial magnetic field.

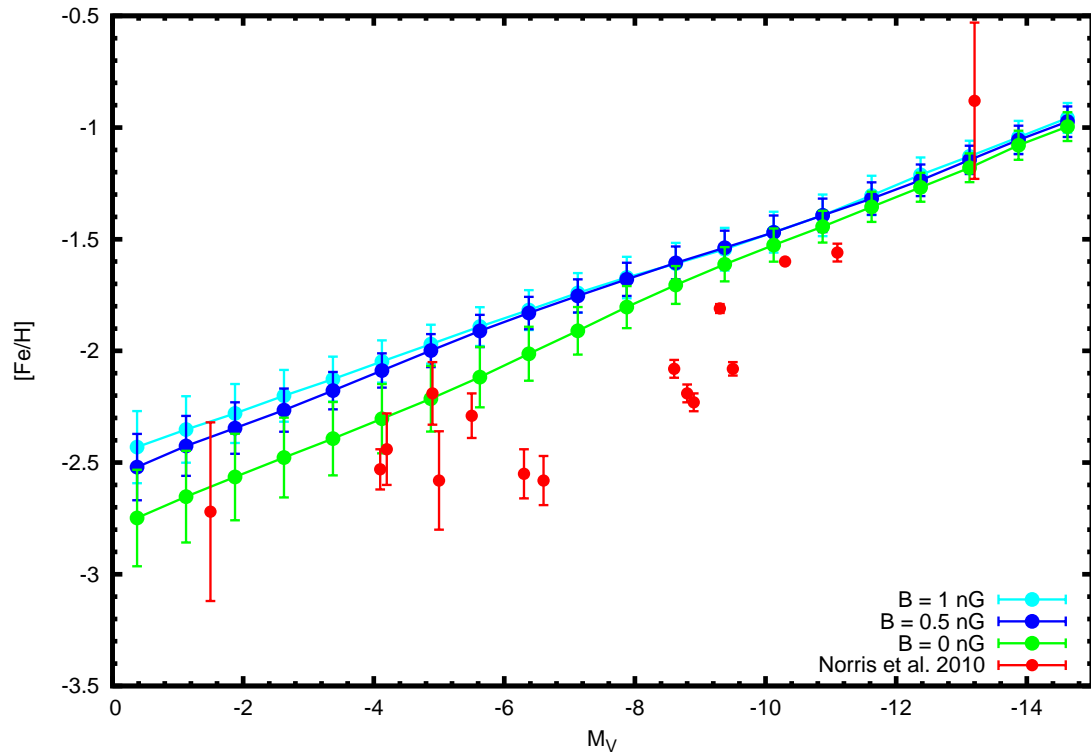


Figure 7.10: The luminosity-metallicity relation for satellite galaxies of a Milky-Way-like central galaxy, under different values of homogeneous primordial magnetic field.

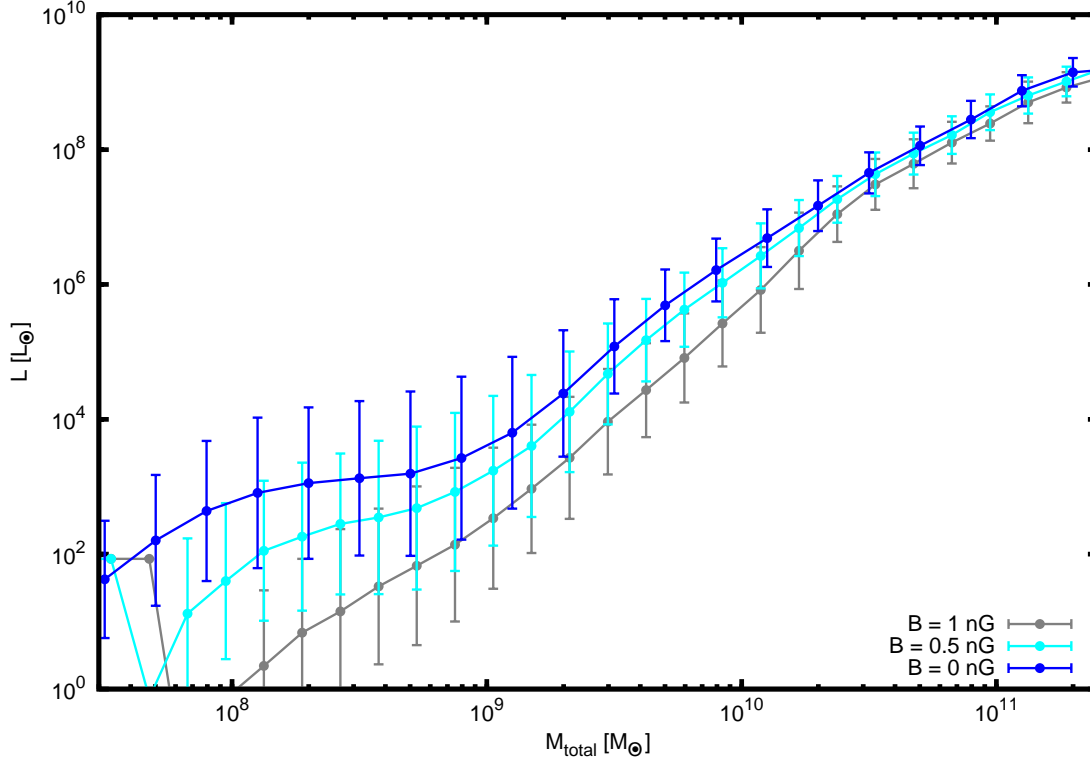


Figure 7.11: Effects of magnetic fields on the inner mass of the satellite galaxies.

7.4 Summary and discussion

In this chapter I presented some original results regarding the influence of magnetic fields on the formation of satellite galaxies.

In the beginning of the chapter, the knowledge on primordial magnetic fields and the observational constraints on the was briefly reviewed.

It was, then, discussed how a homogeneous magnetic field would alter the filtering mass. This quantity – first introduced in chapter 6 in the context of the modelling of effects of reionization – parametrizes the amount of hot gas that can be accreted by a dark matter halo.

A magnetic field will lead to an extra amount of pressure, thus an increase in the Jeans mass and in the filtering mass. The effect is more pronounced at high redshifts, where the magnetic contribution to the Jeans mass dominates over the regular thermal contribution.

The discussion was then generalized, considering a random primordial magnetic field. The field was assumed to be inside randomly oriented cells that shared a characteristic size. For realistic field and coherence length values, this leads a smaller effect than the case of homogeneous fields.

Finally, the modified filtering mass was introduced in GALACTICUS semi-analytic galaxy formation model. The presence of magnetic fields did not perturb well established predicted of semi-analytic models, as the overall luminosity function, but allowed, at the same time, a good match to the observation for the satellite luminosity function.

Thus, primordial magnetic fields represent another astrophysical mechanism that could explain the scarcity of dwarf galaxies orbiting the Milky Way.

The consequences of the primordial magnetic fields to luminosity-metallicity relation were also studied. Similarly to the case of thermal pressure associated with reionization, magnetic pressure leads to an increase, relative to the $B = 0$ case, in the metallicity associated with galaxies with a given luminosity.

Chapter 8

Conclusions

In this thesis, many aspects of the long standing conundrum known in the literature as the “missing satellites problem” were studied.

The problem was formulated in chapter 4, as the discrepancy between the slope of observed mass function of the satellite galaxy population of the Milky Way and the mass function of the subhaloes predicted by dark matter N-body simulations.

It was highlighted there that a direct comparison between these two observables may not be meaningful since known astrophysical processes affect the relationship between mass and light. It was then advocated that one should, instead, try to model the few observed relations which were discussed in chapter 2, namely: the luminosity function of satellites, the metallicity-luminosity relation and the distribution of inner masses.

The challenge of theoretically predicting these relations in a consistent galaxy formation model was named “satellite problem”. It was then highlighted that this is different from the “substructure problem”, which I define as the empirical evidence of the existence (or absence) of dark matter substructures in the Milky Way halo.

In chapter 5, I discussed how warm dark matter and modified inflationary models may lead to distortions in the initial power spectrum of density perturbations.

To exemplify how this effect can be achieved, a new inflaton potential was proposed, where the common quadratic (chaotic) inflaton potential had an oscillating pattern superimposed for small field values. This toy model was simple enough to allow a treatment based on the “slow-roll” approximation. With deviations of 5% from the usual quadratic potential, a reduction of $\approx 50\%$ in the number of small halos was

obtained.

Given the uncertainties associated with the details of the inflationary paradigm, scale dependent features in the power spectrum as the ones discussed cannot be seen as something implausible, but as an empirical issue.

The most important probe of the small scale power spectrum is extracted from the Lyman- α forest data. These data can only probe scales $k \lesssim 0.01 \text{ Mpc}^{-1}$. Dwarf galaxies, however are associated with density perturbation of wavenumbers higher than that. Thus, their properties can be faced as a probe to those scales.

It was shown that a break in the initial power spectrum leads to a luminosity function for the satellite galaxy population consistent with present observations.

In chapter 6, I reviewed the major feedback mechanisms that can have impact on the satellite galaxies population. Both the outflows, caused by supernovae explosions, and the suppression of gas accretion, caused by the photoheating of IGM during reionization epoch, can lead to a correct luminosity function.

Both these solutions have, nevertheless, their own associated problems. In order to the supernovae feedback to be able to suppress enough the small mass galaxy formation, it is necessary to have more outflow than what would be expected from simple energetic arguments. In the case of the implementation of reionization, an increase in the reionization temperature or a change in the reionization redshift is required.

It could be argued, however, that the treatment of reionization which was presented did not take into account the effect of local ionizing sources, which can enhance the effect. This requires much more involved modelling than the way the subject was treated here. Nevertheless, even when this is taken into account (Font et al., 2011), the match between the predicted and observed luminosity function could only be achieved after making the assumption of a photon escape fraction well above that which would be expected.

In chapter 7, I presented perhaps the most significant contribution of this thesis. In it I discuss how cosmic small magnetic fields can have a non-negligible influence on galaxy formation. Acting similarly to the reionization photoheating, the presence of a magnetic field alters the filtering mass and suppresses the accretion of gas by dark

matter haloes.

We found significant changes in the filtering mass when considering primordial magnetic field strengths well within the observational constraints, both in the case of homogeneous large scale fields and in the case of random magnetic fields.

Since the filtering mass sets the halo mass scale below which the hot gas accretion is suppressed, the results obtained imply a reduction of the gas accretion by the haloes inhabited by small mass galaxies, which could lead to a smaller star formation rate in these haloes, resulting in a reduction of the number of observable satellite galaxies.

The enhancement of the filtering mass is more pronounced at higher redshifts, when the magnetic contribution to the Jeans mass becomes comparable or bigger than the thermal contribution. This makes the suppression effect more dramatic for small mass galaxies, which are formed at higher redshifts.

In order to test this hypothesis – that the suppression of gas accretion due to the pressure of a seed magnetic field results in the inhibition of the formation of small mass galaxies – the modified filtering mass was introduced in a complete galaxy formation model.

The magnetic fields did not alter significantly the properties of the overall galaxy population allowing the prediction of the correct form for the b_J luminosity function as well as other observables.

On the other hand, the luminosity function for the satellites of a galaxy similar to the Milky Way was affected and the presence of a magnetic field as small as 5 nG is sufficient to predict a faint end luminosity function in agreement with the observations from the SDSS.

This shows that the impact of a primordial magnetic field on the satellite population is not only non-negligible but a viable route to the resolution of the missing satellites problem.

From epoch of the beginning of my doctoral studies until today, the status of the missing satellites problem changed from a challenging unsolved problem and “crises” in standard cosmological scenario, into a problem with many plausible solutions.

In this thesis, I demonstrated that several physical mechanisms can suppress significantly the satellite population and therefore solve the missing satellites problem

in terms of the most important observable associated with it: the satellite luminosity function.

Nonetheless, it is necessary to find a way to break the degeneracy between the possible answers. One interesting aspect of the analysis here presented is that the luminosity-metallicity relationship presents good sensitiveness to each possible solution.

Unfortunately, the semi-analytic model that was used does not have enough precision to make more definite predictions about this observable. Regardless the variation used, our version of GALACTICUS predicted the wrong normalization for the luminosity-metallicity relation.

Despite this difficulty, it was possible to see that each of the suggested modifications for a match in the luminosity function produces changes in the luminosity-metallicity relation (LMR) in a different way: (1) A simple suppression of power in the initial power spectrum will lead to a change in the slope of the MLR at the faint end; (2) An increase in the exponent of the SN feedback law, α , lead to a change in the overall normalization of the LMR; (3) An earlier reionization epoch will imply in a change of both, slope and normalization of the LMR; and finally, (4) Magnetic fields affect exclusively the faint end.

Perspectives

There are many possibilities of refinement and further development of the current work. In particular, I plan to address the following:

Amplification of galactic magnetic fields In chapter 7, a conservative approach was taken for the introduction of magnetic fields, considering only unamplified primordial fields. To go further, it is necessary to also model magnetic fields in the galactic environment, which are affected by both small-scale (or “turbulent”) and large scale (or galactic) dynamo mechanisms (Arshakian et al., 2009, 2011) and which are strongly influenced by galaxy interactions (Kotarba et al., 2011; Drzazga et al., 2011). The properties of those galactic magnetic fields are likely to be correlated with observable properties of the galaxies themselves, allowing extra tests for the hierarchical scenario.

Ejection of magnetic fields to the intergalactic medium Active galactic nuclei can inject magnetic fields in the intracluster medium which can be sustained and amplified by the turbulence in the medium associated with successive mergers (Xu et al., 2010; Sutter et al., 2011). In massive environments, thus, the magnetic fields generated by AGNs may overcome the primordial cosmic fields and boost the effect of gas accretion suppression (discussed in chapter 7) in those systems.

The chemical enrichment of the dwarf satellite population As was discussed, the amount of metals in the galaxies can be used to access the relative importance of various physical processes and choose between proposed solutions to the missing satellite problem. However, the model predicted an abundance of metals much higher than observed. Thus, the modelling of the chemical enrichment and of the supernovae feedback must be refined.

Environmental effects on the satellite galaxies population In the semi-analytic model employed in this thesis, the modelling of environmental effects on the satellite galaxies was restricted to the ‘starvation’ (described in section 3.2.2), which corresponds to the complete removal of the hot gas halo of a galaxy through ram pressure. While this approach is an adequate approximation for the satellite population (McCarthy et al., 2008), a more involved calculation taking into account the possibility of partial hot halo removal is desirable given the importance of hot gas accretion in the evolution of these objects. Other important environmental effects which were not taken into account are *tidal stripping* and *tidal heating* of the subhaloes.

Bibliography

- Abel T., Wise J. H., Bryan G. L., The H II Region of a Primordial Star, *ApJ*, 2007, vol. 659, p. L87 B.2
- Adams J. A., Ross G. G., Sarkar S., Multiple inflation, *Nuclear Physics B*, 1997, vol. 503, p. 405 5.1
- Ahonen J., Enqvist K., Magnetic field generation in first order phase transition bubble collisions, *Phys. Rev. D*, 1998, vol. 57, p. 664 7.1, 7.2.2
- Alvarez M. A., Bromm V., Shapiro P. R., The H II Region of the First Star, *ApJ*, 2006, vol. 639, p. 621 B.2
- Arshakian T. G., Beck R., Krause M., Sokoloff D., Evolution of magnetic fields in galaxies and future observational tests with the Square Kilometre Array, *A&A*, 2009, vol. 494, p. 21 8
- Arshakian T. G., Stepanov R., Beck R., Krause M., Sokoloff D., Modeling the total and polarized emission in evolving galaxies: "Spotty" magnetic structures, *Astronomische Nachrichten*, 2011, vol. 332, p. 524 8
- Bardeen J. M., Bond J. R., Kaiser N., Szalay A. S., The statistics of peaks of Gaussian random fields, *ApJ*, 1986, vol. 304, p. 15 5.2
- Barnes J., Hut P., A hierarchical $O(N \log N)$ force-calculation algorithm, *Nature*, 1986, vol. 324, p. 446 3.1
- Baugh C. M., A primer on hierarchical galaxy formation: the semi-analytical approach, *Reports on Progress in Physics*, 2006, vol. 69, p. 3101 3.2

- Baugh C. M., Lacey C. G., Frenk C. S., Granato G. L., Silva L., Bressan A., Benson A. J., Cole S., Can the faint submillimetre galaxies be explained in the Λ cold dark matter model?, MNRAS, 2005, vol. 356, p. 1191 6.1
- Baym G., Bödeker D., McLerran L., Magnetic fields produced by phase transition bubbles in the electroweak phase transition, Phys. Rev. D, 1996, vol. 53, p. 662 7.2.2
- Beck R., Galactic and Extragalactic Magnetic Fields. In American Institute of Physics Conference Series , vol. 1085 of American Institute of Physics Conference Series, 2008, p. 83 7
- Benson A. J., Orbital parameters of infalling dark matter substructures, MNRAS, 2005, vol. 358, p. 551 3.2.5
- Benson A. J., Galacticus: A Semi-Analytic Model of Galaxy Formation, ArXiv e-prints, 2010a 3.2
- Benson A. J., Galaxy formation theory, Phys. Rep., 2010b, vol. 495, p. 33 3.2, 6.1
- Benson A. J., Borgani S., De Lucia G., Boylan-Kolchin M., Monaco P., Convergence of Galaxy Properties with Merger Tree Temporal Resolution, ArXiv:1107.4098, 2011 3.2.1
- Benson A. J., Bower R., Galaxy formation spanning cosmic history, MNRAS, 2010, vol. 405, p. 1573 6.1
- Benson A. J., Lacey C. G., Baugh C. M., Cole S., Frenk C. S., The effects of photoionization on galaxy formation - I. Model and results at $z=0$, MNRAS, 2002, vol. 333, p. 156 6.2, 6.2
- Benson, A. J., 2011 private email communication A.2
- Bertschinger E., Simulations of Structure Formation in the Universe, ARA&A, 1998, vol. 36, p. 599 3.1
- Biermann L., Über den Ursprung der Magnetfelder auf Sternen und im interstellaren Raum (miteinem Anhang von A. Schlüter), Zeitschrift Naturforschung Teil A, 1950, vol. 5 7.1

- Binney J., Tremaine S., *Galactic Dynamics: Second Edition*. Princeton University Press, 2008 B.3.1
- Blitz L., Rosolowsky E., The Role of Pressure in GMC Formation II: The H_2 -Pressure Relation, *ApJ*, 2006, vol. 650, p. 933 3.2.4, 3.2.4
- Bower R. G., Benson A. J., Malbon R., Helly J. C., Frenk C. S., Baugh C. M., Cole S., Lacey C. G., Breaking the hierarchy of galaxy formation, *MNRAS*, 2006, vol. 370, p. 645 6.1
- Boylan-Kolchin M., Springel V., White S. D. M., Jenkins A., There's no place like home? Statistics of Milky Way-mass dark matter haloes, *MNRAS*, 2010, vol. 406, p. 896 2
- Brandenberger R. H., Martin J., The Robustness of Inflation to Changes in Super-Planck-Scale Physics, *Modern Physics Letters A*, 2001, vol. 16, p. 999 5.1
- Bullock J. S., Notes on the Missing Satellites Problem, *ArXiv e-prints*, 2010 4
- Bullock J. S., Stewart K. R., Kaplinghat M., Tollerud E. J., Wolf J., Stealth Galaxies in the Halo of the Milky Way, *ApJ*, 2010, vol. 717, p. 1043 1
- Burkert A., The Structure of Dark Matter Halos in Dwarf Galaxies, *ApJ*, 1995, vol. 447, p. L25 B.1, B.3.2
- Carilli C. L., Taylor G. B., Cluster Magnetic Fields, *ARA&A*, 2002, vol. 40, p. 319 7
- Cheng B., Olinto A. V., Primordial magnetic fields generated in the quark-hadron transition, *Phys. Rev. D*, 1994, vol. 50, p. 2421 7.1, 7.2.2
- Coccatto L., Swaters R. A., Rubin V. C., D'Odorico S., McGaugh S. S., VIMOS-VLT integral field kinematics of the giant low surface brightness galaxy ESO 323-G064, *A&A*, 2008, vol. 490, p. 589 B.1
- Cole S., Lacey C. G., Baugh C. M., Frenk C. S., Hierarchical galaxy formation, *MNRAS*, 2000, vol. 319, p. 168 3.2.1
- Cole S., Percival W. J., Peacock J. A., Norberg P., Baugh C. M., Frenk C. S., Baldry I., Bland-Hawthorn J., Bridges T., Cannon R., Colless M., Collins C., Couch W., et al. The 2dF Galaxy Redshift Survey: power-spectrum analysis of the final data set and cosmological implications, *MNRAS*, 2005, vol. 362, p. 505 3.1.1, 5

- Cuddeford P., An analytic inversion for anisotropic spherical galaxies, *MNRAS*, 1991, vol. 253, p. 414 B.3.1
- Dalal N., Kochanek C. S., Direct Detection of Cold Dark Matter Substructure, *ApJ*, 2002, vol. 572, p. 25 4
- Davies G., Widrow L. M., A Possible Mechanism for Generating Galactic Magnetic Fields, *The Astrophysical Journal*, 2000, vol. 540, p. 755 7.1
- de Blok W. J. G., Halo Mass Profiles and Low Surface Brightness Galaxy Rotation Curves, *ApJ*, 2005, vol. 634, p. 227 B.1
- de Blok W. J. G., The Core-Cusp Problem, *Advances in Astronomy*, 2010, vol. 2010, p. 5 B.1
- de Blok W. J. G., Bosma A., McGaugh S., Simulating observations of dark matter dominated galaxies: towards the optimal halo profile, *MNRAS*, 2003, vol. 340, p. 657 B.1
- de Souza R. S., Opher R., Origin of primordial magnetic fields, *Phys. Rev. D*, 2008, vol. 77, p. 043529 7.1, 7.2.2, 7.2.2, 7.2.2
- de Souza R. S., Opher R., Origin of magnetic fields in galaxies, *Phys. Rev. D*, 2010, vol. 81, p. 067301 7.1, 7.2.2, B.1
- de Souza R. S., Rodrigues L. F. S., Ishida E. E. O., Opher R., The effect of a single supernova explosion on the cuspy density profile of a small-mass dark matter halo, *MNRAS*, 2011, vol. 415, p. 2969 B
- de Souza R. S., Rodrigues L. F. S., Opher R., Random primordial magnetic fields and the gas content of dark matter haloes, *MNRAS*, 2011, vol. 410, p. 2149 7, B.2.2
- Dehnen W., Phase-space mixing and the merging of cusps, *MNRAS*, 2005, vol. 360, p. 892 B.1
- Dekel A., Silk J., The origin of dwarf galaxies, cold dark matter, and biased galaxy formation, *ApJ*, 1986, vol. 303, p. 39 B.1

- Diemand J., Kuhlen M., Madau P., Dark Matter Substructure and Gamma-Ray Annihilation in the Milky Way Halo, *ApJ*, 2007, vol. 657, p. 262 2.3, 3.1.2, 4
- Diemand J., Kuhlen M., Madau P., Zemp M., Moore B., Potter D., Stadel J., Clumps and streams in the local dark matter distribution, *Nature*, 2008, vol. 454, p. 735 3.1.2
- Diemand J., Moore B., Stadel J., Earth-mass dark-matter haloes as the first structures in the early Universe, *Nature*, 2005, vol. 433, p. 389 3.1.2
- Donato F., Gentile G., Salucci P., Frigerio Martins C., Wilkinson M. I., Gilmore G., Grebel E. K., Koch A., Wyse R., A constant dark matter halo surface density in galaxies, *MNRAS*, 2009, vol. 397, p. 1169 B.3.2
- Drzazga R. T., Chyży K. T., Jurusik W., Wiórkiewicz K., Magnetic field evolution in interacting galaxies, *A&A*, 2011, vol. 533, p. A22+ 8
- Efstathiou G., Davis M., White S. D. M., Frenk C. S., Numerical techniques for large cosmological N-body simulations, *ApJS*, 1985, vol. 57, p. 241 3.1
- Eisenstein D. J., Hu W., Baryonic Features in the Matter Transfer Function, *ApJ*, 1998, vol. 496, p. 605 5.1.1
- Enqvist K., Olesen P., On primordial magnetic fields of electroweak origin, *Physics Letters B*, 1993, vol. 319, p. 178 7.2.2
- Ferland G. J., Korista K. T., Verner D. A., Ferguson J. W., Kingdon J. B., Verner E. M., CLOUDY 90: Numerical Simulation of Plasmas and Their Spectra, *PASP*, 1998, vol. 110, p. 761 3.2.3
- Font A. S., Benson A. J., Bower R. G., Frenk C. S., Cooper A., De Lucia G., Helly J. C., Helmi A., Li Y.-S., McCarthy I. G., Navarro J. F., Springel V., Starkenburg E., Wang J., White S. D. M., The population of Milky Way satellites in the Λ cold dark matter cosmology, *MNRAS*, 2011, vol. 417, p. 1260 3, 8
- Fryxell B., Olson K., Ricker P., Timmes F. X., Zingale M., Lamb D. Q., MacNeice P., Rosner R., Truran J. W., Tufo H., FLASH: An Adaptive Mesh Hydrodynamics Code for Modeling Astrophysical Thermonuclear Flashes, *ApJS*, 2000, vol. 131, p. 273 3

- Gnedin N. Y., Effect of Reionization on Structure Formation in the Universe, *ApJ*, 2000, vol. 542, p. 535 6.2, B.2.2, B.2.2
- Gnedin N. Y., Hui L., Probing the Universe with the Ly α forest - I. Hydrodynamics of the low-density intergalactic medium, *MNRAS*, 1998, vol. 296, p. 44 6.2
- Gnedin O. Y., Zhao H., Maximum feedback and dark matter profiles of dwarf galaxies, *MNRAS*, 2002, vol. 333, p. 299 B.1, B.4
- Governato F., Brook C., Mayer L., Brooks A., Rhee G., Wadsley J., Jonsson P., Willman B., Stinson G., Quinn T., Madau P., Bulgeless dwarf galaxies and dark matter cores from supernova-driven outflows, *Nature*, 2010, vol. 463, p. 203 B.1
- Govoni F., Feretti L., Magnetic Fields in Clusters of Galaxies, *International Journal of Modern Physics D*, 2004, vol. 13, p. 1549 7
- Grasso D., Rubinstein H. R., Magnetic fields in the early Universe, *Phys. Rep.*, 2001, vol. 348, p. 163 7, 7.1, 7.2.2
- Grebel E. K., The Star Formation History of the Local Group. In *Star Formation from the Small to the Large Scale*, vol. 445 of *ESA Special Publication*, 2000, p. 87 2
- Han J. L., New knowledge of the Galactic magnetic fields, *Nuclear Physics B Proceedings Supplements*, 2008, vol. 175, p. 62 7.1
- Hanayama H., Takahashi K., Kotake K., Oguri M., Ichiki K., Ohno H., Biermann Mechanism in Primordial Supernova Remnant and Seed Magnetic Fields, *ApJ*, 2005, vol. 633, p. 941 7.1
- Harris W. E., A Catalog of Parameters for Globular Clusters in the Milky Way, *AJ*, 1996, vol. 112, p. 1487 2.2
- Hensler G., Theis C., Gallagher III. J. S., Evolution of dwarf-elliptical galaxies, *A&A*, 2004, vol. 426, p. 25 B.1
- Hindmarsh M., Everett A., Magnetic fields from phase transitions, *Phys. Rev. D*, 1998, vol. 58, p. 103505 7.2.2, 7.2.2

- Hinshaw G., Weiland J. L., Hill R. S., Odegard N., Larson D., Bennett C. L., Dunkley J., Gold B., Greason M. R., Jarosik N., Komatsu E., Nolta M. R., Page L., et al., Five-Year Wilkinson Microwave Anisotropy Probe Observations: Data Processing, Sky Maps, and Basic Results, *ApJS*, 2009, vol. 180, p. 225 5.1.1
- Hoeft M., Yepes G., Gottlöber S., Springel V., Dwarf galaxies in voids: suppressing star formation with photoheating, *MNRAS*, 2006, vol. 371, p. 401 6.2
- Hogan C. J., Magnetohydrodynamic effects of a first-order cosmological phase transition, *Physical Review Letters*, 1983, vol. 51, p. 1488 7.1, 7.2.2
- Ichiki K., Nagata R., Brute force reconstruction of the primordial fluctuation spectrum from five-year Wilkinson Microwave Anisotropy Probe observations, *Phys. Rev. D*, 2009, vol. 80, p. 083002 5.1
- Ichiki K., Nagata R., Yokoyama J., Cosmic Discordance: Detection of a modulation in the primordial fluctuation spectrum, *ArXiv e-prints*, 2009 5.1
- Jarosik N., Bennett C. L., Dunkley J., Gold B., Greason M. R., et al. Seven-year Wilkinson Microwave Anisotropy Probe (WMAP) Observations: Sky Maps, Systematic Errors, and Basic Results, *ApJS*, 2011, vol. 192, p. 14 B.1
- Jiang C. Y., Jing Y. P., Faltenbacher A., Lin W. P., Li C., A Fitting Formula for the Merger Timescale of Galaxies in Hierarchical Clustering, *ApJ*, 2008, vol. 675, p. 1095 3.2.5
- Jungman G., Kamionkowski M., Griest K., Supersymmetric dark matter, *Phys. Rep.*, 1996, vol. 267, p. 195 1
- Kang X., Jing Y. P., Mo H. J., Börner G., Semianalytical Model of Galaxy Formation with High-Resolution N-Body Simulations, *ApJ*, 2005, vol. 631, p. 21 6.1
- Kazantzidis S., Zentner A. R., Kravtsov A. V., The Robustness of Dark Matter Density Profiles in Dissipationless Mergers, *ApJ*, 2006, vol. 641, p. 647 B.1
- Kennicutt Jr. R. C., The Global Schmidt Law in Star-forming Galaxies, *ApJ*, 1998, vol. 498, p. 541 3.2.4

- Kim E.-J., Olinto A. V., Rosner R., Generation of Density Perturbations by Primordial Magnetic Fields, *ApJ*, 1996, vol. 468, p. 28 7.2.1
- Kitayama T., Yoshida N., Supernova Explosions in the Early Universe: Evolution of Radiative Remnants and the Halo Destruction Efficiency, *ApJ*, 2005, vol. 630, p. 675 B.2
- Kitayama T., Yoshida N., Susa H., Umemura M., The Structure and Evolution of Early Cosmological H II Regions, *ApJ*, 2004, vol. 613, p. 631 B.2
- Klypin A., Kravtsov A. V., Valenzuela O., Prada F., Where Are the Missing Galactic Satellites?, *ApJ*, 1999, vol. 522, p. 82 4, 4
- Kochanek C. S., Dalal N., Tests for Substructure in Gravitational Lenses, *ApJ*, 2004, vol. 610, p. 69 4
- Komatsu E., Smith K. M., Dunkley J., Bennett C. L., Gold B., Hinshaw G., Jarosik N., Larson D., Nolte M. R., Page L., Spergel D. N., Halpern M., Hill R. S., et al. Seven-year Wilkinson Microwave Anisotropy Probe (WMAP) Observations: Cosmological Interpretation, *ApJS*, 2011, vol. 192, p. 18 5, 5.1, 6.2
- Koposov S., Belokurov V., Evans N. W., Hewett P. C., Irwin M. J., Gilmore G., Zucker D. B., Rix H., Fellhauer M., Bell E. F., Glushkova E. V., The Luminosity Function of the Milky Way Satellites, *ApJ*, 2008, vol. 686, p. 279 2.3, 2.3, 2.3, 2.5, 2.3
- Kotarba H., Lesch H., Dolag K., Naab T., Johansson P. H., Donnert J., Stasyszyn F. A., Galactic ménage à trois: simulating magnetic fields in colliding galaxies, *MNRAS*, 2011, vol. 415, p. 3189 8
- Kravtsov A., Dark Matter Substructure and Dwarf Galactic Satellites, *Advances in Astronomy*, 2010, vol. 2010 4.1, 4, 4
- Kravtsov A. V., Gnedin O. Y., Klypin A. A., The Tumultuous Lives of Galactic Dwarfs and the Missing Satellites Problem, *ApJ*, 2004, vol. 609, p. 482 6.2, B.2.2
- Kronberg P. P., Extragalactic magnetic fields, *Reports on Progress in Physics*, 1994, vol. 57, p. 325 7.1

- Kuzio de Naray R., McGaugh S. S., de Blok W. J. G., Mass Models for Low Surface Brightness Galaxies with High-Resolution Optical Velocity Fields, *ApJ*, 2008, vol. 676, p. 920 B.1
- Lacey C., Cole S., Merger rates in hierarchical models of galaxy formation, *MNRAS*, 1993, vol. 262, p. 627 3.2.1
- Lee J.-W., Is Dark Matter a BEC or Scalar Field?, *Journal of Korean Physical Society*, 2009, vol. 54, p. 2622 2.2
- Lee J.-W., Lim S., Minimum mass of galaxies from BEC or scalar field dark matter, *J. Cosmology Astropart. Phys.*, 2010, vol. 1, p. 7 2.2
- Liddle A. R., Lyth D. H., *Cosmological Inflation and Large-Scale Structure*, 2000 5, 1, 5.1.1
- Liu L., Gerke B. F., Wechsler R. H., Behroozi P. S., Busha M. T., How Common are the Magellanic Clouds?, *ApJ*, 2011, vol. 733, p. 62 2
- Loeb A., Barkana R., The Reionization of the Universe by the First Stars and Quasars, *ARA&A*, 2001, vol. 39, p. 19 6.2
- LSST Science Collaboration *LSST Science Book*, Version 2.0, arXiv:0912.0201, 2009 5.1
- Mac Low M., Ferrara A., Starburst-driven Mass Loss from Dwarf Galaxies: Efficiency and Metal Ejection, *ApJ*, 1999, vol. 513, p. 142 B.1
- Macciò A. V., Kang X., Fontanot F., Somerville R. S., Koposov S., Monaco P., Luminosity function and radial distribution of Milky Way satellites in a Λ CDM Universe, *MNRAS*, 2010, vol. 402, p. 1995 3, 6.2, 6.2
- Magorrian J., Tremaine S., Richstone D., Bender R., Bower G., Dressler A., Faber S. M., Gebhardt K., Green R., Grillmair C., Kormendy J., Lauer T., The Demography of Massive Dark Objects in Galaxy Centers, *AJ*, 1998, vol. 115, p. 2285 3.2.6
- Martin J., Brandenberger R., Dependence of the spectra of fluctuations in inflationary cosmology on trans-Planckian physics, *Phys. Rev. D*, 2003, vol. 68, p. 063513 5.1

- Martin N. F., de Jong J. T. A., Rix H.-W., A Comprehensive Maximum Likelihood Analysis of the Structural Properties of Faint Milky Way Satellites, *ApJ*, 2008, vol. 684, p. 1075 2.1, 2.1, 2.3, 2.4
- Mashchenko S., Couchman H. M. P., Wadsley J., The removal of cusps from galaxy centres by stellar feedback in the early Universe, *Nature*, 2006, vol. 442, p. 539 B.1
- Mashchenko S., Wadsley J., Couchman H. M. P., Stellar Feedback in Dwarf Galaxy Formation, *Science*, 2008, vol. 319, p. 174 B.1
- Massey R., Rhodes J., Ellis R., Scoville N., Leauthaud A., Finoguenov A., Capak P., Bacon D., Aussel H., Kneib J.-P., Koekemoer A., McCracken H., Mobasher B., Pires S., et al. Dark matter maps reveal cosmic scaffolding, *Nature*, 2007, vol. 445, p. 286 3.1.1
- Mateo M., Olszewski E. W., Pryor C., Welch D. L., Fischer P., The Carina dwarf spheroidal galaxy - How dark is it?, *AJ*, 1993, vol. 105, p. 510 2.2, 2.2
- Mateo M. L., Dwarf Galaxies of the Local Group, *ARA&A*, 1998, vol. 36, p. 435 2.1, 2.2
- McCarthy I. G., Frenk C. S., Font A. S., Lacey C. G., Bower R. G., Mitchell N. L., Balogh M. L., Theuns T., Ram pressure stripping the hot gaseous haloes of galaxies in groups and clusters, *MNRAS*, 2008, vol. 383, p. 593 8
- Metz M., Kroupa P., Jerjen H., The spatial distribution of the Milky Way and Andromeda satellite galaxies, *MNRAS*, 2007, vol. 374, p. 1125 2.5
- Miranda O., Opher M., Opher R., Seed magnetic Fields Generated by Primordial Supernova Explosions, *MNRAS*, 1998, vol. 301, p. 547 7.1
- Moore B., Ghigna S., Governato F., Lake G., Quinn T., Stadel J., Tozzi P., Dark Matter Substructure within Galactic Halos, *ApJ*, 1999, vol. 524, p. L19 4, B.1
- Mori M., Ferrara A., Madau P., Early Metal Enrichment by Pregalactic Outflows. II. Three-dimensional Simulations of Blow-Away, *ApJ*, 2002, vol. 571, p. 40 B.1
- Mori M., Umemura M., Ferrara A., The Nature of Ly α Blobs: Supernova-dominated Primordial Galaxies, *ApJ*, 2004, vol. 613, p. L97 B.1

- Murray N., Quataert E., Thompson T. A., On the Maximum Luminosity of Galaxies and Their Central Black Holes: Feedback from Momentum-driven Winds, *ApJ*, 2005, vol. 618, p. 569 6.1, 6.1
- Navarro J. F., Eke V. R., Frenk C. S., The cores of dwarf galaxy haloes, *MNRAS*, 1996, vol. 283, p. L72 B.1
- Navarro J. F., Frenk C. S., White S. D. M., A Universal Density Profile from Hierarchical Clustering, *ApJ*, 1997, vol. 490, p. 493 B.1, B.3.2
- Navarro J. F., Hayashi E., Power C., Jenkins A. R., Frenk C. S., White S. D. M., Springel V., Stadel J., Quinn T. R., The inner structure of Λ CDM haloes - III. Universality and asymptotic slopes, *MNRAS*, 2004, vol. 349, p. 1039 B.1
- Neronov A., Vovk I., Evidence for Strong Extragalactic Magnetic Fields from Fermi Observations of TeV Blazars, *Science*, 2010, vol. 328, p. 73 7.1
- Norris J. E., Wyse R. F. G., Gilmore G., Yong D., Frebel A., Wilkinson M. I., Belokurov V., Zucker D. B., Chemical Enrichment in the Faintest Galaxies: The Carbon and Iron Abundance Spreads in the Boötes I Dwarf Spheroidal Galaxy and the Segue 1 System, *ApJ*, 2010, vol. 723, p. 1632 2.1, 2.2
- Okamoto T., Gao L., Theuns T., Mass loss of galaxies due to an ultraviolet background, *MNRAS*, 2008, vol. 390, p. 920 6.2, 6.2
- Ostriker J. P., McKee C. F., Astrophysical blastwaves, *Reviews of Modern Physics*, 1988, vol. 60, p. 1 B.2.1
- Padmanabhan T., *Theoretical Astrophysics - Volume 1, Astrophysical Processes*. Cambridge University Press, 2000 2
- Pahud C., Kamionkowski M., Liddle A. R., Oscillations in the inflaton potential?, *Phys. Rev. D*, 2009, vol. 79, p. 083503 5.1
- Parkinson H., Cole S., Helly J., Generating dark matter halo merger trees, *MNRAS*, 2008, vol. 383, p. 557 2

- Pasetto S., Grebel E. K., Berczik P., Spurzem R., Dehnen W., Isolated dwarf galaxies: from cuspy to flat dark matter density profiles and metallicity gradients, *A&A*, 2010, vol. 514, p. A47 B.1
- Peñarrubia J., Benson A. J., Walker M. G., Gilmore G., McConnachie A. W., Mayer L., The impact of dark matter cusps and cores on the satellite galaxy population around spiral galaxies, *MNRAS*, 2010, vol. 406, p. 1290 B.1
- Peñarrubia J., McConnachie A. W., Navarro J. F., The Cold Dark Matter Halos of Local Group Dwarf Spheroidals, *ApJ*, 2008, vol. 672, p. 904 4
- Pedrosa S., Tissera P. B., Scannapieco C., The impact of baryons on dark matter haloes, *MNRAS*, 2009, vol. 395, p. L57 B.1
- Peebles P. J. E., The Gravitational Instability of the Universe, *ApJ*, 1967, vol. 147, p. 859 7.1
- Power C., Baugh C. M., Lacey C. G., The redshift evolution of the mass function of cold gas in hierarchical galaxy formation models, *MNRAS*, 2010, vol. 406, p. 43 2, 3
- Press W. H., Schechter P., Formation of Galaxies and Clusters of Galaxies by Self-Similar Gravitational Condensation, *ApJ*, 1974, vol. 187, p. 425 3.2.1, 5.1.2
- Ratra B., Cosmological 'seed' magnetic field from inflation, *ApJ*, 1992, vol. 391, p. L1 7.1
- Read J. I., Gilmore G., Mass loss from dwarf spheroidal galaxies: the origins of shallow dark matter cores and exponential surface brightness profiles, *MNRAS*, 2005, vol. 356, p. 107 B.1
- Rees M. J., Reinhardt M., Some Remarks on Intergalactic Magnetic Fields, *A&A*, 1972, vol. 19 7.1
- Rindler-Daller T., Analytical galactic models with mild stellar cusps, *MNRAS*, 2009, vol. 396, p. 997 B.3.2
- Rodrigues L. F. S., Baugh C. M., Opher R., Influence of primordial magnetic fields on the formation of galaxies, in preparation, 2011 7

- Rodrigues L. F. S., de Souza R. S., Opher R., Suppression of small baryonic structures due to a primordial magnetic field, *MNRAS*, 2010, vol. 406, p. 482 7, B.2.2
- Rodrigues L. F. S., Opher R., Large change in the predicted number of small halos due to a small amplitude oscillating inflaton potential, *Phys. Rev. D*, 2010, vol. 82, p. 023501 5
- Rosswog S., Astrophysical smooth particle hydrodynamics, *New A Rev.*, 2009, vol. 53, p. 78 3
- Sakuma M., Susa H., Feedback Effects of First Supernovae on the Neighboring Dark Matter Halos, *ApJ*, 2009, vol. 698, p. 155 B.2.1
- Salucci P., Burkert A., Dark Matter Scaling Relations, *ApJ*, 2000, vol. 537, p. L9 B.1
- Schleicher D. R. G., Banerjee R., Klessen R. S., Reionization: A probe for the stellar population and the physics of the early universe, *Phys. Rev. D*, 2008, vol. 78, p. 083005 7.1
- Schmidt M., The Rate of Star Formation., *ApJ*, 1959, vol. 129, p. 243 3.2.4
- Shapley H., A Stellar System of a New Type, *Harvard College Observatory Bulletin*, 1938a, vol. 908, p. 1 2
- Shapley H., Two Stellar Systems of a New Kind, *Nature*, 1938b, vol. 142, p. 715 2
- Simon J. D., Geha M., The Kinematics of the Ultra-faint Milky Way Satellites: Solving the Missing Satellite Problem, *ApJ*, 2007, vol. 670, p. 313 2.1, 2.2
- Solomon P. M., Vanden Bout P. A., Molecular Gas at High Redshift, *ARA&A*, 2005, vol. 43, p. 677 3.2.4
- Springel V., E pur si muove: Galilean-invariant cosmological hydrodynamical simulations on a moving mesh, *MNRAS*, 2010, vol. 401, p. 791 3
- Springel V., Wang J., Vogelsberger M., Ludlow A., Jenkins A., Helmi A., Navarro J. F., Frenk C. S., White S. D. M., The Aquarius Project: the subhaloes of galactic haloes, *MNRAS*, 2008, vol. 391, p. 1685 3.1.2, 4

- Springel V., White S. D. M., Jenkins A., Frenk C. S., Yoshida N., Gao L., Navarro J., Thacker R., Croton D., Helly J., Peacock J. A., Cole S., Thomas P., Couchman H., Evrard A., Colberg J., Pearce F., Simulations of the formation, evolution and clustering of galaxies and quasars, *Nature*, 2005, vol. 435, p. 629 3.1.1
- Strigari L. E., Bullock J. S., Kaplinghat M., Diemand J., Kuhlen M., Madau P., Redefining the Missing Satellites Problem, *ApJ*, 2007, vol. 669, p. 676 4, 4.2
- Strigari L. E., Bullock J. S., Kaplinghat M., Simon J. D., Geha M., Willman B., Walker M. G., A common mass scale for satellite galaxies of the Milky Way, *Nature*, 2008, vol. 454, p. 1096 2.2, 2.4
- Subramanian K., Magnetizing the universe, *ArXiv e-prints*, 2008 7.1
- Sutter P. M., Yang H.-Y. K., Ricker P. M., Foreman G., Pugmire D., An examination of magnetized outflows from active galactic nuclei in galaxy clusters, *MNRAS*, 2011, p. 1802 8
- The Planck Collaboration The Scientific Programme of Planck, *arXiv:astro-ph/0604069*, 2006 5.1
- Tollerud E. J., Bullock J. S., Strigari L. E., Willman B., Hundreds of Milky Way Satellites? Luminosity Bias in the Satellite Luminosity Function, *ApJ*, 2008, vol. 688, p. 277 2.3, 2.3, 1
- Tonini C., Lapi A., Salucci P., Angular Momentum Transfer in Dark Matter Halos: Erasing the Cusp, *ApJ*, 2006, vol. 649, p. 591 B.1
- Vasiliev E. O., Vorobyov E. I., Shchekinov Y. A., First supernovae in dwarf protogalaxies, *A&A*, 2008, vol. 489, p. 505 B.2.1
- Wasserman I., On the origins of galaxies, galactic angular momenta, and galactic magnetic fields, *ApJ*, 1978, vol. 224, p. 337 7.1
- Whalen D., Abel T., Norman M. L., Radiation Hydrodynamic Evolution of Primordial H II Regions, *ApJ*, 2004, vol. 610, p. 14 B.2

- Whalen D., van Veelen B., O'Shea B. W., Norman M. L., The Destruction of Cosmological Minihalos by Primordial Supernovae, *ApJ*, 2008a, vol. 682, p. 49 B.2
- Whalen D., van Veelen B., O'Shea B. W., Norman M. L., The Destruction of Cosmological Minihalos by Primordial Supernovae, *ApJ*, 2008b, vol. 682, p. 49 B.2.1
- Widrow L. M., Origin of galactic and extragalactic magnetic fields, *Reviews of Modern Physics*, 2002, vol. 74, p. 775 7
- Willman B., In Pursuit of the Least Luminous Galaxies, *Advances in Astronomy*, 2010, vol. 2010 2, 2
- Wise J. H., Abel T., Resolving the Formation of Protogalaxies. III. Feedback from the First Stars, *ApJ*, 2008, vol. 685, p. 40 B.2
- Wolf J., Martinez G. D., Bullock J. S., Kaplinghat M., Geha M., Muñoz R. R., Simon J. D., Avedo F. F., Accurate masses for dispersion-supported galaxies, *MNRAS*, 2010, vol. 406, p. 1220 2.1
- Xu G., A New Parallel N-Body Gravity Solver: TPM, *ApJS*, 1995, vol. 98, p. 355 3.1
- Xu H., Li H., Collins D. C., Li S., Norman M. L., Evolution and Distribution of Magnetic Fields from Active Galactic Nuclei in Galaxy Clusters. I. The Effect of Injection Energy and Redshift, *ApJ*, 2010, vol. 725, p. 2152 7.1, 8
- Yamazaki D. G., Ichiki K., Kajino T., Mathews G. J., New constraints on the primordial magnetic field, *Phys. Rev. D*, 2010, vol. 81, p. 023008 7.1
- York D. G., Adelman J., Anderson Jr. J. E., Anderson S. F., Annis J., Bahcall N. A., Bakken J. A., Barkhouser R., Bastian S., Berman E., Boroski W. N., Bracker S., Briegel C., et al. The Sloan Digital Sky Survey: Technical Summary, *AJ*, 2000, vol. 120, p. 1579 2
- Zentner A. R., Bullock J. S., Halo Substructure and the Power Spectrum, *ApJ*, 2003, vol. 598, p. 49 2, 5.2
- Zhao D. H., Jing Y. P., Mo H. J., Börner G., Accurate Universal Models for the Mass Accretion Histories and Concentrations of Dark Matter Halos, *ApJ*, 2009, vol. 707, p. 354 B.3.2

Appendix

Appendix A

Fiducial model

In several chapters of this work, we illustrated the effect of astrophysical processes on the formation of satellite galaxies using a modified version the semi-analytic model GALACTICUS.

The results presented employed a modified version of this code, based on its version 0.9.0, revision number 429.

A.1 Halo gas accretion module

Originally, GALACTICUS uses what is known as ' $V_{\text{cut}}/z_{\text{cut}}$ implementation' for reionization, where the accretion of gas to haloes is simply switched off if the redshift is smaller than some “reionization redshift” parameter, $z < z_{\text{cut}}$, and the circular velocity is smaller than a “minimum velocity” parameter, $V < V_{\text{cut}}$.

While this simple approach captures the essence of reionization photoheating (i.e. that at sufficiently high redshifts, the gas accretion of sufficiently small haloes is sharply suppressed), the filtering mass approach described in section 6.2 allows a more explicit connection between the Jeans mass and the hot gas accretion.

Therefore, instead of using that default implementation, I wrote an extra module that implements the hot gas accretion to haloes using filtering mass approach. This new module also allows the calculation of the filtering mass taking into account the effect of magnetic fields, following the reasoning described in section 7.2.

A.2 Parameters choice

The set of parameters which was used (listed in the tables A.2—A.4, in the end of this chapter) is a modified version of “model894” set of parameters that was obtained from Benson, A. J. (2011) as an intermediate result of an on-going automated parameter space exploration.

The changes that I made to the parameter set were not obtained through an automated process but instead came from manual adjustments and comparison of the results with observational data (namely, the b_J luminosity function, the stellar mass function and the HI mass function).

One should notice that the choice of the fiducial parameters was made before examining the observables related to the satellite galaxies population. Therefore, there was no attempt to explicitly fit the parameters to the observables associated with satellite galaxies data.

While the choice of those parameters does not represent the best fit, since a complete search on the parameter space is yet to be completed, it presents reasonable agreement with many of observational tests. We show some of those tests in figures A.4-A.3.

A.3 Runs

For each effect studied, two runs of the code were made: one of lower resolution, which was used to compare the consequences of the test with the to study the impact of the effect on the overall galaxy population, and one of higher resolution, used to see the effect on the satellite population. The characteristics of the two runs are summarized in table A.1.

	Low resolution	High resolution
Number of merger trees (n_{trees})	3000	800
Tree resolution	$3 \times 10^9 M_\odot$	$2 \times 10^7 M_\odot$
Minimum final halo mass (M_{max})	$1 \times 10^{10} M_\odot$	$1 \times 10^{15} M_\odot$
Maximum final halo mass (M_{min})	$5 \times 10^{11} M_\odot$	$5 \times 10^{12} M_\odot$

Table A.1 - Properties of the two types of run employed.

The root masses of the merger trees were distributed following

$$M_{\text{halo},i} = M_{\text{min}} \left(\frac{M_{\text{max}}}{M_{\text{min}}} \right)^{x_i} \quad (\text{A.1})$$

with $x_i = i/n_{\text{trees}}$.

Since one wanted to compare the results with the Milky Way satellites data, the output of the high resolution run was filtered. The first requirement for the system to be “Milky-Way-like” was the presence of a bright central galaxy. Thus, only galaxies with luminosities $-18.1 < M_V < -23.1$ (i.e., approximately, $0.1 < L/L_{\text{MW}} < 10$) were selected. From this subgroup, those without any bright satellite (with $M_V < -12$) were further discarded.

A.4 Resources

The source code of the gas accretion module, the parameter set in machine-readable format, as well as other resources, can be accessed from the website:

<http://www.astro.iag.usp.br/~felippe/Tese/LFSRthesis.html>

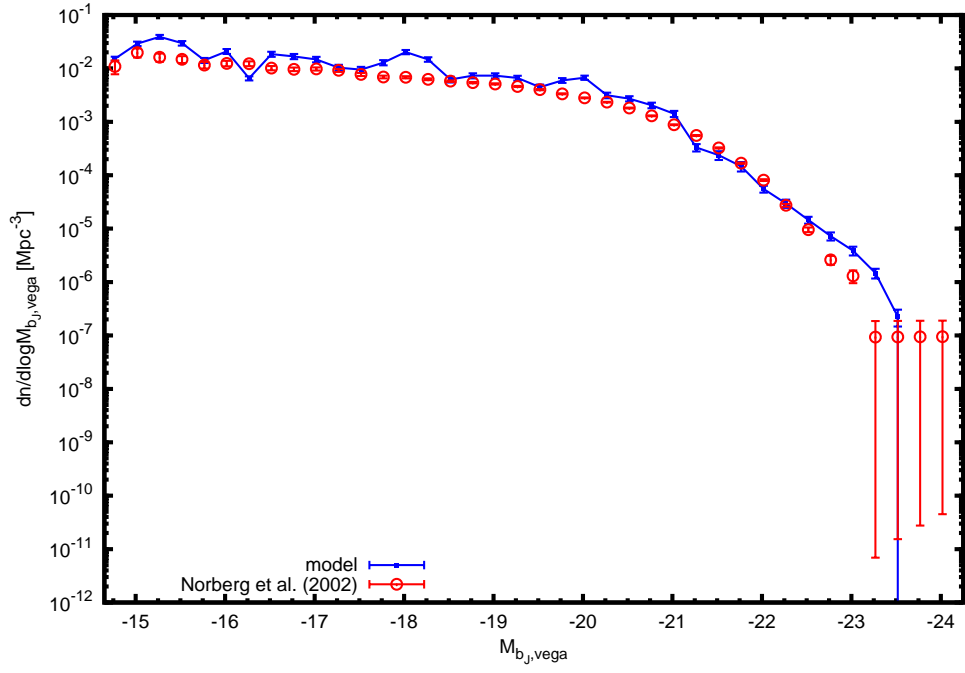


Figure A.1: The b_J luminosity function of the fiducial model.

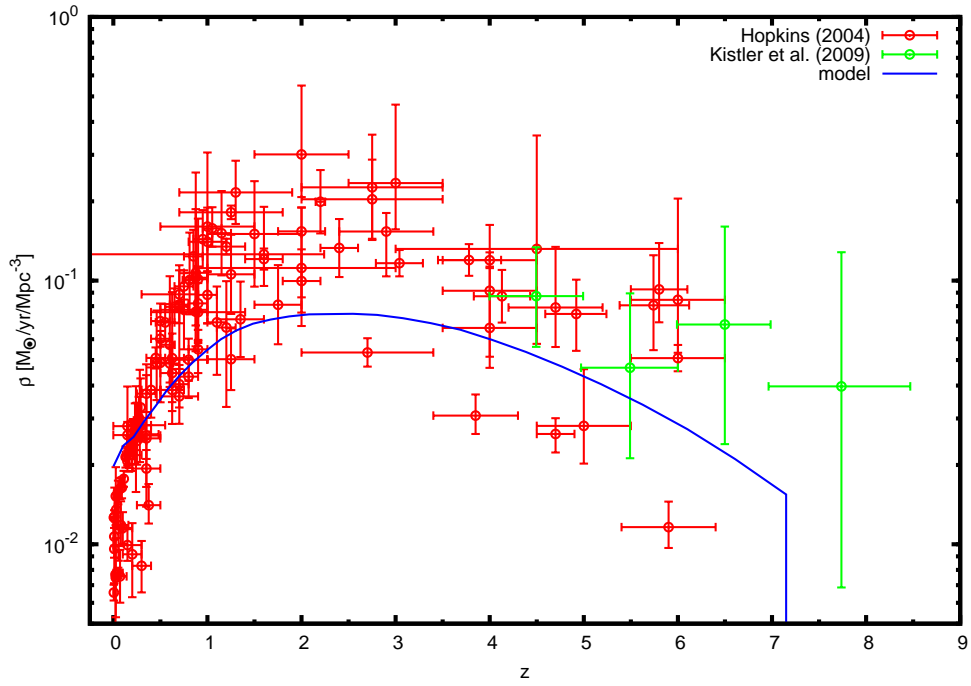


Figure A.2: The star formation history predicted by the fiducial model.

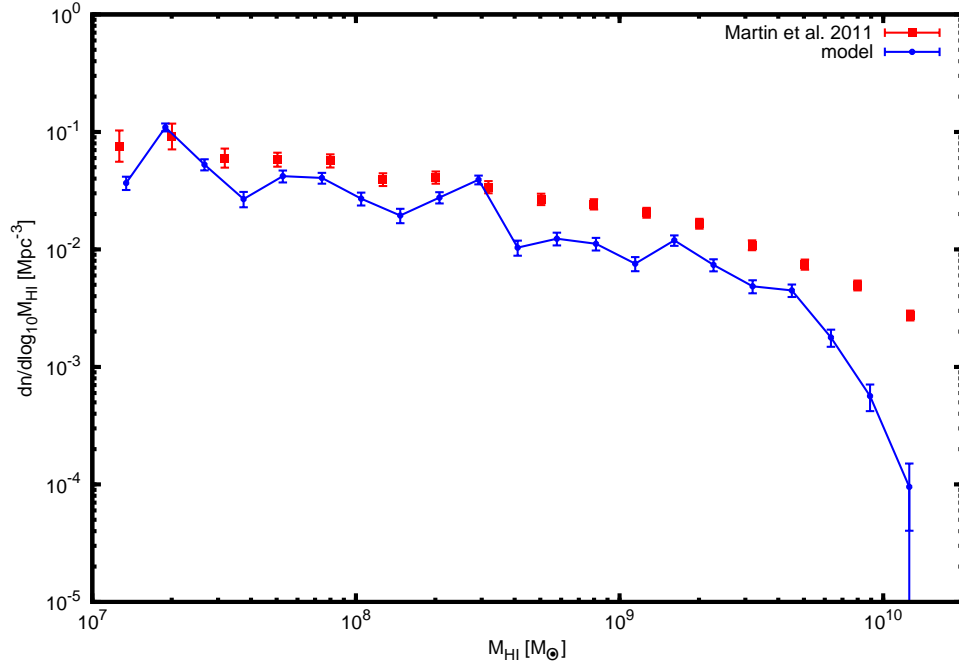


Figure A.3: The HI mass function predicted by the fiducial model.

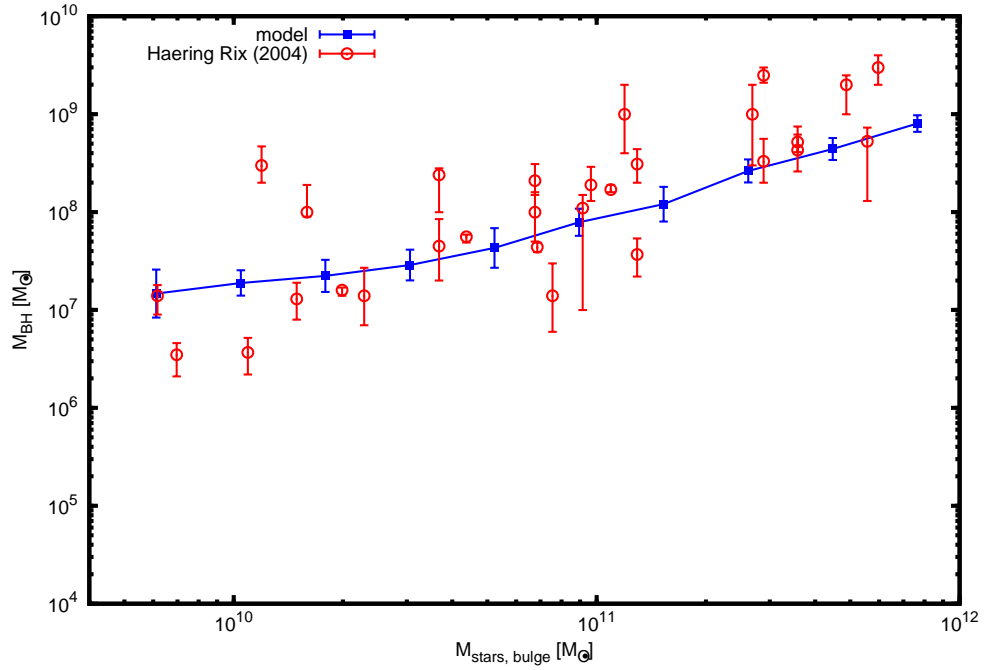


Figure A.4: The relation between the mass of the mass of the bulge and the mass of the central black hole predicted by the fiducial model.

Parameter	Value
H_0	70.2
Ω_M	0.2725
Ω_Λ	0.7275
Ω_b	0.0455
T_{CMB}	2.72548
accretionDisksMethod	switched
accretionHalosMethod	MagneticFiltering
accretionRateThinDiskMaximum	0.65d0
accretionRateThinDiskMinimum	0.01d0
adafAdiabaticIndex	1.444
adafEnergyOption	pure ADAF
adafFieldEnhanceType	exponential
adafRadiativeEfficiency	0.01
adafViscosityOption	fit
adiabaticContractionGnedinA	0.8
adiabaticContractionGnedinOmega	0.77
adiabaticContractionIncludeBaryonGravity	true
allTreesExistAtFinalTime	true
barInstabilityMethod	ELN
blackHoleBinaryMergersMethod	Rezzolla2008
blackHoleHeatsHotHalo	true
blackHoleSeedMass	100
blackHoleWindEfficiency	0.0027
bondiHoyleAccretionEnhancementHotHalo	4.78556137010748
bondiHoyleAccretionEnhancementSpheroid	1
bondiHoyleAccretionTemperatureSpheroid	100
coolingFunctionMethods	atomic_CIE_Cloudy
coolingRadiusMethod	simple
coolingRateMethod	White + Frenk
coolingTimeAvailableAgeFactor	0
coolingTimeAvailableMethod	White-Frenk
coolingTimeMethod	simple
coolingTimeSimpleDegreesOfFreedom	3
cosmologyMethod	matter + lambda
criticalOverdensityMethod	spherical top hat
darkMatterConcentrationMethod	Gao 2008
darkMatterProfileMethod	NFW
darkMatterProfileMinimumConcentration	4
diskMassToleranceAbsolute	1e-06
diskOutflowExponent	2
diskOutflowTimescaleMinimum	0.001
diskOutflowVelocity	155
effectiveNumberNeutrinos	4.34
galacticStructureRadiusSolverMethod	adiabatic
haloMassFunctionMethod	Tinker2008
haloSpinDistributionMethod	Bett2007
heightToRadialScaleDisk	0.137
hotHaloAngularMomentumLossFraction	0
hotHaloCoredIsothermalCoreRadiiMethod	virialRadiusFraction
hotHaloDensityMethod	cored isothermal
hotHaloOutflowReturnOnFormation	false
hotHaloOutflowReturnRate	1
hotHaloTemperatureMethod	virial
imfChabrierRecycledInstantaneous	0.46
imfChabrierYieldInstantaneous	0.02
imfSelectionFixed	Chabrier
imfSelectionMethod	fixed
ionizationStateMethod	atomic_CIE_Cloudy
isothermalCoreRadiusOverVirialRadius	0.34766906
linearGrowthMethod	simple
majorMergerMassRatio	0.25
mergerRemnantRadiativeEfficiency	2.75
mergerRemnantSizeOrbitalEnergy	1

Table A.2 - Fiducial parameters (continues)

Parameter	Value
mergerTreeBuildCole2000AccretionLimit	0.1
mergerTreeBuildCole2000MassResolution	see section A.3
mergerTreeBuildCole2000MergeProbability	0.1
mergerTreeBuildHaloMassMaximum	see section A.3
mergerTreeBuildHaloMassMinimum	see section A.3
mergerTreeBuildMethod	Cole2000
mergerTreeBuildTreesBaseRedshift	0
mergerTreeBuildTreesPerDecade	see section A.3
mergerTreeConstructMethod	build
mergerTreePruneBranches	false
mergerTreePruneHierarchyAtDepth	0
mergerTreePruningMassThreshold	0
mergingTimescaleMultiplier	1
minorMergerGasMovesTo	spheroid
modifiedPressSchechterFirstOrderAccuracy	0.1
modifiedPressSchechterG0	0.57
modifiedPressSchechterGamma1	0.38
modifiedPressSchechterGamma2	-0.01
nodeMergersMethod	single level hierarchy
odeToleranceAbsolute	0.01
odeToleranceRelative	0.01
outputRedshifts	0
powerSpectrumIndex	0.961
powerSpectrumMethod	power law
powerSpectrumReferenceWavenumber	1
powerSpectrumRunning	0
pressureCharacteristicBlitzRosolowsky	4.54
pressureExponentBlitzRosolowsky	0.92
primordialMagneticFieldIntensity	0
randomSeed	1717
randomSpinResetMassFactor	2
reionizationCompletedRedshift	10
reionizationExponentAlpha	6
reionizationStartsRedshift	11
reionizationTemperatureISM	10000
satelliteMergingMassMovementsMethod	simple
satelliteMergingMethod	Jiang2008
satelliteMergingRemnantSizeMethod	Covington2008
sigma_8	0.807
spheroidAngularMomentumAtScaleRadius	0.2546479089
spheroidEnergeticOutflowMassRate	0.45
spheroidMassToleranceAbsolute	1e-06
spheroidOutflowExponent	2
spheroidOutflowSaturation	0
spheroidOutflowTimescaleMinimum	0.001
spheroidOutflowVelocity	100
spinDistributionBett2007Alpha	2.509
spinDistributionBett2007Lambda0	0.04326
stabilityThresholdGaseous	0.9
stabilityThresholdStellar	1.1
starFormationFeedbackDisksMethod	power law
starFormationFeedbackSpheroidsMethod	power law
starFormationFrequencyNormalizationBlitzRosolowsky	5.25e-10
starFormationSpheroidEfficiency	0.008
starFormationSpheroidMinimumTimescale	0.001
starFormationSpheroidVelocityExponent	0
starFormationTimescaleDisksMethod	Blitz-Rosolowsky
starFormationTimescaleSpheroidsMethod	dynamical time
starveSatellites	true

Table A.3 - Fiducial parameters (continues)

Parameter	Value
stellarPopulationLuminosityIntegrationToleranceRelative	0.001
stellarPopulationPropertiesMethod	instantaneous
stellarPopulationSpectraMethod	Conroy, White & Gunn
stellarPopulationSpectraPostprocessMethod	Meiksin2006
summedNeutrinoMasses	0
surfaceDensityCriticalBlitzRosolowsky	200
surfaceDensityExponentBlitzRosolowsky	0.4
timestepHistoryBegin	0.68887459571576
timestepHistoryEnd	13.7774919143152
timestepHistorySteps	30
timestepHostAbsolute	1
timestepHostRelative	0.1
timestepSimpleAbsolute	1
timestepSimpleRelative	0.1
transferFunctionMethod	Eisenstein + Hu
treeBranchingMethod	modified Press-Schechter
treeNodeMethodBasic	standard
treeNodeMethodBlackHole	standard
treeNodeMethodDarkMatterProfile	scale
treeNodeMethodDisk	exponential
treeNodeMethodHotHalo	standard
treeNodeMethodMergingStatistics	standard
treeNodeMethodSatelliteOrbit	simple
treeNodeMethodSpheroid	Hernquist
treeNodeMethodSpin	random
velocityDispersionDiskGas	10
virialDensityContrastMethod	spherical top hat
virialOrbitsMethod	Benson2005
zeroCoolingRateAboveVelocity	10000

Table A.4 - Fiducial parameters

Appendix B

Cusps and cores

In this chapter I present an original contribution on a related topic that was studied during this doctorate: the discrepancy between the predicted and observed density profiles of dark matter dominated galaxies. The results reproduced here were originally published in de Souza, Rodrigues, Ishida & Opher (2011).

B.1 Introduction

The presence of a cusp in the centre of cold dark matter (CDM) haloes is one of the strongest results of N-body simulations (Moore et al., 1999; Navarro et al., 1997, 2004). However, the slope of this density profile is in apparent discrepancy with some observations of disk galaxies and galaxy clusters, which exhibit rather flat density cores (Burkert, 1995; Kuzio de Naray et al., 2008; de Blok, 2005; de Blok et al., 2003; Salucci & Burkert, 2000). On the other hand, e.g., Coccato et al. (2008) studied the bulge and the disk kinematics of the giant low surface brightness galaxy ESO 323-G064 and showed that observations are not able to disentangle different density profiles, in that context. Parallel to the alternative models for dark matter already proposed, there are also attempts to solve this discrepancy within the CDM cosmology using baryonic physics (e.g., Mashchenko et al. (2006, 2008); Governato et al. (2010)).

The so-called core/cusp problem has been in the spotlight of astrophysical research for quite a while (for a recent review, see de Blok (2010)). One natural attempt to solve the apparent contradiction, is to study the gravitational effect of baryons in the dark matter density profile. This approach was first suggested by Navarro et al. (1996). The study of external impulsive mass loss events (Read & Gilmore, 2005) and steady

winds (Gnedin & Zhao, 2002) corroborated with the idea that baryons have a crucial role in the determination of the density profile (Pedrosa et al., 2009). Mashchenko et al. (2006) and Pasetto et al. (2010) discuss how star formation processes can interfere in the central profile shape. Peñarrubia et al. (2010) argue that the existence of the central cusp is necessary in order to maintain the baryons trapped in the halo's gravitational potential. According to their results, the sum of SN explosions, tidal effects and star formation processes can completely destroy dwarf spheroidal haloes which initially present a core like central density. Several authors suggested that the interstellar medium (ISM) of dwarf galaxy systems could be entirely removed by supernovae (SNe) explosions (Dekel & Silk, 1986; Hensler et al., 2004; Mori et al., 2002, 2004; Mac Low & Ferrara, 1999). In this work, we study the effect of a single SN explosion on the removal of baryon gas from the first haloes and the effects of this removal on the shape of the density profile.

As stated in Mashchenko et al. (2006, 2008) once removed, the cusp cannot be reintroduced during subsequent mergers involved in hierarchical evolution of galaxies. This statement is supported by numerical and analytical results. Outcomes from simulations made by Kazantzidis et al. (2006) imply that the universal characteristic shape of dark matter density profiles may be set early in the evolution of haloes and Dehnen (2005) shows theoretically that the remnant cusp cannot be steeper than any of the progenitor cusps.

In this work, we consider the possibility to solve the apparent core-cusp problem via baryonic physics (Mashchenko et al., 2006, 2008). The sudden gas removal makes the dark matter distribution to expand. Such mechanism can operate efficiently in small high redshift haloes, creating dark matter cores (Governato et al., 2010). Using arguments similar to those presented by Tonini et al. (2006); de Souza & Opher (2010), we analyse this process in the context of distribution functions.

It is initially assumed that baryons and dark matter are in an equilibrium configuration. Considering that energy perturbations track the initial energy distribution (dominated mainly by dark matter), after being perturbed, the halo will redistribute dark matter particles in a new equilibrium configuration. As a consequence, variations in the initial halo distribution function, caused by energy or angular momentum

perturbations, are followed by macroscopic quantities, such as the energy density profile.

In this paper, we considered the Λ CDM model with best fit parameters from Jarosik et al. (2011) (WMAP-Yr7¹), $\Omega_m = 0.267$, $\Omega_\Lambda = 0.734$, $\Omega_b = 0.0449$, and $H_0 = 0.71$. The paper is organized as follows. In section B.2, we briefly review our knowledge about the propagation of blastwaves in the interstellar medium (ISM) and show the fraction of gas that can be removed from the haloes; in section B.3, discuss the changes in density profile due to gas removal; and in section B.4, present and discuss our results. Finally, in section B.5, we discuss our conclusions.

B.2 Expulsion of baryonic gas by a supernova explosion

Since the gravitational potential of the first collapsed haloes is shallow, the ionizing radiation from the first stars can expel the gas out of them (Abel et al., 2007; Alvarez et al., 2006; Kitayama et al., 2004; Whalen et al., 2004; Wise & Abel, 2008). As a result, a subsequent SN can break away from the halo due to the decreased gas density by photoionization prior to the explosion (Kitayama & Yoshida, 2005; Whalen et al., 2008a). In order to understand the nature of the SN shock expanding into an essentially uniform and ionized intergalactic space, we assume spherical symmetry.

B.2.1 Evolution of a supernova blastwave

As described in the review on astrophysical blastwaves by Ostriker & McKee (1988), and in the recent paper of Sakuma & Susa (2009), the evolution of a supernova remnant (SNR) in the intergalactic medium (IGM) can be described as follows. Initially, the energy is largely thermal, but as the supernova expands, the adiabatic expansion converts thermal into kinetic energy.

During the first stage, the SN ejecta sweeps out roughly the same amount of mass as its own in the surrounding medium. In the second stage, the expansion of the shock front is well approximated by the Sedov-Taylor solution. Eventually, radiative losses from the SNR become significant, and the remnant enters in the third, radiative, stage

¹ <http://lambda.gsfc.nasa.gov/product/map/current/>

of its evolution. A thin shell is formed just behind the shock front. Finally the SNR expands conserving momentum.

Vasiliev et al. (2008) found that supernova explosions with an energy 10^{53} ergs expel a significant portion of the initial baryonic mass from protogalaxies with total mass $\sim 10^7 M_\odot$. Whalen et al. (2008b) performed numerical simulations of primordial supernovae in cosmological haloes from $6.9 \times 10^5 - 1.2 \times 10^7 M_\odot$ and showed that even less energetic explosions are capable of ejection of more than 90% of the baryons from haloes containing $\lesssim 10^7 M_\odot$. Based on such studies, we assume that feedback from SN explosions are able to expel up to all the baryonic gas in primordial haloes. Our next step then, is to evaluate what fraction of the total halo mass is in form of gas.

B.2.2 Gas mass fraction

In order to evaluate the ratio of ejected gas mass to total (virial) halo mass, we used the expression obtained by Gnedin (2000)

$$f_{gas}(M, z) = \frac{\Omega_b/\Omega_m}{\left(1 + 0.26 \frac{M_F(z)}{M}\right)}, \quad (\text{B.1})$$

where f_{gas} is the mass fraction of the halo, M_F is the filter mass (e.g., Gnedin (2000); Rodrigues et al. (2010); de Souza et al. (2011)), Ω_b and Ω_m are the baryonic and dark matter energy density parameter, respectively and M corresponds to the total (virial) mass of the halo. According to Kravtsov et al. (2004), $M_F \approx 5 \times 10^6 M_\odot$ at redshift $z = 10$, and the reionization epoch is assumed to occur between $z \sim 8 - 11$ (e.g., the gas fraction of haloes with $M \sim 10^7 M_\odot$ was $f_{gas} = 0.148$ at $z \sim 10$).

Since it is unlikely that the ejection of baryons was completely efficient, we consider cases where 5%, 10% and 15% of the total mass was expelled, which correspond to 31%, 61% and 92% of expulsion of the halo's baryonic mass, respectively.

B.3 Evolution of the density profile of dark haloes

In order to understand the effect on the density profile, caused by the removal of baryonic matter from the halo, we study the evolution of its distribution function

(hereafter DF).

B.3.1 Distribution functions and density profiles

The DF fully describes the state of any collisionless system at any time, specifying the number of particles $f(x, v, t) d^3x d^3v$ having positions in the small volume d^3x centered on x and velocities in the small range d^3v centered on v . The evolution of a collisionless system is governed by the Boltzmann equation, $\frac{df}{dt} = 0$.

The DF of a mass distribution in a steady state is related to its density profile through

$$\rho(r) = \int f(r, v) d^3v. \quad (\text{B.2})$$

For an isotropic galaxy, the density can be written in the simple form

$$\rho(r) = 4\sqrt{2}\pi \int_0^{\Psi(r)} [\Psi(r) - \mathcal{E}]^{1/2} f(\mathcal{E}) d\mathcal{E}, \quad (\text{B.3})$$

where Ψ is the relative potential and

$$\mathcal{E} \equiv \Psi(r) - v^2/2$$

is the relative energy (Cuddeford, 1991; Binney & Tremaine, 2008).

Equation (B.3) is an Abel integral whose solution is

$$f(\mathcal{E}) = \frac{\sqrt{2}}{4\pi^2} \frac{d}{d\mathcal{E}} \int_0^{\mathcal{E}} \frac{d\rho}{d\Psi} \frac{d\Psi}{\sqrt{\mathcal{E} - \Psi}}. \quad (\text{B.4})$$

B.3.2 Parametrizing the density profile

The usual parametrizations of cuspy density profiles (eg. NFW) lead to potentials without a simple analytical solution for the inverse function, $r(\Psi)$. As a consequence, it is generally not possible to obtain an analytical form for the DF from equation (B.4).

In order to avoid these complications, we adopt the following family of spherical potentials (Rindler-Daller, 2009),

$$\Psi = \frac{b^{\alpha\gamma}}{(b^\alpha + r^\alpha)^\gamma}, \quad (\text{B.5})$$

which leads to density profiles of the form

$$\rho(r) = \rho_g \alpha \gamma b^{\alpha \gamma} \frac{(1 + \alpha)b^\alpha + (1 - \alpha \gamma)r^\alpha}{r^{2-\alpha}(b^\alpha + r^\alpha)^{\gamma+2}}, \quad (\text{B.6})$$

where ρ_g is a characteristic density to be adjusted for each profile, or, in terms of the relative potential

$$\begin{aligned} \rho(\Psi) = & \frac{\rho_g}{1 + \alpha} \Psi^{1+\frac{1}{\gamma}} \left(\Psi^{-\frac{1}{\gamma}} - 1 \right)^{1-\frac{2}{\alpha}} \\ & \times \left[1 - \alpha \gamma + \alpha(1 + \gamma) \Psi^{\frac{1}{\gamma}} \right]. \end{aligned} \quad (\text{B.7})$$

This form of the density profile can conveniently capture the behavior of cusp and cored density profiles, for specific choices of the parameters (α, γ, b) .

NFW profile

The most common choice for the form of the density profile of haloes, which is also in best agreement with DM N-body simulations, is the NFW density profile (Navarro et al., 1997),

$$\rho(r) = \frac{\rho_s}{\frac{r}{r_s} \left(1 + \frac{r}{r_s} \right)^2}. \quad (\text{B.8})$$

Where r_s and ρ_s are determined by the concentration parameter c through

$$r_s = \frac{r_{\text{vir}}}{c} \text{ and } \rho_s = \frac{\rho_{\text{vir}}}{3} \frac{c^3}{\log(1+c) - \frac{c}{1+c}}, \quad (\text{B.9})$$

where $\rho_{\text{vir}} = 178 \bar{\rho}$, is the average density of a virialized halo, and r_{vir} corresponds to its radius.

Since we are treating very high redshift ($z > 10$) haloes (i.e. in the beginning of their mass accretion histories), we use $c = 4$, following the prescription of Zhao et al. (2009).

A different choice of c should not, however, affect significantly the forthcoming results, since all of them can be expressed in function of the parameters ρ_s and r_s and will, thus, scale with a change in the concentration.

In figure B.1 we show that the density profile of equation (B.6) provides a very good

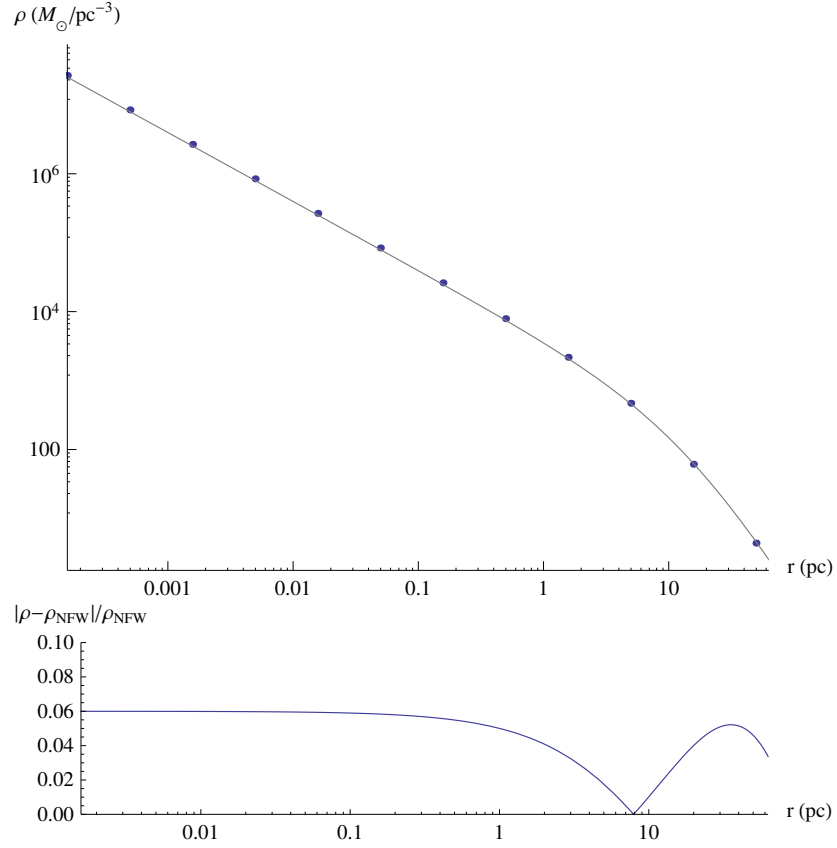


Figure B.1: In the upper panel, the continuous (gray) curve shows the NFW density profile of a halo of mass $10^7 M_\odot$ at $z = 10$, and the (blue) points correspond to the general profile with $\alpha = 1$, $\gamma = 1/2$ and $b = 1.085 r_s = 36.8$ pc. In the lower panel the fractional difference between the two profiles is shown.

approximation to the NFW profile for the choice $\alpha = 1$, $\gamma = \frac{1}{2}$, $b = 1.085 r_s$ and $\rho_g = \rho_s$, with the difference between the two profiles never exceeding 10%.

Cored profiles

Many recent observations (Burkert, 1995; Donato et al., 2009) favor the Burkert density profile, which has the form

$$\rho_{\text{bur}}(r) = \frac{\rho_0}{\left(1 + \frac{r}{r_0}\right) \left(1 + \frac{r^2}{r_0^2}\right)}. \quad (\text{B.10})$$

The Burkert profile can be well approximated by equation (B.6) choosing $\alpha = 2$, $\gamma = \frac{1}{16}$, $b = 0.76 r_0$ and $\rho_g = \rho_0$, as shown in figure B.2.

Another common choice for a cored density profile, is the pseudo-isothermal (PI)

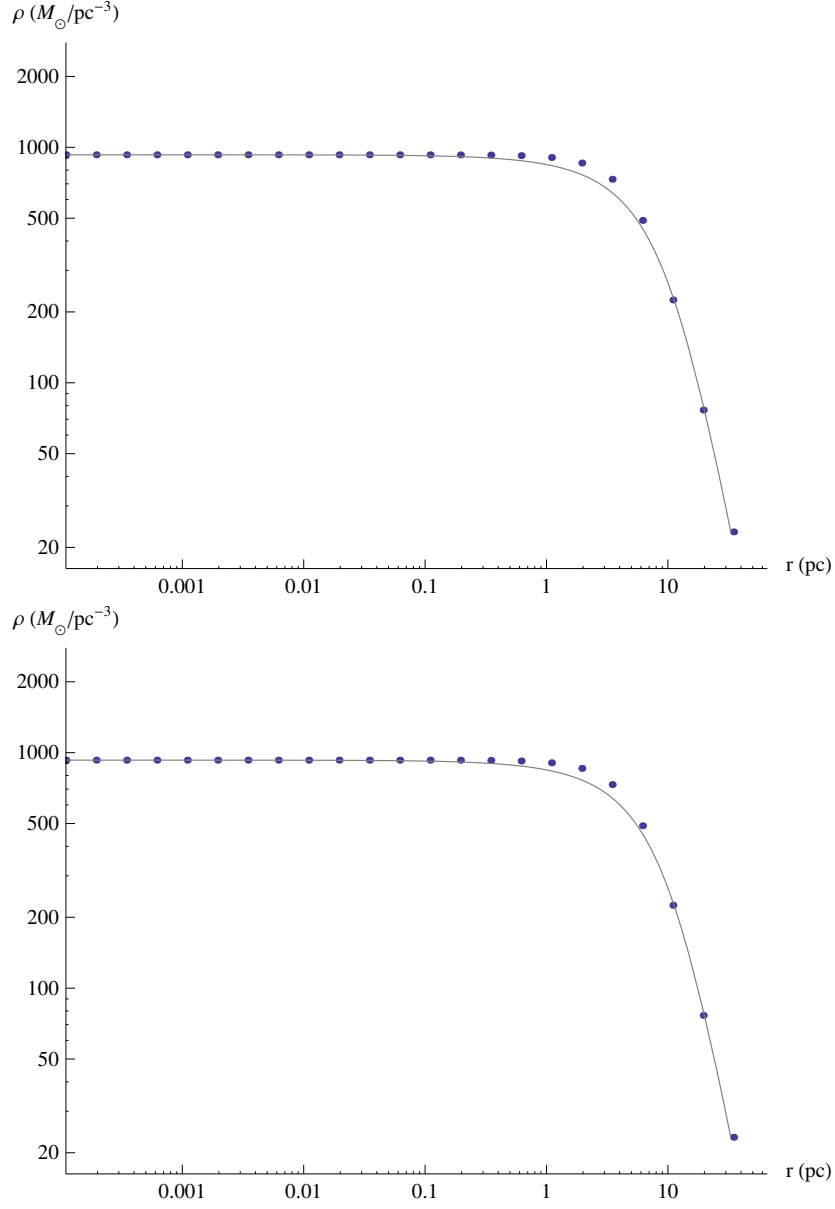


Figure B.2: In the upper panel, the continuous (gray) curve shows the Burkert density profile of a halo of mass $10^7 M_{\odot}$ at $z = 10$, and the (blue) points correspond to the general profile with $\alpha = 3/5$, $\gamma = 6/5$ and $b = 1.58 r_s = 53.7$ pc. In the lower panel the fractional difference between the two profiles is shown.

profile

$$\rho_{\text{iso}}(r) = \frac{\rho_0}{1 + \left(\frac{r}{r_0}\right)^2}. \quad (\text{B.11})$$

B.3.3 Perturbing the distribution function

The Boltzmann equation of a collisionless isotropic system is

$$\frac{df}{dt} = 0 \quad \Rightarrow \quad \frac{\partial f}{\partial t} + \frac{\partial \mathcal{E}}{\partial t} \frac{\partial f}{\partial \mathcal{E}} = 0. \quad (\text{B.12})$$

The removal of the baryons from the halo will lead to a small change in its energy, $\delta\mathcal{E}$. This change will take a small amount of time, δt , and will cause a change in the DF. We will assume that the distribution function, after the perturbation, $f(t + \delta t, \mathcal{E})$, will have the form

$$f(t + \delta t, \mathcal{E}) \equiv f(t, \mathcal{E} + \delta\mathcal{E}). \quad (\text{B.13})$$

To demonstrate the validity of the above assumption, we first expand the last equation keeping only first order terms in $\delta\mathcal{E}$,

$$f(t + \delta t, \mathcal{E}) \equiv f(t, \mathcal{E} + \delta\mathcal{E}) \approx f(t, \mathcal{E}) + \delta\mathcal{E} \left. \frac{\partial f}{\partial \mathcal{E}} \right|_{t, \mathcal{E}}. \quad (\text{B.14})$$

If the ejection took place on a small time interval, δt , the transformation in the distribution function can be written as

$$\frac{\delta f}{\delta t} = \frac{f(t + \delta t, \mathcal{E}) - f(t, \mathcal{E})}{\delta t} = - \left. \frac{\delta\mathcal{E}}{\delta t} \frac{\partial f}{\partial \mathcal{E}} \right|_{\mathcal{E}}, \quad (\text{B.15})$$

which, in the limit of small time intervals, is precisely the Boltzmann equation.

B.3.4 Relation between relative energy and perturbed halo mass

The formalism discussed in section B.3.3 allows us to understand how the removal from the halo, of a certain amount of relative energy, $\delta\mathcal{E}$, change the density profile. It is, however, necessary to relate this change of energy with the actual expulsion of baryons by SNe.

From a fundamental point of view, this correspondence is far from trivial since the

same amount of energy could be removed by either lower mass, faster particles or higher mass, slower particles. There is, also, a cosmological context, where taking into account the mass outside the virial radius is not a sensible choice.

We avoid those complexities taking the final density profile calculated for a given $\delta\mathcal{E}$ and, then, calculating the virial mass by a simple – and fast convergent – iterative procedure.

We initialize the virial radius variable, $r_{vir}^{(0)}$, with the virial radius of the unperturbed halo. We then calculate the virial mass using

$$M_{vir}^{(i)} = \int_0^{r_{vir}^{(i-1)}} 4\pi r^2 \rho(r) dr \quad (\text{B.16})$$

where $\rho(r)$ is the perturbed density profile. We reevaluate the virial radius

$$r_{vir}^{(i)} = \left(\frac{M_{vir}^{(i)}}{\frac{4}{3}\pi \rho_{vir}} \right)^{1/3} \quad (\text{B.17})$$

and proceed to the next iteration.

This procedure converges rapidly to a consistent value for the virial mass of a perturbed halo, which can be compared with the known virial mass of the unperturbed halo (set to $10^7 M_\odot$ in our calculations), therefore allowing us to relate variations in energy with variations in mass.

B.4 Results

Using the formalism developed in the end of section B.3, we calculated the DF associated with NFW density profile:

$$\begin{aligned} f(\mathcal{E}) = & - \frac{1}{56\sqrt{2}(-1+\mathcal{E}^2)^3\pi^2} \left[4(-1+\mathcal{E})\mathcal{E}^{3/2} \right. \\ & \times (1+\mathcal{E})(28-9\mathcal{E}^2-136\mathcal{E}^4+96\mathcal{E}^6) \\ & + 21\sqrt{1-\mathcal{E}}(1+\mathcal{E})^3 \arcsin(\sqrt{\mathcal{E}}) \\ & \left. + 21(-1+\mathcal{E})^3\sqrt{1+\mathcal{E}} \operatorname{arctanh}\left(\sqrt{\frac{\mathcal{E}}{1+\mathcal{E}}}\right) \right] \end{aligned} \quad (\text{B.18})$$

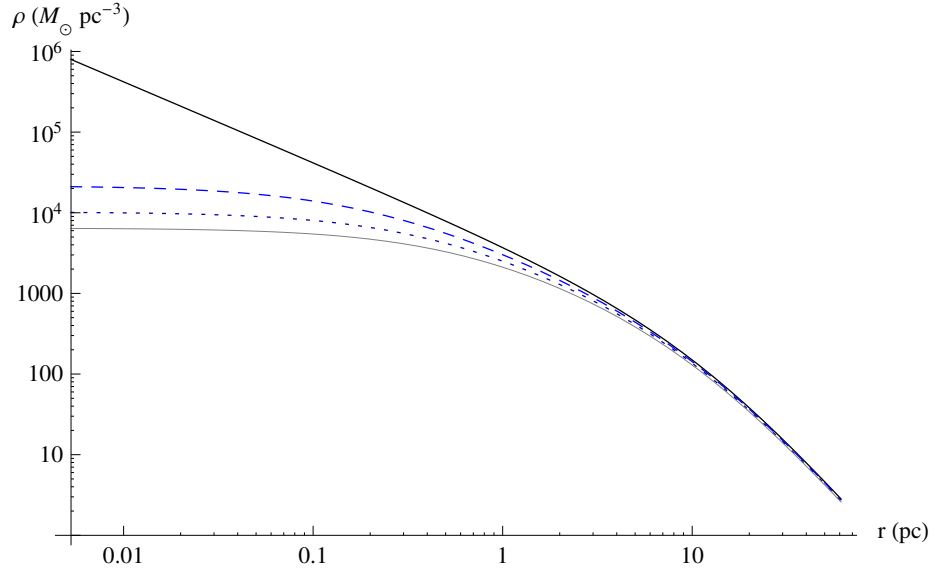


Figure B.3: New equilibrium configuration of the perturbed halo removing 5% (dashed curve), 10% (dotted curve) or 15% (thin curve) of the total mass of the halo, compared to the NFW profile (top solid line).

The DF found were then perturbed through equation (B.13) and a transformed density profile was generated from it using equation (B.3).

In figure B.3 we see how a NFW density profile varies due to the expulsion of 5%, 10% and 15% of mass of the halo (namely, removal of 0.57%, 1.17% and 1.81% of the relative energy, respectively). The appearance of a core in the transformed density profile is noticeable.

In order to get better quantitative insight, we fit a pseudo-isothermal density profile to the resultant transformed profile. We found a core radii of $r_0 = 0.054 r_s$, $r_0 = 0.075 r_s$ and $r_0 = 0.092 r_s$ for the removal of 5%, 10% and 15% of the the halo's mass, respectively.

We also fit a Burkert-like profile finding $r_0 = 0.20 r_s$, $r_0 = 0.24 r_s$ and $r_0 = 0.28 r_s$ for 5%, 10% and 15% of removal of the halo's mass.

As in the NFW case, we fit a pseudo-isothermal density profile to the resultant transformed profile. We found core radii of $r_0 = 0.011 r_s$, $r_0 = 0.012 r_s$ and $r_0 = 0.013 r_s$ for the removal of 5%, 10% and 15% of mass of the halo (namely, removal of 0.70%, 1.44% and 2.22% of the relative energy, respectively). The fit of a Burkert-like profiles leads to $r_0 = 0.074 r_s$, $r_0 = 0.069 r_s$ and $r_0 = 0.064 r_s$ for 5%, 10% and 15% of removal of the the halo's mass. Our core radius are approximately similar to the one found

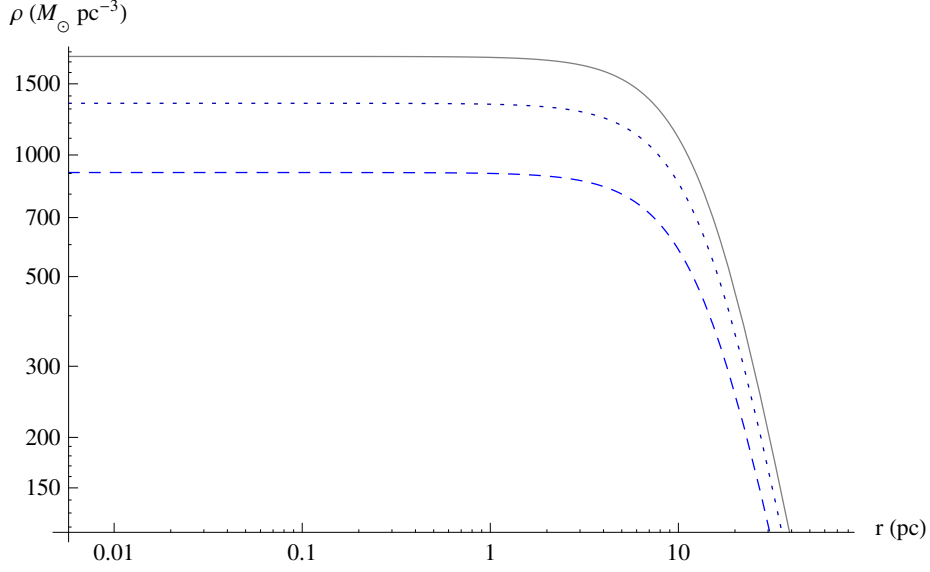


Figure B.4: New equilibrium configuration of the perturbed halo removing 1% (dotted line) and 2.5% (dashed line) of total energy E , compared to the original Burkert profile (solid line).

by Gnedin & Zhao (2002). In their analysis, they r_0 lies in the range $0 \lesssim r_0 \lesssim 0.2r_s$, depending of the model for outflow.

As the SN could also occur in a halo which was originally cored (e.g. haloes where the core was previously erased by the process exposed), we performed the same analysis for a halo with an initial core profile. In figure B.4 we show the evolution of a Burkert density profile after energy removal. As we can see, the core structure is maintained after gas removal and its radius remains approximately unchanged.

B.5 Conclusions and discussion

We explored the effect of a supernova explosion on the central density of a small mass ($\sim 10^7 M_\odot$) dark matter halo at high redshifts.

We first reviewed (section B.2) the evidence that supernovae can efficiently expel a large part of the baryonic mass from small haloes.

We then built a simple analytical model where we assume that

1. the halo is approximately isotropic,
2. the mass expelled by the SN leads to a small loss of energy of the halo.

Since typical parametrizations of the density profile do not lead to invertible ex-

pressions for the potentials, we used the profile of equation (B.6), which is shown to be consistent with both cusp and cored density distributions.

From the density profile we calculated the distribution function associated with NFW profile. We, then, evolved this distribution function, removing a small amount of energy from it.

The final density profile found does not present a cusp, but, instead, a core. We found that the transformation from a cusp into a cored profile is present even for changes as small as 0.5% of the total energy of the halo, that can be produced by the expulsion of matter caused by a single SN explosion.